UNIVERSIDADE FEDERAL DE SANTA CATARINA
PROGRAMA DE PÓS-GRADUAÇÃO EM CIÊNCIA E
ENGENHARIA DE MATERIAIS

Cyro Rovath de Faria

PROCESSING OF SHORT FIBER REINFORCED POROUS
CMC AND MMC TUBES BY POWDER THERMOPLASTIC
EXTRUSION

Florianópolis

2011

Catalogação na fonte elaborada pela biblioteca da
Universidade Federal de Santa Catarina

A ficha catalográfica é confeccionada pela Biblioteca
Central.

Tamanho: 7cm x 12 cm

Fonte: Times New Roman 9,5

Maiores informações em:

http://www.bu.ufsc.br/design/Catalogacao.html

Cyro Rovath de Faria

PROCESSING OF SHORT FIBER REINFORCED POROUS CMC AND MMC TUBES BY POWDER THERMOPLASTIC EXTRUSION

Esta Dissertação foi julgada adequada para obtenção do Título de Mestre em Ciência e Engenharia de Materiais, e aprovada em sua forma final pelo Programa de Pós-Graduação em Ciência e Engenharia de Materiais.

Florianópolis, 25 de Fevereiro de 2011

_____
Prof. Carlos Augusto Silva de Oliveira, Dr. Ing.
Coordenador do Programa

Banca Examinadora:

_____
Prof. Antônio Pedro Novaes de Oliveira, Dr. Ing.
Universidade Federal de Santa Catarina

_____
Prof. Antonio Eduardo Martinelli, PhD
Universidade Federal do Rio Grande do Norte

_____
Prof. José Roberto Martinelli, PhD
Universidade de São Paulo

Aos meus pais e à minha esposa

AGRADECIMENTOS

À Universidade Federal de Santa Catarina.

Ao Prof. Dr. Aloisio Nelmo Klein pela orientação e pela confiança em mim depositada.

Ao EMPA (Swiss Federal Laboratories for Materials Science and Technology), em especial ao Dr. Thomas Graule, chefe do Laboratório de Cerâmicas de Alta Performance, pela oportunidade de realizar meu trabalho experimental em seu laboratório.

Ao Dr. Frank Jörg Clemens, pela co-orientação e pelo convite a fazer parte de seu grupo no EMPA.

Aos colegas dos cursos de graduação e pós-graduação pela forte amizade.

Aos colegas de trabalho no EMPA, em especial aos que já lá estavam quando cheguei, por terem sido muito receptivos.

Aos meus pais, Sebastião Sérgio de Faria e Clélia Rovath de Faria, por tudo o que fizeram e me proporcionaram até hoje e por todo o amor dado.

Ao meu irmão e amigo, Rafael Rovath de Faria, pelo exemplo e principalmente pelo incentivo que me fez seguir adiante na vida acadêmica.

À Natalie Rovath de Faria pelo carinho e amor dados durante a segunda metade do meu período de estadia na Suíça, e por se deixar levar pelo meu também dado amor, tornando-se enfim, e antes da defesa deste trabalho, minha eterna companheira e esposa.

Ao destino que fez meu caminho cruzar o de Natalie, então Natalie Gigaud.

"Any sufficiently advanced technology is indistinguishable from magic."

Arthur C. Clarke

RESUMO

Materiais com poros interconectados são comumente usados em diversas aplicações de filtragem, como, por exemplo, purificação de água, filtração de metais fundidos e filtração de gases quentes. Se por um lado, os filtros devem conter uma estrutura de elevada porosidade aberta; em contrapartida, esses materiais devem apresentar resistência mecânica suficiente para suportar a queda de pressão durante o processo de filtração. O objetivo deste trabalho foi estudar a viabilidade de produção de tubos porosos, em compósitos de matriz cerâmica e metálica reforçados por fibras, via extrusão termoplástica de pós, para aplicação em processos de filtração. A extrusão termoplástica é um processo contínuo, capaz de promover um alto nível de alinhamento de fibras na direção de extrusão, sem que haja excessiva fratura de fibras durante o processamento. Pós de alumina e superliga de níquel foram selecionados para formar a matriz dos compósitos de matriz cerâmica e metálica, respectivamente. Fibras curtas de alumina foram utilizadas como reforço. Como componentes do sistema ligante foram utilizados polietileno de baixa densidade (LDPE), parafina (PW) e ácido esteárico (SA). Diferentes proporções entre LDPE-PW-SA foram estudadas a fim de desenvolver um sistema ligante apropriado ao processo. A evolução da viscosidade da mistura em função do teor de sólidos foi estudada e comparada a diversos modelos de viscosidade. Após o desenvolvimento do feedstock de extrusão, 30 % em volume de fibras foram adicionadas a mistura. Tubos com 4,5 a 10,0 mm de diâmetro, com 0,6 e 1,0 mm de espessura foram então extrudados com sucesso, após sucessivas etapas de ajuste dos parâmetros de extrusão. Análises microscópicas confirmaram o alinhamento satisfatório das fibras. Finalmente, após a sinterização dos tubos a 1300 °C durante 60 minutos, meso e macroporosidades foram identificadas através de análises porosimétricas por intrusão de mercúrio, totalizando um volume de poros de, aproximadamente, 41 e 36 % nos tubos de matriz cerâmica e metálica, respectivamente. O nível de porosidade, bem como o tamanho médio de poros, foi considerado adequado à aplicação em certos processos de filtração, em especial a filtração de gases quentes.

Palavras-chave: Extrusão. Materiais porosos. Compósitos reforçados por fibras. Compósitos de matriz metálica. Compósitos de matriz cerâmica. Sistemas ligantes.

ABSTRACT

Materials with interconnected pore network are commonly used in several filtering applications, *e.g.* water purification, molten metal filtration, and hot-gas filtration. On one hand filters must contain a highly open porous structure; on the other hand these materials must have sufficient mechanical strength to withstand the pressure drop during the filtration process. The objective of this work was to study the feasibility to produce short fiber reinforced porous ceramic and metal matrix composites tubes, processed by powder thermoplastic extrusion, for application in filtering processes. The powder thermoplastic extrusion is a continuous process, able to promote high alignment of fibers in the extrusion direction, without excessive fiber breakage. Alumina and nickel superalloy powders have been selected to form the matrix of the ceramic and metallic matrix composites, respectively. Short alumina fibers have been used as reinforcement. Low density polyethylene (LDPE), paraffin wax (PW) and stearic acid (SA) formed the binder system. Different proportions of LDPE-PW-SA have been studied in order to develop a binder system suitable for the extrusion process. The evolution of the feedstock viscosity as a function of the solids content was studied and compared to various viscosity models. After the development of the extrusion feedstock, 30 vol.% of fibers were incorporated to the mixture. Tubes with 4.5 and 10.0 mm of diameter, with 0.6 and 1.0 mm of thickness, were then successfully extruded, after the complete extrusion parameters adjustment. Microscopy analysis confirmed the satisfactory fiber alignment. Finally, after sintering the tubes at 1300 °C for 60 minutes, meso and macroporosity were identified by mercury intrusion porosimetry analysis, with a total pore volume of, approximately, 41 and 36 % in the ceramic and metal matrix composites, respectively. The porosity level, as well as the average pore size, have been considered adequate for the application in certain filtration processes, particularly in hot-gas filtration.

Keywords: Extrusion. Porous materials. Fiber reinforced composites. Metal matrix composites. Ceramic matrix composites. Binder systems.

LIST OF FIGURES

LIST OF TABLES

LIST OF ABBREVIATIONS

CIP – Cold isostatic pressing
CMC – Ceramic matrix composite
HDPE – High density polyethylene
HIP – Hot isostatic pressing
IGCC – Integrated gasification combined cycle
LDPE – Low density polyethylene
MFI – Melt flow index
MMC – Metal matrix composite
PE – Polyethylene
PFBC – Pressurized fluidized-bed combustion
PIM – Powder injection molding
PIP – Polymer infiltration and pyrolysis
PMC – Polymer matrix composite
PMP – Particulate materials processing
PP – Polypropylene
PS – Polystyrene
PSD – Particle size distribution
PW – Paraffin wax
SA – Stearic acid
SEC – Size exclusion chromatography
SEM – Scanning electron microscopy
SHS – Self-propagation high temperature synthesis
TGA – Thermogravimetric analysis
WHIPOX – Wound highly porous oxide CMC
XRD – X-ray diffraction

LIST OF SYMBOLS

l_c – Fiber critical length
d_f – Fiber diameter
σ_f* – Fiber strength
τ_i* – interface shear strength
T_c – Critical temperature
t_c – Time of exposure in the critical temperature
M – Metal
γ_{SL} – Solid-liquid surface tension
ΔG – Gibbs free energy
T_g – Glass transition temperature
T_m – Melting temperature
A – Area
x – Distance
v – Velocity
f – Force
$\dot{\gamma}$ – Velocity gradient or shear rate
τ – Shear stress
η – Viscosity
T – Temperature
η_0 – Viscosity at a reference temperature
T_0 – Reference temperature
k – Boltzmann's constant
E – Activation energy
E_a – Apparent activation energy
η_r – Relative viscosity
ϕ – Volume fraction
ϕ_r – Relative solids volume fraction
ϕ_m – Maximum solids volume fraction
η_b – Binder viscosity
∞ – Infinite
A, B, k and n – Unknown constants
λ – Crowding factor
r – Particle radius
$[\eta]$ – Intrinsic viscosity
D – Diffusion coefficient
L – Particle length
D – Particle diameter

ΔG_T – Total Gibbs free energy

ΔG_V – Gibbs free energy associated with volume

ΔG_B – Gibbs free energy associated with boundaries

ΔG_S – Gibbs free energy associated with surface area

A_S – Surface area

V_P – Volume of feedstock displaced by the piston

v_P – Piston speed

A_P – Piston section area

t – time

V_E – Extruded volume

v_E – Extrusion speed

A_D – Die section area

CONTENT

1.   INTRODUCTION

Porous materials, more specifically interconnected porous materials, are used in several applications, in particular filtering. Examples of filtering process are the water purification, oil filtration, aerosols filtration, hot-gas filtration and molten metal filtration (FERNANDO, et al., 2002; FERNANDO, et al., 2005; STUDART, et al., 2006). Filtration is a very important process for several fields, in particular for the petrochemical, mining and chemical industries (FERNANDO, et al., 2005).

For its application to be successfully attended, a porous material used for filtering must fulfill the following requirements (DUO, et al., 1999):

    i.   Presence of an interconnected porous network;
    ii.   Pore size distribution according to the size of the filtered particulate;
    iii.   Permeability to the filtered fluid;
    iv.   Sufficient mechanical strength to withstand the fluid pressure drop;
    v.   Thermal resistance to withstand high temperatures, up to 1000 °C, in the case of hot-gas filtration;
    vi.   Corrosion and oxidation resistance.

On one hand these materials must contain high open porosity, according to the application, on the other hand, high mechanical strength is also required for the component to withstand the pressure drop imposed by the filtering process.

The introduction of short fibers is an intelligent solution to improve the mechanical strength, without jeopardizing the permeability of the component. In the search of appropriate materials for the production of porous components, short fibers were found to be good precursors for membranes used in hot-gas and aerosols filtration (FERNANDO, et al., 2005).

One way to optimize the utilization of fibers is to align them in the direction of the highest tensile strain imposed to the component. It is well known that powder injection molding (PIM) and powder extrusion have the ability to align short fibers in the direction of the viscous flux of the material (CHAWLA, et al., 2006; YE, et al., 2008). The

alignment is parallel in contracting flow and perpendicular in expanding flow (YE, et al., 2008). The same benefit can be obtained by the powder thermoplastic extrusion.

The fiber alignment achieved by extrusion processes is one of the reasons why this route was chosen to produce short fibers reinforced porous tubes. Furthermore this process shows other important advantages such as:

i.   Fiber length maintenance (fiber breaking occurs only during the mixing step);

ii.   Possibility to produce thin wall tubes without shape collapse;

iii.   It is a continuous process, which is a very important issue for industry in terms of time and process variability;

iv.   Possibility to produce components with a high length/thickness ratio.

In the present work alumina short fibers were added to alumina powder and a nickel based alloy powder, to produce ceramic matrix composite (CMC) and metal matrix composite (MMC) porous tubes, respectively. The idea was to validate a process that could suit several different applications in which ceramic or metallic filters are required.

Nextel™ 610 alumina fibers were chosen due to purity and availability at the EMPA laboratory where this project was carried out. Alumina powder was chosen for its well known thermal and chemical stability, adequate for filtering applications (FERNANDO, et al., 2002). The IN718 nickel superalloy was chosen for its high thermal and corrosion resistance.

1.1.   OBJECTIVES

1.1.1.   General objectives

The aim of this work is to study the feasibility to produce short fiber reinforced porous CMCs and MMCs tubes, processed via powder thermoplastic extrusion.

1.1.2.   Specific objectives

  i.   Development of a feedstock with tailored solids content and binder system, which is adequate for subsequent extrusion and debinding steps. The feedstock should be common for alumina and IN718 powders, not to double the amount of work necessary to achieve the further objectives;
 ii.   Investigation of the influence of the fibers on feedstock mixing and debinding;
iii.   Investigation of the influence of cylinder temperature, die temperature and piston speed on the extrusion pressure and extrudate visual aspect;
 iv.   Control of extrusion parameters in order to obtain defect-free extruded tubes;
  v.   Comparison of debinding behavior between disk shaped and tubular shaped samples;
 vi.   Definition of a debinding route that is able to maintain tube geometry until sintering step;
vii.   Characterization of sintered MMC and CMC tubes regarding microstructure, porosity and crystalline phases.

2. LITERATURE REVIEW

2.1. COMPOSITES

Composite materials comprise any material that has at least two chemically or physically distinct phases. The combination of the two different phases usually provides a combination of properties that cannot be obtained by the components individually (CHAWLA, et al., 2006). The continuous phase is the matrix, while the distributed phase is the reinforcement, which can be in the form of particles, whiskers, fibers or laminate (CHAWLA, 2003) as shown in Figure 1.
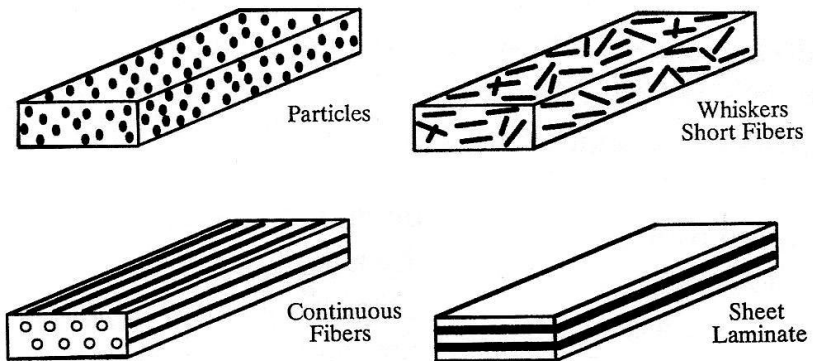
Figure 1 – Classification of composites according to the reinforcement form. Source: Chawla (2003).

Both matrix and reinforcement can be polymeric, ceramic or metallic. According to the matrix material is convenient to separate the composites into three groups: polymer matrix composites (PMC's), ceramic matrix composites (CMCs) and metal matrix composites (MMCs) (CHAWLA, 2003).

Normally a composite performs its function as far as the fiber is loaded via fiber/matrix interface. Therefore the interface in composites has so much importance (MILEIKO, 1997).

In a composite, there are two types of bonding at the interface of matrix and reinforcement, mechanical and chemical bonding. In PMC's and MMCs it is important that both types of bonding are present, in a

way that the load can be transmitted from the weaker matrix to the typically stiffer reinforcement. Whereas for CMCs mechanical bonding is more desirable than chemical bonding so that a series of fracture mechanisms such as crack-bridgind, crack deflection, fiber fracture and fiber pull-out can take place. The energy consumed in these fracture mechanisms leads to an enhanced fracture toughness and a non-catastrophic failure mode (CHAWLA, 2003; CHAWLA, et al., 2006).

The main advantage of CMCs and MMCs have in common, in comparison with PMC's, are the higher temperature ranges that these materials can be submitted (CHAWLA, et al., 2006).

A metal matrix composite has usually a ductile matrix. The most efficient fibers are graphite, boron, carbides, and oxides, which are brittle. In the case of ceramic matrix composites, usually both matrix and fibers are brittle (MILEIKO, 1997).

This work relates with short alumina fibers reinforced CMCs and MMCs. The characteristic of such materials will be described in the following sections.

A big variety of processing routes are available to produce CMCs and MMCs such as (CHAWLA, 2003; CHAWLA, et al., 2006; GERMAN, 1990; SURESH, et al., 1993; CHOU, et al., 1985):

    i.   Cold pressing and sintering;
    ii.   Hot pressing;
    iii.   Injection molding;
    iv.   Conventional extrusion;
    v.   Forging;
    vi.   Rolling;
    vii. Reaction and diffusion bonding;
    viii. Casting or liquid infiltration;
    ix.   Squeeze casting or pressure infiltration;
    x.   Spray co-deposition
    xi.   Direct oxidation – Lanxide™ process;
    xii. In-situ chemical reaction techniques;
    xiii. Sol-gel;
    xiv. Polymer infiltration and pyrolysis – PIP;
    xv. Self-propagation high temperature synthesis – SHS;
    xvi. Electrophoretic deposition;
    xvii. Explosive shock consolidation;

Compared with these processes, thermoplastic powder extrusion features two main advantages regarding the processing of fibrous composites. First it is a process, like others related feedstock processing routes, which induces fiber alignment (GERMAN, 1990; SHENOY, 1999; CALOW, et al., 1972). The fiber alignment can be good to tailor properties such as strength and creep resistance in a preferential direction (CALOW, et al., 1971). Figure 2 shows schematically the concept of fiber alignment obtained with PIM processing.
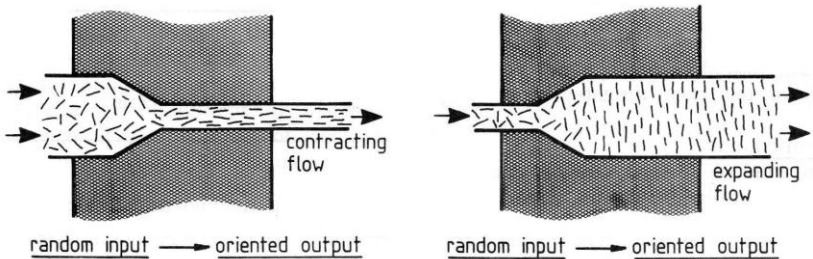
Figure 2 – Schematic diagram showing fiber alignment due to contracting and expanding flow during injection or feedstock extrusion process.
Source: German (1990).

Fiber alignment is not an exclusivity of feedstock processing, other routes including conventional extrusion, rolling, forging and squeeze casting may also grant an oriented microstructure (CHAWLA, et al., 2006; SURESH, et al., 1993). Figure 3 shows a quantitative analysis of the degree of orientation of SiC particles in a conventionally extruded MMC.
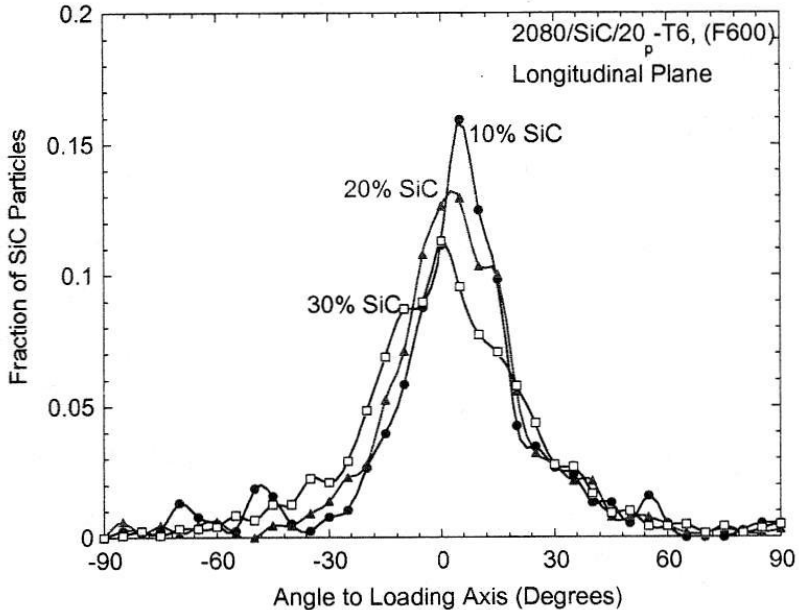
Figure 3 – Quantitative analysis of the degree of orientation of SiC particles in an extruded 2080 aluminum alloy matrix composite with 20 vol.% of reinforcement fraction. The degree of orientation is defined by the angle of a given article to loading axis.
Source: Chawla, et al (2006).

However, because of the high strains associated with process such as rolling, forging and conventional extrusion, fracture of short fibers and even particles take place, which can be detrimental to the properties of the composite (CHAWLA, et al., 2006). The fracture of fibers leads to the second advantage of feedstock processing, *e.g.* thermoplastic powder extrusion, because due to the low viscosity of the feedstock at molding temperatures, both fibers and particles are subjected to lower strains, as compared with conventional extrusion, which avoids fiber breaking (GERMAN, 1990).

The breaking of fiber is acceptable until the fibers reaches a minimum length at which it is still effective, *i.e.* contributes to increase the strength and stiffness of the composite. This length is called critical length l_c, and depends on the fiber diameter d_f, the fiber strength σ_f^* and on the interface shear strength τ_i^*, according to Equation 1 (MILEIKO, 1997; CALLISTER, 2006; CALOW, et al., 1972).

Equation 1 $$l_c = \frac{\sigma_f^* d_f}{2\tau_i^*}$$

2.1.1. Alumina based fibers as reinforcement

Ceramic fibers are very attractive for reinforcement of both CMCs and MMCs. They combine high strength, high modulus, chemical resistance, high temperature capabilities, being ideal candidates for high temperature applications (CHAWLA, 2003).

Due to the small cross section and large aspect ratio, ceramic fibers have two very important features: their high degree of flexibility and higher strength than the bulk material of the same composition (CHAWLA, 2003; CHAWLA, et al., 2006).

A big problem of high temperature applications is the oxidation when the material is exposed to oxidizing atmosphere (LEV, et al., 1995). Carbon fibers oxidizes easily at temperatures above 400 °C. Silicon carbide (SiC) fibers are also prone to oxidation at temperatures higher than 1200 °C (CHAWLA, 2003). A solution to the oxidation problem demands the use of oxide fibers (LEV, et al., 1995). Oxide fibers are available since 1970s and have been thoroughly investigated (CHAWLA, 2003).

Among the oxides, alumina is one of the most stable in a variety of environments, although its melting point, 2050 °C, is not one of the highest. Its thermodynamically stable phase is the hexagonal α-Al_2O_3 (CHAWLA, 2003; CHAWLA, et al., 2006), which the structure is shown on Figure 4.
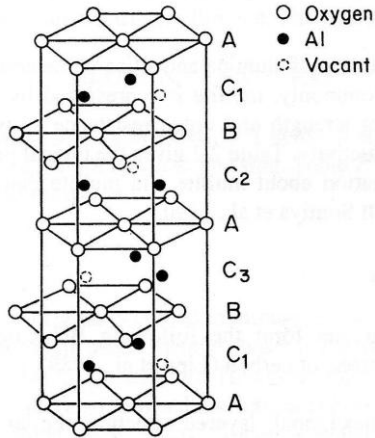
Figure 4 – Hexagonal close-packed structure of α-alumina.
Source: Chawla (2003).

Since decades many companies produce in high scale polycrystalline alumina fibers, being the fibers produced by Du Pont, Sumitomo Chemical Co., and 3M Co. (formerly known as Minnesota Mining and Manufacturing Co.) among the most commercialized (CHAWLA, 2003).

The highest performance fibers that are now available in adequate quantities and at reasonable cost are fine-grained high-purity alumina (Nextel™ 610) and alumina/mullite (Nextel™ 720) fibers produced by the 3M Co. The Nextel™ 610 has the highest strength (~3.3 GPa) and higher corrosion resistance, while the Nextel™ 720 shows better creep resistance, being stable at higher temperatures, 1200 °C for Nextel™ 720 against 1100 °C for The Nextel™ 610 (MARSHALL, et al., 2001).

Table 1 shows the data of some of the commercially available alumina fibers.

Table 1 – Data of some commercial alumina fibers. Some may be no longer available.

Comercial Name	Composition (wt.%)	Diameter (μm)	Density (g/cm^3)	Tensile Strength (GPa)	Young's Modulus (GPa)
FP	>99 Al_2O_3	20	3.9	1.4	380
PRD-166	80 Al_2O_3 20 ZrO_2	18	4.2	1.9	344
Nextel 312	62.5 Al_2O_3 24.5 SiO_2 13 B_2O_3	10 – 12	2.7	1.7	150
Nextel 440	70 Al_2O_3 28 SiO_2 2 B_2O_3	10 – 12	3.05	2.0	190
Nextel 480*	70 Al_2O_3 28 SiO_2 2 B_2O_3	10 – 12	3.05	2.3	224
Nextel 550	73 Al_2O_3 27 SiO_2	10 – 12	3.03	2.0	193
Nextel 610	>99 Al_2O_3	10 – 12	3.9	3.1	370
Nextel 650*	89 Al_2O_3 10 ZrO_2 1 Y_2O_3	10 – 12	4.10	2.55	358
Nextel 720	85 Al_2O_3 15 SiO_2	10 - 12	3.40	2.1	260
Saffil	96 Al_2O_3 4 SiO_2	3	2.3	1.0	100
Saphikon	Single Crystal 100 Al_2O_3	70 – 250	3.8	3.1	380
Sumitomo	85 Al_2O_3 15 SiO_2	9	3.2	2.6	250
Almax	>99.5 Al_2O_3	10	3.6	1.8	320

* No longer available
Source: Chawla (2003); Mileiko (1997); Bansal (2005); Dhingra (1980).

Nextel fibers are polycrystalline which gives them isotropic properties, *e.g.* isotropic thermal expansion, what can make easier to

avoid thermal expansion mismatch between matrix and fibers (CHAWLA, 2003).

Sintering of alumina fibers should not exceed 1300 °C. Above this temperature the properties of the fibers reduces due to degradation (LEE, et al., 2003).

2.1.2. Metal matrix composites

Metal matrix composites development has been impelled by some advantages with respect to unreinforced metals. Comparing with the analog unreinforced metal, MMCs may enhance the following properties (CHAWLA, et al., 2006; SURESH, et al., 1993):

i.	Specific strength;
ii.	Specific modulus;
iii.	Dimensional stability;
iv.	Reduced coefficient of thermal expansion;
v.	Creep resistance;
vi.	Fatigue resistance;
vii.	Wear resistance;
viii.	Isotropy.

When compared with CMCs, metal matrix composites have as advantage higher thermal, electrical conductivity and fracture toughness (SURESH, et al., 1993; CHAWLA, 2003).

Examples of metals commonly used as the matrix on composites are: aluminum and aluminum alloys, titanium alloys, magnesium and magnesium alloys, cobalt, iron and iron alloys, copper, silver, nickel and nickel alloys, including nickel superalloys, niobium, and intermetallics[1] (CHAWLA, et al., 2006; SURESH, et al., 1993).

For high temperature applications the matrix systems are mainly nickel-, niobium-, and cobalt-based alloys, as well as intermetallics. The MMCs with these matrix systems are developed for applications at temperatures over 800 °C (SURESH, et al., 1993).

---

[1] The chemical bond in intermetallics is actually not metallic, but ionic or covalent in nature. Intermetallics are formed when two dissimilar metals are combined following chemical valence rules, *i.e.* ionic or covalent rules (CHAWLA, et al., 2006).

The two main routes to produce MMCs are via liquid state processing and solid state processing. The advantages of the solid state processing, which is mostly based on powder metallurgy techniques, is the control of reinforcement distribution, uniformity of matrix microstructure, and lower degree of interfacial reaction between matrix and reinforcement which can be detrimental to the reinforcement (CHAWLA, et al., 2006).

Increasingly MMCs are used in several areas including aerospace, automotive and railway industries; electronics; thermal management; filamentary superconducting magnets; power transmission; sporting goods; and wear-resistant materials (CHAWLA, et al., 2006; SURESH, et al., 1993).

2.1.2.1.   Alumina fibers reinforced nickel based composites

The study and development of alumina reinforced nickel based composites was driven the high temperature and oxidation resistance of nickel alloys and the availability of alumina whiskers. A promising application for such composites was high temperature turbine blades. However problems with thermal expansion compatibility (see Table 2), whiskers degradation and weak interface bond made retarded the development of these composites (CALOW, et al., 1972; CALOW, et al., 1971; MILEIKO, 1997; MILEIKO, et al., 2004).

Table 2 – Coefficients of thermal expansion of nickel and alumina.

Material	Coefficient of thermal expansion ($°C^{-1}$)	
	at 373 K	at 1273 K
Ni	13.25×10^{-6}	16.50×10^{-6}
Al_2O_3	6.00×10^{-6}	8.20×10^{-6}

Source: Calow, et al (1972).

Chemical interaction between fiber and matrix is inevitable if there is no thermodynamic equilibrium between them. The consequence will be an interface region containing substances with properties different from the matrix and fiber (MILEIKO, 1997).

Nevertheless difficulties on predicting and avoiding those interactions arise for many reasons. First because phase diagrams of

complex systems elements used in MMCs are unknown. Secondly the kinetics cannot be described without experiments. Thirdly the influence of the interface on the properties of the composite can be varied and depends on the type of load (MILEIKO, 1997).

For systems forming interfaces, such as Ni and Al_2O_3, it is important to predict those product phases formed by diffusion bonding during sintering. However, even if all the thermodynamic data are known, it is still hard to determine which phases will be present in the interface. In the case of the system Ni-Al-O, two different situations can exists, as shown in Figure 5. In high vacuum conditions, with activity of oxygen under 10^{-12}, the diffusion path (path I) follows the side of an aluminum rich phase, poor in oxygen, and no product phase is formed. On the other hand, if the activity of oxygen is higher, the diffusion path follows the tie line that connects the nickel and the spinel (path II), and spinel is formed (SURESH, et al., 1993). For pure nickel matrix, substantial amount of spinel nickel aluminate, $NiAl_2O_4$, can form above 1100 °C (CALOW, et al., 1971).
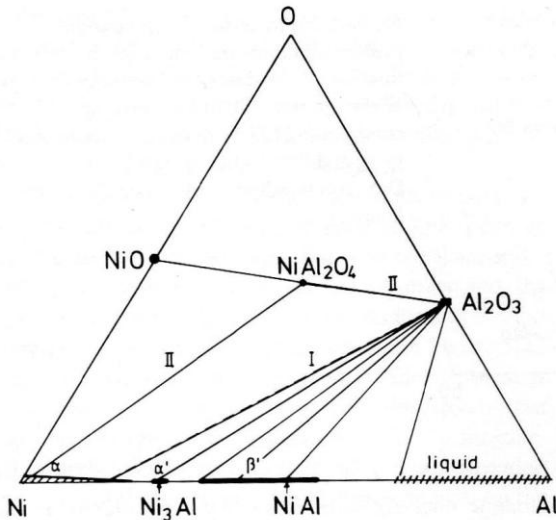
Figure 5 – Ni-Al-O isothermal phase diagram at 1600 K. Two reaction paths are possible when nickel is bonded to Al2O3. (I) low oxygen activity, no reaction product form. (II) high oxygen activity, spinel forms.
Source: Suresh, et al (1993).

One of the consequences of the interaction between the ceramic fiber and the metal matrix is the degradation of the fiber, leading to reduction of fiber strength. Degradation of alumina reinforcement in a nickel-based matrix has been reported (MILEIKO, 1997; MILEIKO, et al., 2002a; CALOW, et al., 1971; CALOW, et al., 1972). Table 3 shows the critical temperature T_c and time of exposure in the critical temperature t_c in which sapphire whiskers, *i.e.* monocrystalline alumina, starts to degrade in the presence of different nickel-based matrix.

Table 3 – Stability of alumina whiskers in nickel-based matrices.

Matrix	t_c (h)	T_c (°C)
Ni	<1	1000
80Ni – 20Cr	<1	1000
Ni-Cr-Fe	<16	1000

Source: Mileiko (1997)

There are three possibilities to avoid such interactions and degradation of the alumina fibers. The first obvious possibility is not to submit the MMC to a long-term exposure at high temperatures during fabrication, what would lead to low densification. The second possibility is matrix alloying; introducing alloying elements on the nickel matrix reduces its interaction with fibers, what has been already experimentally demonstrated with elements such as chromium, aluminum, molybdenum, tungsten, and cobalt (MILEIKO, 1997; MILEIKO, et al., 2002a; CALOW, et al., 1971). Another advantage of alloying the nickel matrix is the reduction of sintering temperature. Pure nickel sintering temperatures are between 1300 and 1350 °C (CALOW, et al., 1972; JOHNSON, et al., 2004). Nevertheless is worthy to mention that sintering of highly porous nickel components, with porosity up to 80 %, can be obtained by sintering loose carbonyl nickel powder at temperatures between 850 and 1050 °C (ASM International, 2000).

The third option to minimize degradation lies on the use of diffusion barriers, avoiding the direct contact between fiber and matrix. Examples of diffusion barriers for nickel matrix composites are HfO_2, Y_2O_3, TiC, ZiN, and HfC. Alumina coated with Y_2O_3-W-Ni has been also reported (MILEIKO, 1997).

If on one hand reaction between the metal matrix and alumina fiber can be detrimental to the final properties of the composite, on the other hand, as mentioned in the previous section, a minimum of

chemical interaction is required for MMCs to guarantee a proper load transfer from matrix to the fibers. Following this approach the formation of a complex oxide $Al_xM_yO_z$ at the interface, where M is an alloying element of the nickel matrix, might be also desirable (MILEIKO, et al., 2002a). Some alloying elements, *e.g.* chromium, improve the bond strength without though causing chemical reaction (CALOW, et al., 1971).

Tests has shown that nickel alloys reinforced with different alumina based fibers have higher creep resistance than any available non-reinforced nickel superalloys (MILEIKO, et al., 2002b; MILEIKO, et al., 2004). The potential for such composites is the use at temperatures up to 1200 °C (MILEIKO, 2002).

2.1.2.2.   Nickel superalloys

As mentioned in the previous section, alloying the nickel matrix is one of the possible approaches to minimize fiber-matrix detrimental interactions (MILEIKO, 1997). Nickel based superalloys are well known for its high temperature strength and resistance. However, nickel based superalloys limiting temperature is below 1100 °C. The only way to enhance the use temperature of such alloys is reinforcing them with creep-resistant ceramic fibers (MILEIKO, et al., 2002a; MILEIKO, et al., 2002b).

Superalloys are the class of heat-resisting alloys based on nickel, nickel-iron, or cobalt. These alloys exhibit a combination of strength and corrosion resistance at elevated and cryogenic temperatures, what make them useful for many applications in the aerospace, automotive, medical, chemical and petrochemical industries (JOHNSON, et al., 2004).

Their high strength and toughness make them difficult to shape via machining and forging. For this reason powder metallurgy techniques, including powder injection molding, are alternative routes that have been used to process these materials (JOHNSON, et al., 2004).

Among the superalloys that have been processed via powder injection molding, IN718 nickel superalloy has been the most extensively studied. This alloy is usually sintered at temperatures between 1250 and 1275 °C to densities close to 100% (ASM International, 2000; JOHNSON, et al., 2004; VALENCIA, et al., 1997;

BOSE, et al., 1997; VALENCIA, et al., 1994; HAJMRLE, et al., 1980). The alloy IN625 is another alloy that can be processed by powder injection molding; however this alloy requires higher sintering temperatures, above 1290 °C to achieve full density (JOHNSON, et al., 2004).

The alloy IN718 is a precipitation-hardenable nickel-chromium alloy that combines corrosion resistance and high strength. It has excellent creep-rupture strength at temperatures up to 700 °C. Used in gas turbines, rocket motors, spacecraft, nuclear reactors, pumps, and tooling. It can form liquid phase during sintering as its melt temperature range is between 1260 and 1336 °C (Special Metals Corporation, 2008). The temperature in which sintering starts is reported to be in the range of ~1160 °C. At this temperature liquid phase sintering is also likely to take place (HAJMRLE, et al., 1980).

Table 4 – Chemical composition of IN718 and IN625 nickel superalloys.

Element	Limiting chemical composition (wt.%)	
	IN718	IN625
Ni	50.00 – 55.00	> 58.00
Cr	17.00 – 21.00	20.00 – 23.00
Fe	Balance	< 5.00
Nb	4.75 – 5.50	3.15 – 4.15
Mo	2.80 – 3.30	8.00 – 10.00
Ti	0.65 – 1.15	< 0.40
Al	0.20 – 0.80	< 0.40
Co	< 1.00	< 1.00
C	< 0.08	< 0.10
Mn	< 0.35	< 0.50
Si	< 0.35	< 0.50
P	< 0.015	< 0.015
S	< 0.015	< 0.015
B	< 0.006	-
Cu	< 0.30	-

Source: Special Metals Corporation, 2008.

IN625 is nickel-chromium-molybdenum alloy with an addition of niobium that acts with the molybdenum to stiffen the alloy's matrix and thereby provide high strength without a strengthening heat treatment. The alloy resists a wide range of severely corrosive environments. Used in chemical processing, aerospace and marine engineering, pollution-

control equipment, and nuclear reactors. Its melting point range is 1290 to 1350 °C (Special Metals Corporation, 2008).

The composition of IN718 and IN625 superalloys are given on Table 4.

2.1.3. Ceramic matrix composites

Although high performance ceramics have high strength, high hardness, excellent high temperature capabilities, chemical inertness, high wear resistance and all allied to low density; these materials have an inherent brittleness, *i.e.* low fracture toughness, being prone to catastrophic failure under mechanical or thermal stresses in the presence of crack-like defects (CHAWLA, 2003). Increase thermal shock resistance and toughness of these materials, making them damage tolerant by introducing reinforcement fibers is the main purpose of the productions of CMCs (CHAWLA, 2003; CINIBULK, et al., 2004; HACKEMANN, et al., 2010). The fiber reinforced CMCs may also show higher tensile strength, stiffness and creep than the monolithic ceramics (CINIBULK, et al., 2004; HACKEMANN, et al., 2010).

For the selection of the matrix and fibers for a specific application, the following properties should be considered (CHAWLA, 2003):

    i.   Melting temperature;
    ii.   Volatility;
    iii.   Density;
    iv.   Elastic modulus;
    v.   Thermal expansion coefficient;
    vi.   Creep characteristics;
    vii.   Strength
    viii.   Fracture toughness;
    ix.   Chemical and thermal compatibility between fiber and matrix.

Some of the items above are discussed in the following section, justifying the selection of the alumina-alumina CMCs used in the present work.

The production of CMCs is driven by cost reduction in terms of fabrication and maintenance, weight reduction (mainly for aerospace and automotive industry), higher operation temperatures (CHAWLA, 2003). Examples of applications for fiber reinforced CMCs are shown in Table 5.

Table 5 – Potential industrial applications for fibers reinforced ceramic composites.

Product area	Component examples
Advanced heat engines	Combustors, liners, wear parts, etc.
Heat recovery equipment	Air preheaters, recuperators.
Burners and combustors	Radiant tube burners, combustors, low-temperature radiant combustors.
Process equipment	Reformers, reactors, HIP equipments.
Waste incineration systems	Handling equipment, internals, cleanup.
Separation/filtration	Filters, substrates, centrifuges.
Refractories and related	Furnace linings, crucibles, flasks, etc.
Structural components	Beams, panels, decking, containers.

Addapted from: Chawla (2003).

2.1.3.1. Alumina fibers reinforced alumina matrix composites

The undesirable need for environmental barrier coatings to protect SiC based composites, adds motivation to develop oxide composite systems that are inherently stable in oxidizing environments (MARSHALL, et al., 2001).

All-oxide ceramic matrix composites have currently been developed for long term applications at high temperature and oxidizing environmental conditions, *e.g.* combustor walls of gas turbines for power generation or for propulsion, exhaust components, high temperature ducts, thermal insulation, heat exchangers and hot-gas filters (HACKEMANN, et al., 2010; MARSHALL, et al., 2001).

Despite the problem of oxidation at high temperature applications is solved with all-oxide composites, they show lower creep resistance, as compared to the covalently bonded SiC, due to their predominant ionic bond (HACKEMANN, et al., 2010). Nevertheless a composite matching oxide fiber and oxide matrix, *e.g.* Al_2O_3-Al_2O_3, is an answer to the problems of thermal expansion mismatch and chemical

compatibility between the elements of the composite (LEV, et al., 1995).

Alumina fiber reinforced alumina matrix composites should be sintered at temperatures below 1300 °C. Composites sintered above this temperature tend to fracture in a completely brittle mode due to fiber degradation. For non coated fiber, like Nextel™ 610, the optimum sintering temperature is 1200 °C, however pressure should be simultaneously applied to achieve high densities (LEE, et al., 2003).

2.2. POROUS MATERIALS

Porous materials are any solid material which contains cavities, channels or interstices. Most of the materials are porous to some extend and it is actually difficult to find or either prepare a real non-porous material, *i.e.* with null porosity. The degree of porosity influences directly on physical properties of the materials and its control is of great industrial importance. Porosity also affects the chemical reactivity of solids and the physical interaction of solids with gases and liquids (ROUQUEROL, et al., 1994).

Pores can be classified according to size, shape and availability to an external fluid. According to IUPAC, the classification of pore size is made as follows (STUDART, et al., 2006; ROUQUEROL, et al., 1994):

i.   Microporosity – pores width smaller than 2 nm;
ii.   Mesoporosity – pores width between 2 and 50 nm;
iii.   Macroporosity – pores width larger than 50 nm.

According to the availability to an external fluid, pores can be categorized into two main groups: *closed* and *open pores*. Closed pores are totally isolated from their neighbors. This type of pores is represented by the pore (a) in Figure 6. Open pores are those which have a continuous channel of communication with the external surface of the body, like pores (b), (c), (d), (e) and (f) in Figure 6. Yet, open pores can be sub-classified into *through pores*, like (c), (d) and (e), which are those open at two or more ends; or sub-classified as *blind pores*, like (b) and (f), open in only one extremity (ROUQUEROL, et al., 1994).

From the shape point of view, pores can be *cylindrical*, like (c) and (f); *ink-bottle* shaped like (b); *funnel* shaped like (d); or *slit* shaped (ROUQUEROL, et al., 1994).

The region marked as (g) in Figure 6 is not a pore, but roughness. To distinguish pore from roughness, an adopted convention consider that roughness are irregularities on the solid surface whose width is larger than its deepness (ROUQUEROL, et al., 1994).
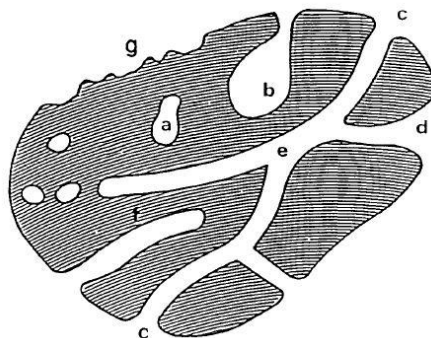
Figure 6 – Schematic cross-section of a porous solid showing different types of pores. Source: Rouquerol, et al (1994).

.

Applications for porous materials include (ISHIZAKI, et al., 1998):

i. Filters;
ii. Burners;
iii. Catalysts;
iv. Bioreactors;
v. Cells;
vi. Grinding wheels;
vii. Gas sensors;
viii. Gas separators;
ix. Electrodes;
x. Porous metals bearings;
xi. Thermal insulators;
xii. Capacitors;
xiii. Impact energy absorbers;

xiv.   Heaters and heat exchangers;
xv.   Molds;
xvi.   Surgical implants.

Porous materials can be produced by several routes, sintering powders compacts is one of them (ISHIZAKI, et al., 1998). Since the 1940's, porous metallic filters have been fabricated via powder-binder mixture extrusion. Corrosion-resistant metals, such as stainless steel, titanium, and nickel-based alloys, are the most suitable for filtration (GERMAN, 2005). In order to produce open porous materials with desired properties it is necessary to control powder properties, green body properties and sintering processes (ISHIZAKI, et al., 1998)

The main methods to characterize porous solids are (ROUQUEROL, et al., 1994):

i.   Stereology;
ii.   Radiation scattering;
iii.   Pycnometry;
iv.   Adsorption from a gas phase;
v.   Methods depending on interfacial curvature (intrusion, suction, maximum bubble pressure);
vi.   Fluid flow;
vii.   Calorimetric determinations (immersion calorimetry, gas or liquid adsorption calorimetry, thermoporometry);
viii.   Size exclusion chromatography (SEC);
ix.   Xenon NMR;
x.   Ultrasonic methods.

The replacement of solid material by voids in the component provides the materials some special features, such as (STUDART, et al., 2006):

i.   Low thermal mass;
ii.   Low thermal conductivity;
iii.   Controlled permeability;
iv.   High surface area;
v.   Low bulk density;
vi.   Low dielectric constant.

These properties can be tailored by changing type of porosity, *i.e.* open or close, pore mean size, pore size distribution, and pore morphology. All this microstructural aspects are highly influenced by the processing route used to produce a porous material (STUDART, et al., 2006).

Macroporous materials with open porosity can be made from particles or discontinuous fibers by partially sintering previous porous compacts, or by sintering powder mixtures that undergo reactions that lead to pore formation (FERNANDO, et al., 2005; INNOCENTINI, et al., 2009; STUDART, et al., 2006). These macroporous materials generally have porosity between 20 and 97% with pore size ranging from 400 nm to 4 mm (STUDART, et al., 2006).

Applications for macroporous ceramic materials are: hot-gas filtration, molten metal filtration, diffusion, dispersion rolls, ink pads for fingerprinting, high temperature thermal insulators, burners and numerous others (FERNANDO, et al., 2005; PRABHAKARAN, et al., 2005; STUDART, et al., 2006). Some of these components are made of ceramic materials or high temperature metal alloys (WOOD, et al., 2008), *e.g.* refractory metals and superalloys.

2.2.1. Hot-gas filters

Hot-gas filters are porous, closed-end tubes used to remove fine particles in a variety of operations (CHAWLA, 2003). Advanced power systems, such as the integrated gasification combined cycle (IGCC) and pressurized fluidized-bed combustion (PFBC), requiring gas turbines, are technologies to produce electricity and steam from coal and other hydrocarbon fuels with high efficiency and reduced emissions of sulfur dioxide and other pollutants. Removal of particulate and other emissions is required for these processes to protect the gas turbines against erosion and corrosion. To maintain a high thermal efficiency, the gas cleaning should be done without a previous cooling of the gases. Filtration then should be carried at over 350 °C for IGCC and 750 °C for PFBC. Moreover the filters must withstands backpressure pulses used on filter cleaning, *i.e.* removal of filter cake from the filters (DUO, et al., 1999; CHAWLA, 2003; INNOCENTINI, et al., 2009).

Other applications for hot-gas filters are coal gasification, incineration, catalytic recovery, catalytic processing, chemical and

petrochemical processing (FERNANDO, et al., 2002; CHAWLA, 2003).

After rapid development over the past decade, ceramic barrier filters have emerged as the most promising choice for hot-gas cleaning because of their high corrosion resistance and their ability to withstand high temperatures up to 1000 °C (DUO, et al., 1999).

Membranes with pore size ranging from 0.1 to 50 µm and porosity above about 40% are adequate for use in hot-gas filtration (FERNANDO, et al., 2005). Other requirements for hot-gas filters are: (DUO, et al., 1999; CHAWLA, 2003; FERNANDO, et al., 2002; INNOCENTINI, et al., 2009)

    i.   Long-term durability;
   ii.   High temperature capabilities;
  iii.   Alkali corrosion resistance;
   iv.   Cleanability;
    v.   Thermal shock resistance;
   vi.   Impermeability to particulates to be filtered;
  vii.   Optimized permeability to the gas;
 viii.   Lightweight;
   ix.   High toughness.
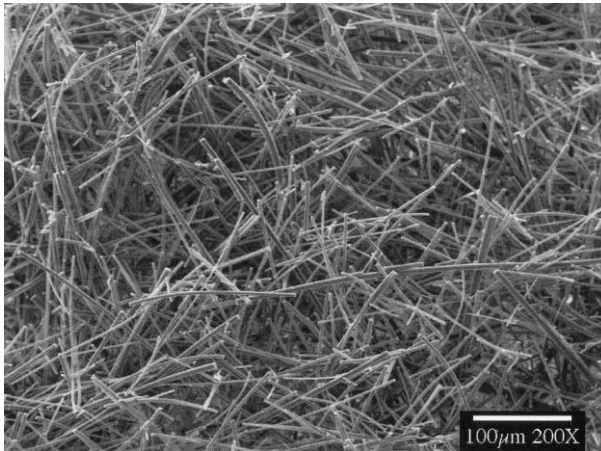
Figure 7 – Scanning electron microscope image of an alumina fiber filter membrane.
Source: Fernando, et al (2002)

Hot-gas filters membranes have been made of Saffil alumina fibers (90 wt.%) and a binder (10 wt.%). The pore size of these filters ranged from 1 to 23 μm, and was considered adequate for fine particles filtration (FERNANDO, et al., 2002). The microstructure of this type of membrane is shown in Figure 7.

2.2.2. Porous CMCs

There is an unconventional approach to design microstructures of composites that are damage tolerant. It relies on the weakness and low stiffness of a porous matrix to prevent damage from extending into the fibers (CINIBULK, et al., 2004). In this case the interface between the fibers and matrix might be strongly bonded (MARSHALL, et al., 2001). The failure strain in such CMCs is greater than in monolithic ceramic. Matrix crack energy is dissipated through multiple microfractures in the porous matrix, through weak interparticle bonding. These materials can retain their mechanical properties after long-term exposure to 1100°C during cyclic tension and fatigue (CINIBULK, et al., 2004). Processing of porous CMCs is easier because a high density is not required, thus low sintering temperatures can be used, avoiding fiber degradation (CHAWLA, 2003).

A process called WHIPOX™ (Wound Highly Porous Oxide CMC) was developed to produce such composites. A CMC composed by Nextel™ fibers in a porous mullite matrix was produced through this process. Rings and tubes of 20 and 250 mm long were sintered in air at 1300 °C for 60 min. The fiber volume fraction varied from 25 to 50 %. The porosity of the matrix was found to be over 60 vol.%. Figure 8 shows the microstructure of such composites (CHAWLA, 2003).
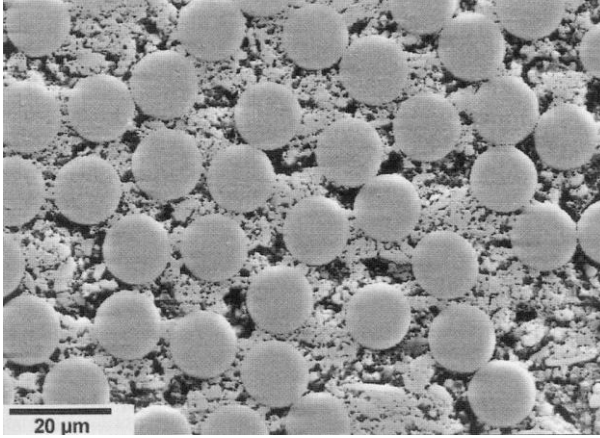
Figure 8 – Microstructure of the composite obtained by WHIPOX process.
Source: Chawla (2003).

Some industries are interested in the performance of porous CMCs. In particular energy related components, including porous radiant burners and hot-gas filters, need new materials to achieve higher operating temperatures, higher efficiency and longer service life. Radiant burners transfer a substantial fraction of their energy input directly to the process load as infrared radiation. Increased radiant output and fuel efficiency are the main benefits of using CMCs in radiant burners (CHAWLA, 2003).

Hot-gas filters are normally made of conventional monolithic ceramics that fail easily during cleaning operations, which involve backpressure pulses. The higher toughness, higher strength, higher creep resistance and thermal shock resistance of CMCs can be exploited in these components. Composites consisting of Nextel™ 610 or Nextel™ 312 fibers in a silicon carbide or alumina matrix have been made for filtering gas streams at temperatures up to 1000 °C (CHAWLA, 2003).

2.3. POWDER THERMOPLASTIC EXTRUSION

Extrusion is a process used to form long shapes with continuous cross section, such as rods, tubes, honeycombs and other infinite variety

of profiles. In the industry, extrusion is a common process used in the fields of metallurgy, ceramics, polymers and foodstuffs (RAUWENDAAL, 1986).

Powder thermoplastic extrusion is the molding process of particulate materials, in which a feedstock, *i.e.* powder-binder mixture, is forced through a die, where the compact extruded acquires the shape of the die channel (GERMAN, 2005).

After molding a debinding step is necessary to remove the binders and finally the component is sintered (GERMAN, 2005).

2.3.1.   Basics concepts on particulate materials processing

The processing of materials through powder, commonly known as particulate materials processing (PMP), is an attractive technology due to its replication capabilities and the viability to tailor the product application through the selective placement of phases or pores. Moreover PMP is in many cases the most competitive available technology that allows the production of materials such as composites, high-temperature ceramics, certain polymers, copper steels, refractory metals, intermetallics and cermets (GERMAN, 2005). These materials couldn't be processed in an economically viable way through conventional routes such as casting, and in many cases no other route is available.

The porosity control makes PMP an useful technology to produce components for filtration, lubrication and energy dissipation (GERMAN, 2005).

Particulate material processing consist basically on conforming or molding a chosen powder into a desired shape, and through a heat treatment called sintering, bond the particles together, making the initial individual particles become a solid body (GERMAN, 2005).

Two are the major routes to form a green body, compaction or shaping. The green body is the name given to the compact before sintering, it consist of powder and usually additives, that are added to improve conformability and/or help the compact retain its shape and improve mechanical strength during manufacturing steps that take place before sintering (GERMAN, 2005).

Compaction is applied for granulates and powders with low amount of additives, whereas shaping is applied for plastic consistence

feeds and slurries containing high amount of additives (GERMAN, 2005).

Compaction technologies can be divided into die compaction, cold isostatic compaction[2], hot pressing and rolling pressing. Examples of shaping technologies are injection molding, plastic extrusion, thermoplastic extrusion, rolling, thermosetting and thermoplastic pressing, porcelain pressing and slurry techniques[3] (REED, 1995; GERMAN, 2005).

2.3.2. Powders

Powder processing technologies deal generally with particles in the range from some dozen nanometers to hundreds of microns. The main aspects of the powders to be characterized are (GERMAN, 2005):

   i.   Particle size and particle size distribution (PSD);
   ii.   Particle shape;
   iii. Particle agglomeration;
   iv.   Surface area;
   v.   Interparticle friction;
   vi.   Flow and packing;
   vii. Internal structure;
   viii. Composition, homogeneity and contamination.

These characteristics are imposed by the material and especially by the powder synthesis and fabrication technique.

The shape of the particles is a very important factor on the processing and affects directly the packing, flow and compressibility (GERMAN, 2005). Figure 9 gives a collection of possible particles shapes. The most appropriate way to characterize the particle shape is through scanning electron microscopy (SEM). Light scattering particle

---

[2] Also known as cold isostatic pressing, CIP. A variant of CIP is hot isostatic pressing, HIP, in which a previously sintered body is subjected to a pressurized hot-gas (REED, 1995). HIP is considered an enhanced sintering process rather than an compaction process.
[3] Slurry techniques comprise: Slip casting, tape casting, pressure casting, slurry pressing, vacuum casting, centrifugal casting, gel casting, casting concrete and others.

size analyzers and gas adsorption (BET) are other important techniques to characterize PSD and surface area of powders (GERMAN, 2005).
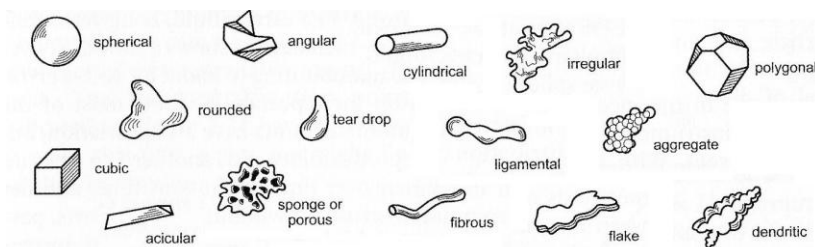
Figure 9 – Collection of possible particle shapes.
Source : German (2005)

2.3.3. Additives

Additives are inorganic or organic chemicals used to tailor powder characteristics (GERMAN, 2005). They can be categorized as follows:

i. *Solvent* – used as a temporary liquid to disperse other additives;
ii. *Dispersant or deflocculant* – separate particles braking agglomerates;
iii. *Coagulant or flocculant-* promotes particle agglomeration;
iv. *Plasticizer* – used to lower the viscosity of the mixture and modifies the viscoelastic properties of a condensed binder film on the particles;
v. *Surfactant or wetting agent*– improves binder-powder wetting;
vi. *Foaming and antifoaming agent* – controls the formation of bubbles in the mixture;
vii. *Thickener* – increases the apparent viscosity of the mixture;
viii. *Binder* – provides green strength;
ix. *Lubricant* – minimizes tool wear;

      x.   *Preservative* – reduces enzymatic degradation of a binder (GERMAN, 2005; REED, 1995).

2.3.3.1. Binders

Binders are polymers molecules that form a bridge between particles and provide interparticle binding action (REED, 1995). The combination of powder and binder is the so called feedstock (GERMAN, 2005).

There are several materials that can be used as binders such as organic matter of clays, natural gums, waxes, vinyl, cellulose, polyethylene glycol, resins (thermoplastics), gels, low-temperature reaction bonds, hydraulic cements, and so on (REED, 1995).

Binder's most important function is to improve the strength of the as-formed product allowing it to be handled before the product is densified by sintering (REED, 1995).

Polymers and waxes derived from petroleum such as low density polyethylene (LDPE), high density polyethylene (HDPE), polypropylene (PP), polystyrene (PS) and paraffin wax are commonly used. Some natural waxes like carnauba wax (derived from the leaves of a Brazilian palm tree), candelilla wax and beeswax are also widely used (GERMAN, 2005; REED, 1995).

Polymers resins, *e.g.* PE, PP and PS, are usually added to form a bonding matrix. The strength, melting temperature and viscosity of these thermoplastics increase with the average molecular weight (REED, 1995).

2.3.3.2. Surfactants

Surfactants are molecules which have a polar group in one extremity and have a nonpolar chain on the other side. The polar group attracts polar molecules and is called lyophilic group. The nonpolar group, usually a hydrocarbon chain, is the lyophobic group (REED, 1995). Figure 10 shows a sketch of a surfactant and its behavior on different means.

Surfactants improve the compatibility of the solid with the liquid medium, when adsorbed at the interface solid-liquid, reducing the surface tension γ_{SL}. The driving force for the adsorption of these molecules at a surface or interface is the reduction of Gibbs free energy ΔG (REED, 1995).
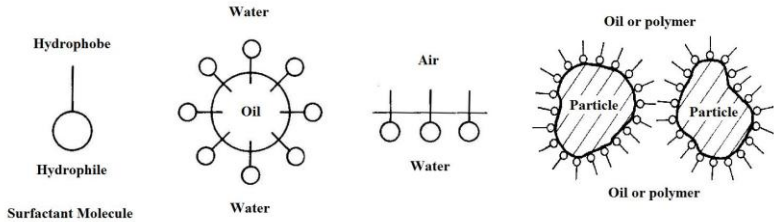
Figure 10 – Surfactant sketch showing its hydrophilic and hydrophobic groups, and the behavior of a surfactant in different means.
Source: Reed (1995).

Examples of surfactants are: stearic acid, ethoxylated nonylphenol, ethoxylated tridecyl alcohol, sodium stearate, sodium disopropylnaphtalene sulfonate, dodecyltrimethylammonium chloride and sodium dodecyl sulfate (REED, 1995; GERMAN, 1990).

2.3.3.3.   Plasticizers

Ceramic systems containing a binder are molded above the glass transition temperature T_g of the binder. Plasticizers usually have a smaller molecule than the binder. This molecules are distributed among the chains of the binder reduces the Van der Waals forces that binds the polymer molecules together. This makes the binder to soften and increase its flexibility, but also reduces its strength. Essentially the plasticizer reduces the T_g of the polymer (REED, 1995). In general the plasticizer have a low melting point (T_m).

Oils and waxes are used as plasticizers in the case of thermoplastic binders such as PE and PS. Stearic acid and oleic acid behave as plasticizers for waxes (REED, 1995).

2.3.4. Rheology

Rheology is the science of deformation and flow (REED, 1995). The study of the rheological behavior of a fluid material is of high importance for the design and selection of the equipments for processing a feedstock (GERMAN, 1990).

The most important rheological property of a feedstock is the viscosity. The second important property is the elasticity. Elastic materials exhibit a shape memory effect, which implies that part of the submitted deformation is recovered after the stress is ceased. Feedstocks exhibit both viscous and elastics characteristics and are therefore termed viscoelastic fluids (GERMAN, 1990).

One of the effects of the viscoelasticity of polymers is the phenomenon known as extrudate swell[4], in which the diameter of the extrudate out of the die is considerably higher than the diameter of the die orifice. This occurs because the viscoelastic fluid recovers part of its deformation − the elastic portion − underwent when it was forced into the die (SHENOY, 1999)

2.3.4.1. Shear flow

The steady simple shear flow can be described by the scheme of Figure 11. The situation describes a fluid being sheared by two plates of area A separated by a distance dx_2. The lower plate moves with a velocity v_1 and the upper plate with a velocity v_1+dv_1. The differential velocity dv_1 is imposed by the force f.

The velocity gradient $\dot{\gamma}$ [s^{-1}] is also called shear rate and can be defined as shows Equation 2, where the term dx_1/dx_2 describes the shear strain γ. The shear stress τ [Pa], necessary to shear the fluid and maintain a laminar flow, can be defined as it is shown on Equation 3. Finally Equation 4 defines the viscosity η [Pa·s], referred to as steady state viscosity, which correlates shear rate and shear stress.

---

[4] Also known as die swell, jet swell, Barus effect or Merrington effect (SHENOY, 1999).
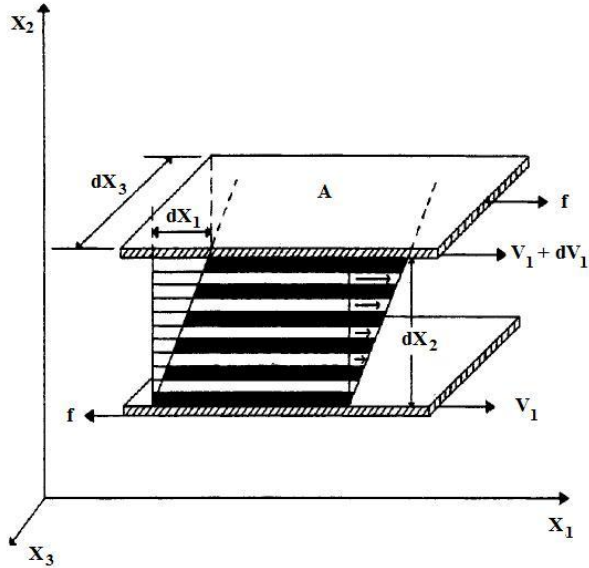
Figure 11 – Simple shear flow of a fluid between two plates, in which one has higher velocity than the other. Source: Adapted from Shenoy (1999).

Equation 2
$$\dot{\gamma} = \frac{dv_1}{dx_2} = \frac{d}{dx_2}\left[\frac{dx_1}{dt}\right] = \frac{d}{dt}\left[\frac{dx_1}{dx_2}\right]$$

Equation 3
$$\tau_{12} = \frac{f}{A}$$

Equation 4
$$\eta = \frac{\tau_{12}}{\dot{\gamma}}$$

Viscosity is the resistance of the fluid to any irreversible positional change of its volume elements (SHENOY, 1999). In other words, viscosity is the resistance of the fluid to shear. Equation 4 is valid for Newtonian fluids in which the shear stress τ is linearly dependent on the velocity gradient $\dot{\gamma}$ (REED, 1995). Nevertheless the nature of the polymers and the filled polymers bring them to the category of non-Newtonian fluids (SHENOY, 1999).

2.3.4.2. The effect of shear rate and time on non-Newtonian fluids

For non-Newtonian fluids, the viscosity can be a function of shear rate and time (SHENOY, 1999), and the linear relationship between shear rate and shear stress may not exist.

In general non-Newtonian fluids exhibit one of the following features:

    i.   Shear rate dependent viscosity in certain shear rate ranges, with or without elastic behavior;

    ii.   Yield stress;

    iii.   Time-dependent viscosities at fixed shear rates (SHENOY, 1999).

Depending on which of the previous characteristics a fluid exhibit, it can be classified in one of the following models (REED, 1995; SHENOY, 1999):

    i.   *Pseudoplastic* – its viscosity decreases with increasing of shear rate, also called shear thinning fluids, $\partial \eta / \partial \dot{\gamma} < 0$;

    ii.   *Dilatant* – its viscosity increases with increasing shear rate, also called shear thickening fluids, $\partial \eta / \partial \dot{\gamma} > 0$;

    iii.   *Bingham* – flows just after the shear stress exceeds a yield stress, then shows a linear relationship between shear rate and shear stress;

    iv.   *Pseudoplastic with yield stress* – its viscosity decreases with increasing of shear rate and additionally exhibits a yield stress;

    v.   *Dilatants with yield stress* – its viscosity increases with increasing of shear rate and additionally exhibits a yield stress;

    vi.   *Thixotropic* – exhibits a reversible decrease in shear stress with time at a constant temperature and shear rate;

    vii.   *Rheopectic* – exhibits a reversible increase in shear stress with time at a constant temperature and shear rate;

    viii.   *Viscoelastic* – possesses an elastic component apart from the viscosity, showing properties of viscous liquids and elastic solids.

Figure 12 shows the variation of shear stress with shear rate for some of non-Newtonian fluids models. Polymers – filled or not – can be pseudoplastics with or without yield stress, thixotropics and viscoelastics (SHENOY, 1999).
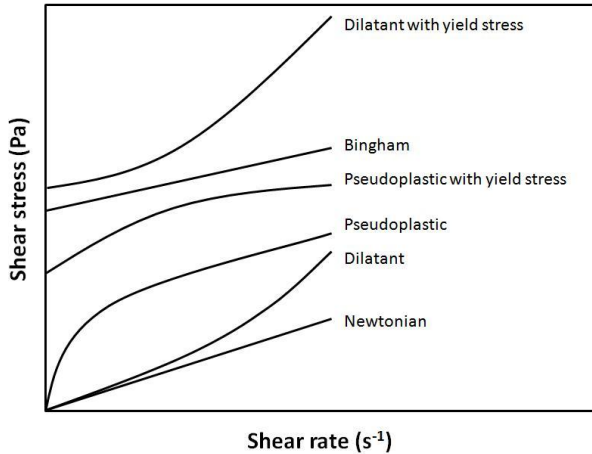
Figure 12 – Newtonian and non-Newtonian models of fluid behavior.
Adapted from: Reed (1995)

Fluids containing large molecules and suspensions containing non-attracting anisometric particles, when undergo a laminar flow may have the molecules or particles oriented. As orientation reduces the resistance to shear, the stress necessary to increase the shear rate diminishes with increasing shear rates (REED, 1995). This gives the pseudoplastic characteristic of the feedstocks, in which the particles have a major effect on the mixture behavior (GERMAN, 1990).

2.3.4.3.   Effect of temperature

The viscosity of most of the fluids is temperature and pressure dependent. The viscosity of a fluid decreases with the increase of temperature. And the viscosity η varies exponentially with the absolute temperature T as shown in Equation 5, where T is the temperature in Kelvin, η_0 is the viscosity at a reference temperature T_0, k is the

Boltzmann's constant, and E is a material specific constant which represents the activation energy for viscous flow. High values of E indicate a high sensibility to temperature change (GERMAN, 1990).

Equation 5 $$\eta = \eta_0 exp\left[\left(\frac{E}{k}\right)\left(\frac{1}{T}-\frac{1}{T_0}\right)\right]$$

   Figure 13 illustrates the application of Equation 5 for a binder system composed by polyethylene and stearic acid, with activation energy of 32 kJ/mol (GERMAN, 1990). The plot of the natural logarithm of the viscosity, versus the inverse of the temperature is the so called Arrhenius plot.
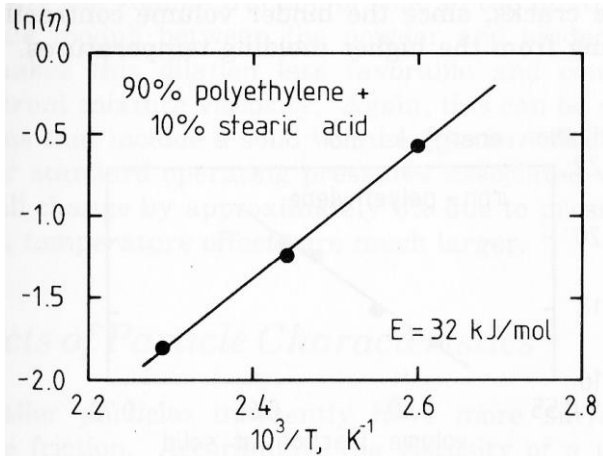
Figure 13 – Arrhenius plot of a natural logarithm of the viscosity for a polyethylene and stearic acid mixture.
Source: German (1990).

   Polymers loaded with particles, in spite they exhibit higher viscosity, are more temperature sensitive than pure polymers. This happens because of the difference in thermal expansion coefficients of the polymers and the particles. The polymer expands more than the particles and the solid volume fraction decreases with the increase of temperature. This means that the apparent activation energy E_a is larger for loaded systems (GERMAN, 1990).

2.3.4.4.   Effect of solid volume fraction

The viscosity of a loaded polymer increases with the addition of powder in the system. Furthermore, there is a limit of solids that can be added before the viscosity becomes essentially infinite, and the mixture gets too stiff to be considered viscous. For monosized spheres, this limit is equal to the maximum random packing condition of 63,7 vol.% of solids (GERMAN, 1990), as shown in Figure 14.

Einstein provided an equation to predict the viscosity of suspensions with low solid volume fraction in which the relative viscosity η_r, that is the viscosity of the loaded fluid divided by the viscosity of the pure fluid, has a linear relationship with the solid volume fraction ϕ, as shown in Equation 6 (GERMAN, 1990), where $\partial\eta/\partial\phi > 0$.

Equation 6 $$\eta_r = 1 + 2.5\phi$$

Einstein's viscosity equation postulates a suspension so diluted that there is no interaction between particles (MOONEY, 1951). Therefore this equation fits well just with low content of solids, *i.e.* less than approximately 15 vol.%, and the relationship between relative viscosity and solid volume fraction departs from the linearity with higher contents of solids (GERMAN, 1990), as can be seen in Figure 14.
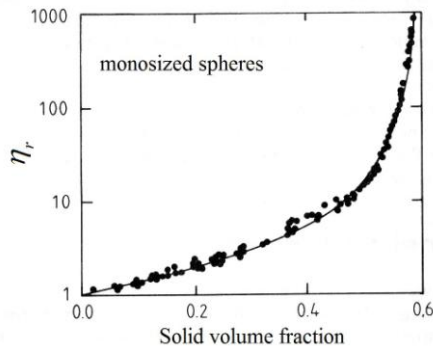
Figure 14 – Relative viscosity versus volume fraction of monosized glass spheres.
Source: German (1990).

Many other models have been proposed so far, most of them based on Einstein's viscosity equation, to predict the change in viscosity with particles loading on a powder-binder mixture. Most of the models, nevertheless, assume hard, solid and spherical particles (GERMAN, 1990), and many of them express η_r as a function of the relative solids loading ϕ_r, that is the ratio ϕ/ϕ_m. Moreover, the models have in common two boundary conditions that must be satisfied.

First, the relative viscosity η_r, must be equal to unity for pure binder, *i.e.* the viscosity of the mixture η approaches the viscosity of the binder η_b for solid contents close to zero, as represented by Equation 7.

Equation 7
$$\lim_{\phi \to 0} \eta_r (\phi) = 1$$

Second, there is a maximum solid volume fraction ϕ_m, and the viscosity approaches to infinite when the solid volume fraction approaches ϕ_m, as it is shown on Equation 8 (GERMAN, 1990).

Equation 8
$$\lim_{\phi \to \phi_m} \eta_r (\phi) = \infty$$

This happens because, when the solids content is too high, the particles are practically in permanent contact with each other, and the amount of liquid is sufficient only to fulfill the interstices between the particles, as shown in Figure 15, and do not contribute to decrease the viscosity of the system. This liquid in the interstices is immobile and don't participates on the basic flow process, therefore the viscosity increases dramatically when the solid content reaches this condition. A little amount of liquid is enough to form a film between the particles and play the role of a lubricant. This mobile liquid reduces the frictional interaction of the particles reducing radically the system viscosity. Therefore, the suspension viscosity depends on the amount of mobile fluid and not on the total amount of fluid (GERMAN, 1990).
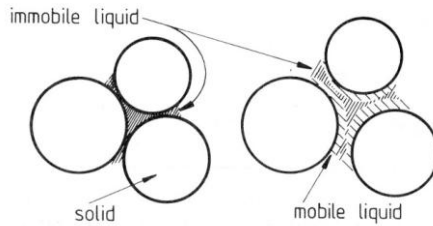
Figure 15 – Sketches showing the immobile liquid when the solid volume fraction ϕ reaches the maximum value ϕ_m, and the mobile liquid when $\phi < \phi_m$.
Source: German (1990).

Although viscosity data for suspensions of solid spheres are quite numerous, the agreement among the various investigations has been rather poor, specially on the high concentration regime (FRANKEL, et al., 1967), *i.e.* high filling level. This makes it difficult to predict the behavior of suspension with high contents of solids and generate a universal model.

Reasons pointed for the conflicting results are: wall effect in capillary viscometers, slip at particle surfaces, insufficient dispersion, adsorption, turbulence, sedimentation, and others (FRANKEL, et al., 1967).

Some of the suggested models that represent the relative viscosity as a function of solid volume fraction are given by Equation 9 to **Fehler! Verweisquelle konnte nicht gefunden werden.** that follows, where *A*, *B*, *k* and *n* are constants that depend on the system (GERMAN, 1990; REED, 1995).

Equation 9 represents the model proposed by Eilers. It is an empirical based model in which the constant *A* is a factor related with the inverse of the maximum filling level ϕ_m, suggested to be 1.35 by Eilers as the inverse of 0.74, that is the packing factor for monosized spheres on its close-packed structure. His experimental data however, fitted better for a factor of 1.28 and 1.30, what would lead to packing factors of 0.78 and 0.77 respectively (EILERS, 1941; EILERS, 1949).

Equation 9
$$\eta_r = \left(1 + \frac{1.25\phi}{1 - A\phi}\right)^2$$

where $$A = \frac{1}{\phi_m} = \frac{1}{0.74} = 1.35$$

Mooney has also made his contribution and proposed the model of Equation 10. This model introduced the concept of crowding factor λ_{12}, which is a function of the ratio r_1/r_2 of the particle radius in a bimodal particle size distribution. Mooney calls the crowding effect the occupancy of the remaining free volume, between particles of size r_1, by the particles of size r_2. The constant k is a particular value of λ_{11} called the self-crowding factor, which by a purely geometric argument must be higher than 1.35 and smaller than 1.91 (MOONEY, 1951).

Equation 10 $$\eta_r = exp\left(\frac{2.5\phi}{1-k\phi}\right)$$

where $$1.35 < k < 1.91$$

The model of Krieger and Dougherty, Equation 11, takes into consideration the non-Newtonian behavior, attributed to ability of the shear stress, transmitted through a continuous medium, to orient or distort the suspended particles in opposition to the randomizing effects of Brownian motion. The variation of viscosity with shear rate is the result of the decrease of resistance to flow offered by the oriented or distorted arrangement. The appearance of this non-Newtonian behavior is related with crowding. Such affirmation derives from the fact that these systems show Newtonian behavior up to relatively high concentrations, 20 vol.% (KRIEGER, et al., 1959).

Equation 11 $$\eta_r = \left(1 - \frac{\phi}{\phi_m}\right)^{-[\eta]\phi_m}$$

Krieger and Dougherty's model derived from a modification of Mooney's functional analysis, where the constant $[\eta]$ is the "intrinsic viscosity" and should be close to 5/2 (KRIEGER, et al., 1959).

Frankel and Acrivos achieved one purely theoretical model, with no empirical constants. Their model, shown on Equation 12, is valid for high concentrations and can be applied for suspensions where ϕ_r

approaches to unity, in other words, when ϕ tends to ϕ_m (FRANKEL, et al., 1967).

Equation 12
$$\eta_r = A \left[\frac{(\phi/\phi_m)^{1/3}}{1-(\phi/\phi_m)^{1/3}} \right]$$

On Equation 12 the constant A is related with the region of influence of the particle. The region of influence, called cell by the authors, can be of different geometries. Therefore, the constant A can represent different numerical values, being fairly sensitive to the assumed geometry of the cell. For instance, a spherical cell results in a value of 9/8 and a cubic cell results in a value of $3\pi/16$ (FRANKEL, et al., 1967).

Chong and co-workers have also achieved an empirical model, Equation 13, of the same type of Eilers', however with a different constant (CHONG, et al., 1971).

Equation 13
$$\eta_r = \left[1 + 0.75 \left(\frac{\phi/\phi_m}{1-\phi/\phi_m} \right) \right]^2$$

Quemada proposed also an equation including the pseudoplasticity in his model, like Krieger and Dougherty did, but furthermore considered the diffusion coefficient D of particles in the medium. So his general formulation considered that viscosity and diffusion are both functions of the solid volume fraction ϕ and shear rate $\dot{\gamma}$, in mathematical notation $\eta(\phi, \dot{\gamma})$ and $D(\phi, \dot{\gamma})$ (QUEMADA, 1977).

The model of Quemada assumed a rectangular concentration profile with no effective diffusion (QUEMADA, 1977), and a rectangular velocity profile. This assumptions were based on a two-phase flow with a concentrated axial core and a marginal layer, close to the wall, with null concentration, $\phi = 0$. Another bound condition was that when $\phi \to \phi_m$, not only $\eta \to \infty$, but also $\partial \eta / \partial \phi \to \infty$ (QUEMADA, 1977). Quemada's approach leads to a very simple model, represented by Equation 14.

Equation 14
$$\eta_r = \left(1 - \frac{\phi}{\phi_m} \right)^{-2}$$

The models discussed above can be used to predict the relative viscosity for a certain solid loading, but there is a range of solid loading considered the optimal loading for processing. In practice, this optimal loading contains less powder than the maximum filling level (GERMAN, 1990).

One of the reasons is the extremely high viscosity close to the maximum filling level. Another reason is that the difference between densities of powder and binder implies in a large sensitivity to the inherent fluctuations that occurs in compounding a mixture, which is made in a weight basis (GERMAN, 1990). That means that a small error on weighting of powder and binder during compounding, represent a considerable change in volume fraction when working near the maximum filling level, as shown in Figure 16.
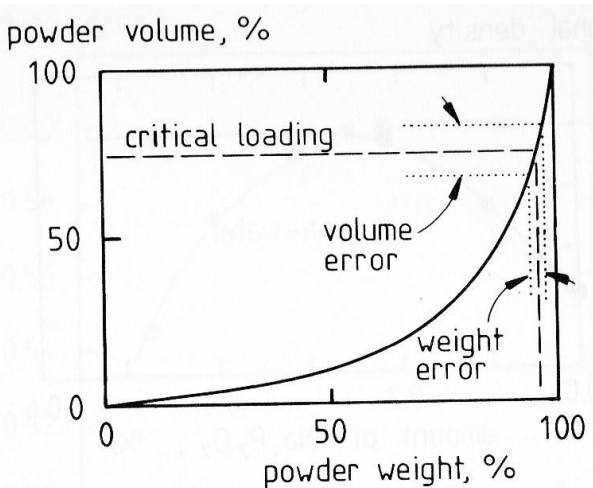
Figure 16 – Powder volume fraction versus powder weight fraction. A small error in the weight is amplified in the volume loading near the maximum loading.
Source: German (1990).

Since the viscosity of the mixture changes very rapidly with the solid volume content in the region close to the maximum filling level, small differences of solid volume fraction can be amplified into large viscosity shifts as shown in Figure 17 (GERMAN, 1990).
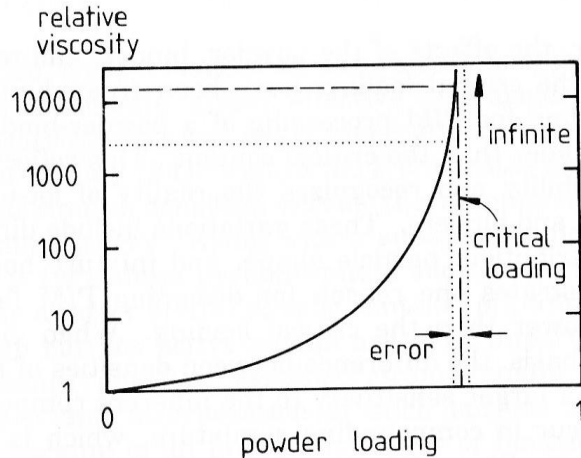
Figure 17 – Relative viscosity versus powder volume loading. Small error in volume loading represents large changes in viscosity near maximum loading. Relative viscosity can become infinite for errors that achieves higher loading than the maximum.
Source: German (1990).

2.3.4.5.   Effect of particle characteristics

The size of the particles influences the viscosity of the mixture. The smaller the particle size, the higher is the surface area and higher is the interaction between particles, increasing the interparticle friction. For this reason the viscosity of feedstocks is inversely proportional with the particle size. This, though, has just a considerable effect for submicrometer particle size (GERMAN, 1990).

More relevant than the particle size is the particle size distribution. PSD influences considerably the viscosity of the system. Mixing powder with different sizes improve the packing density and thereby decrease the viscosity at any given solid volume fraction (GERMAN, 1990). This is because the small particles can occupy the interstices of the larger ones, once occupied by immobile fluid. The excess of fluid becomes mobile fluid and is available to contribute with the flow process. Moreover smaller particles can be interposed between

larger particles and act as a lubricant facilitating the rotation of larger particles (SHENOY, 1999).

The greater the packing density, the lower the relative viscosity for the same solid volume fraction. Therefore a wide PSD will give a lower viscosity than a narrower one, allowing a higher solid loading (GERMAN, 1990). Figure 18 shows the effect of the percentage of small particles mixed with larger particles on the viscosity, with a size ratio of 21 and solid content of 55 vol.%.
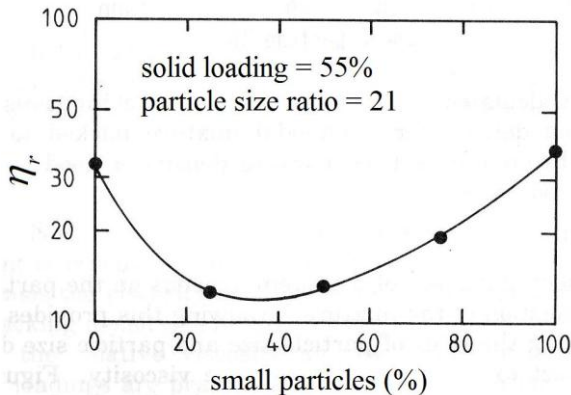
Figure 18 – Effect of the percentage of small particles on relative viscosity for a bimodal mixture of spheres at a solid content of 55 vol.% and a size ratio of 21.
Source: German (1990).

The shape of the particles is also crucial and non-spherical particles increase the viscosity of the systems due to the lower inherent packing density and higher interparticle friction. Irregular particle shape and agglomerated particles decreases the maximum packing density, increasing therefore the relative viscosity (GERMAN, 1990).

The presence of fibers in the feedstocks will increase the viscosity, increase the shear thinning effect, due to alignment, and increase the strength of the green body after solidification (GERMAN, 1990).

As more the ratio lengh-diameter L/D departs from the unit, lower is the maximum loading and higher is the relative viscosity for a same solid content (GERMAN, 1990), as can be seen on Figure 19.
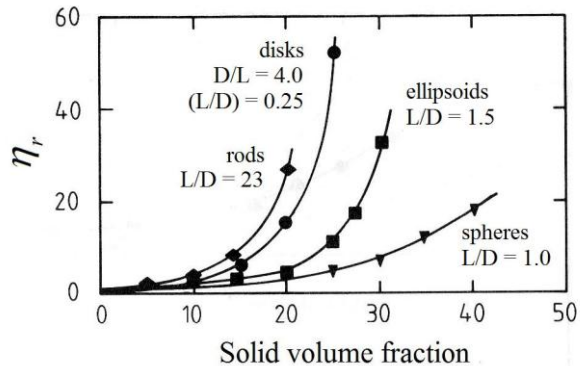
Figure 19 – The effect of particle shape on the relative viscosity for a suspension of glass particles in water. The ratio length-diameter is also indicated to show its direct influence.
Source: German (1990).

2.3.4.6. Rheometry

Rheometry is the measurement arm of rheology and is used to quantify the rheological parameters of practical importance. A rheometer can measure the force generated to an applied deformation mode, or measure the deformation caused by an applied force mode (SHENOY, 1999).

Rheometers can be divided into rotational and capillary types. The most common tests applied to polymer-powder mixtures are (GERMAN, 1990; SHENOY, 1999):

i.   Capillary plunger extrusion;
ii.   Capillary screw extrusion;
iii.   Rotating coaxial cylinders;
iv.   Rotating parallel plates;
v.   Torque measurements in mixing rheometers – torque rheometer;
vi.   Rotating cone-on-plate tests.

A capillary rheometer measures the pressure drop and the flow rate associated with the forced flow through a small capillary cylinder (GERMAN, 1990). Figure 20 shows the main features of a constant plunger speed with circular orifice capillary rheometer.
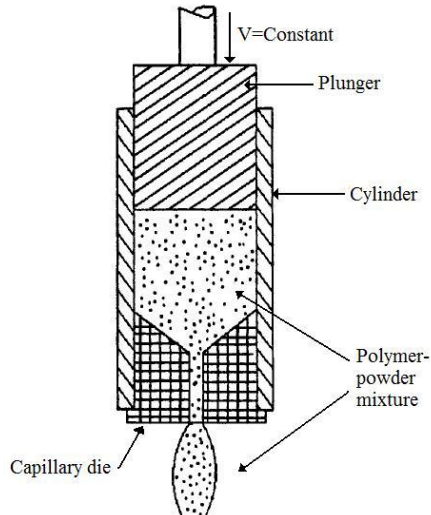
Figure 20 – Schematic diagram of a constant plunger speed with circular orifice capillary rheometer.
Adapted from: Shenoy (1999).

The torque rheometer is also an instrument that allows rheological studies in the basis of torque measurements as a function of temperature, time and rotation speeds. It consists in melting the mixture inside a chamber and, with two rollers rotating in opposite directions, mix the melt measuring the torque necessary for the mixing. Different types of rollers, that impose different shear stresses to the mixtures, can be also selected. The problem of the torque rheometer is that its geometry and the three-dimensional nature of the flow field in the chamber make it difficult to evaluate rheological properties of melts (CHENG, et al., 2001), in a way that torque and rotation speed data cannot be easily converted into shear stress and shear rate, respectively.

Another issue is that, differently from other rheometers, the mixer chamber of the torque rheometer is usually only partially filled – 65~90% of the chamber volume, while 70% is a standard value

(CHENG, et al., 2001). The cavities present in the partial filled chamber influence the measurement. Figure 21 shows a schematic diagram of a torque rheometer chamber.
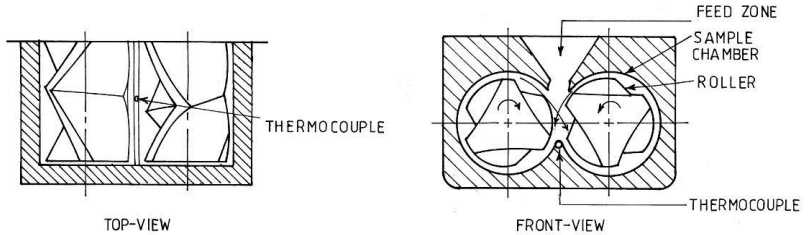
Figure 21 – Schematic diagram of the chamber of a torque rheometer.
Adapted from: Maity, et al. (1999)

2.3.5. Mixing

Mixing is the first step in the preparation of the feedstock for molding. Uniform quantities of particles and binder are needed in all portions of the mixture, and intensive mixing is needed to ensure that each interstice between the particles contains a representative combination of the binder components. For particulate materials processing it is desired that every portion of the mixture contains an equal concentration of powder and the same particle size distribution (GERMAN, 1990).

The inhomogeneities can occur in two forms, separation of binder from powder, and segregation according to particle size, shape or density within the binder. The segregation leads to uneven densities and distortion of the final product. Size segregation is more problematic for high particle size ratios or wide particle size distributions, and in practice, segregation can be minimized by maintaining a high binder viscosity (GERMAN, 1990).

Many indexes for mixture homogeneity have been proposed, including measurements of the torque and energy during mixing, shear modulus, viscosity, density, concentration and particle size in the mixture. From a rheological point of view, pseudoplastic behavior is associated with a well mixed system, while instability with shear rates relates to poorly mixed systems (GERMAN, 1990).

2.3.5.1. Mixing kinetics and practice

The initial action of mixing is to break clusters by shear. With continued mixing, cluster size decreases and binder becomes dispersed between the particles (GERMAN, 1990).

The mixing torque can be used to determine the homogeneity of the mixture as shown in Figure 22. Initial low torque corresponds to the plain binder. When the powder is added the torque increases to a high level. As the agglomerates break apart and the immobilized liquid is released the torque decreases. As more liquid is released the torque decreases, initially in an exponential manner. At the steady-state, *i.e.* no change in torque with time, the rate of mixing equals to the rate of demixing. After achieving the steady-state, any change in the mixer speed or temperature will cause a torque shift (GERMAN, 1990).
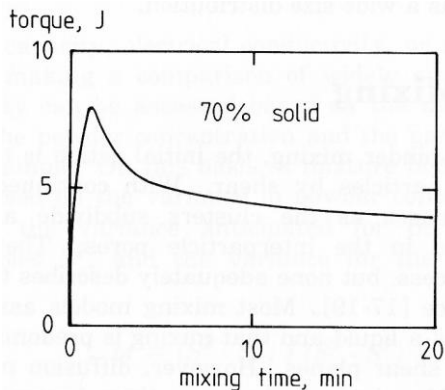
Figure 22 – Mixing torque as a function of mixing time. Steady-state torque is associated with mixture homogeneity.
Source: German (1990)

To attain homogeneity, several details must be considered in practice. First the temperature must be enough to both lower the viscosity and to reduce the yield point of the mixture. Cavitation defects may occur if the temperature is too low and the effects of the yield strength are still present. A too high temperature can degrade the binders or cause separation of powder from the binder (GERMAN, 1990).

The practice of mixing should occur as follows (GERMAN, 1990):

i.   The binder of highest melting point is added to the preheated chamber;

ii. Selectively lower temperature binders are added with appropriate temperature reductions when necessary, to avoid evaporation or degradation;

iii. As the chamber becomes fuller, mechanical work increases and considerable heating may occur. Temperature control is important in this case;

iv. The powder is then added.

v.   At this point the temperature may reduce drastically if the powder has a high heat capacity (metallic powders mainly);

vi. The mixing torque, after the powder has been added, becomes relatively higher, because of inhomogeneities, interparticle friction, and decrease in temperature;

vii. As temperature and homogeneity increases, the torque reduces fast;

viii. Finally, when temperature is stable and a good level of homogeneity is achieved, the torque reaches a steady-state value;

2.3.6.   Extrusion molding

The extrusion process consists basically in pushing or forcing a material through an opening. Extruder die refers to the part of the machine containing the opening through which the material is forced. As the material is squeezed through the die, it acquired the shape of the die opening. The extruded product is referred to as the extrudate (RAUWENDAAL, 1986).

Extruders are the most important piece of machinery in the polymer processing industry, but also many different materials can be formed through extrusion process, *e.g.* metals, clays, ceramics, foodstuffs, etc. Materials can be extruded in the molten or in the solid state. Polymers are generally extruded in the molten state; nevertheless, the solid state extrusion can be used for some specific applications (RAUWENDAAL, 1986).

2.3.6.1. Plunger extruders

Plunger or ram extruders are simple in design, rugged and can only operate in a discontinuous fashion. Figure 23 shows schematically a plunger extruder used in powder thermoplastic extrusion. Plunger extruders are able to generate very high pressures (RAUWENDAAL, 1986).
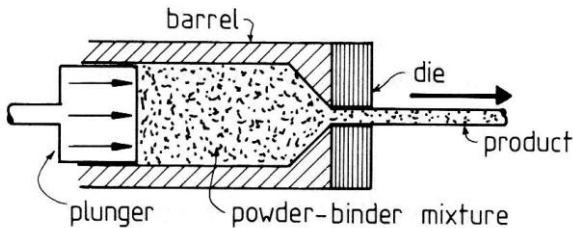
Figure 23 – Sketch of a plunger extruder used in thermoplastic powder extrusion.
Source: German (1990).

This type of extruder is being used for small shot size molding machines and other applications that take advantage of its outstanding pressure generation, *e.g.* extrusion of ultrahigh molecular weight polyethylene (UHMWPE) and polytetrafluoroethylene (PTFE) that requires pressures in the order of 300 MPa (RAUWENDAAL, 1986).

Another well known application of plunger extrusion is the solid state extrusion. This technique was borrowed from the metal industry, where solid state extrusion has been used for decades. Solid state extrusion consists in force the polymer through a die in a temperature below its melting point. This causes a drastic deformation in the material, which leads to an accentuated chain orientation, more effective than that which occurs in conventional melt extrusion. Thus extraordinary mechanical properties can be attained (RAUWENDAAL, 1986).

Apart from the extraordinarily high mechanical properties, solid state extrusion provides some other benefits such as (RAUWENDAAL, 1986):

      i.   Virtually no extrudate swell occurs;

     ii.   Higher surface quality and low surface friction coefficient can be obtained;

    iii.   Polymers maintain the high tensile strength at higher temperatures;

    iv.   Melting point of the polymer is increased with the high molecular orientation.

2.3.6.2. Extrusion pressure

Die forming is a pressure consuming, in other words, it requires pressure to occur. The pressure necessary for the extrusion process to occur depends on (RAUWENDAAL, 1986):

      i.   Geometry of the flow channel;

     ii.   Flow properties of the material to be extruded;

    iii.   Temperature distribution in the material to be extruded;

    iv.   Flow rate throw the die.

2.3.6.3. Extrudate swell

It is a typical phenomenon on the polymer melt extrusion process which consists in the swelling of the extrudate as it leaves the die, as can be seen in Figure 24. The responsible for this phenomenon is the viscoelasticity of the polymer, more precisely the elastic recover of the deformation through which the polymer was submitted in the die (RAUWENDAAL, 1986).

The amount of swelling that the extrudate undergoes depends on (RAUWENDAAL, 1986; CHEREMISINOFF, 1987; DEALY, et al., 2000):

      i.   Shear rate;

     ii.   Polymer molecular weight.

    iii.   Time during which the extrudate is held under deformation;

iv.   Temperature;

Extrudate swell is intimately related with the polymer chains orientation. When the extrudate undergoes higher shear rates, the polymer chains orient more and consequently more elastic recover can occur. Moreover, if a polymer has longer chains, *i.e.* higher molecular weight, elastic recover is even higher due to rearrangement of oriented chains, consequently, the extrudate swell is also higher (CHEREMISINOFF, 1987).

The elastic recover is time-dependent, which means that it only occurs after a limited time subsequent to the undergone deformation. In other words, the deformation can be recovered to a large extent shortly after the occurrence of the deformation. However, after longer times the recoverable deformation reduces. That is the reason why short length dies create larger swelling than long length dies. In longer dies, a certain amount of relaxation occurs in the polymer structure before it leaves the die (RAUWENDAAL, 1986).
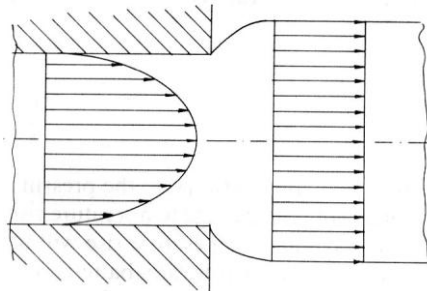
Figure 24 – Sketch of an extrudate suffering swelling in the die exit region. Note that the velocity profile changes from parabolic to straight.
Source: Rauwendaal (1986).

2.3.6.4.   Die flow instabilities

The two most common flow instabilities that affect extrudate products are shark skin and melt fracture.

Shark skin is the occurrence of a mat surface. It is generally formed in the channel or in the die exit. The cause of the occurrence of this problem is related with the change in velocity profile, also shown on Figure 24. The main parameters that influence on the appearance of this defect are the temperature and the extrusion speed. Decreasing the extrusion speed and increasing the temperature can reduce the problem. Very low temperature may also reduce shark skin defects (RAUWENDAAL, 1986).

Melt fracture is a more severe distortion of the extrudate and can appear in many different forms such as the examples shown in Figure 25. Melt fracture are not surface defect, like shark skin, but are associated with the whole body of the extrudate. The causes of melt fracture are not in agreement in the literature. But it was found to be reduced by controlling the temperature, extrusion speed or changing the die geometry (RAUWENDAAL, 1986).
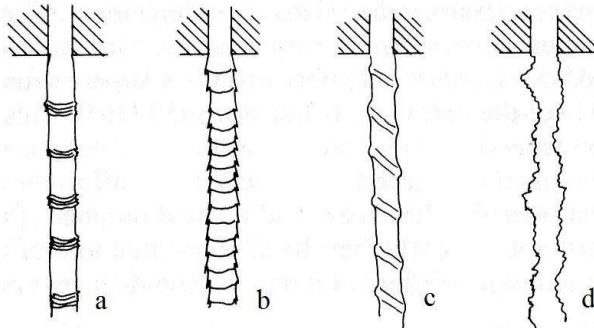
Figure 25 – Various forms of melt fracture: (a) regular ripple, (b) bamboo, (c) spiral and (d) random fracture. Source Rauwendaal (1986).

2.3.7. Debinding

Debinding is the removal of the binder. The binder should be extracted from the compact as a fluid – in the liquid or gas state – without distorting or contaminating the compact. This can be attained by six main different techniques that are divided into thermal debinding and solvent debinding (GERMAN, 1990).

Thermal debinding techniques are diffusion, permeation and wicking. Diffusion and permeating consist in heat the compact to a temperature high enough to cause the evaporation or degradation of the binder. Degradation can occur as decomposition, chain scission or depolymerization. If the compact has low porosity, diffusion is favorable, otherwise permeation occurs. Wicking is a technique in which the molten binder is extracted from the compact to the pores of a wicking substrate via capillary forces. In the wicking process the temperature should be enough to decrease sufficiently the viscosity of the binder (GERMAN, 1990).

Solvent debinding techniques are divided into extraction, high pressure and thermally assisted. These techniques consist in immersing the compact in a fluid that is able to dissolve some of the binders. The solvent induce binder flow out of the compact based on the chemical concentration gradient. The role of the solvent debinding is to create a pore structure, promoting channels through which vapor of the remaining binder can flow in the subsequent debinding by evaporation. Extraction is the simple immersion in a solvent. The high pressure technique utilizes a supercritical in which vapor and liquid are indistinguishable. The thermally assisted solvent debinding uses heat to increase the kinetics of the process, the solvent in this case may be in the vapor state. Solvents commonly used include ethanol, ethylene chloride, trichloroethylene, pentane, methylene chloride, Freon, acetone, hexane and heptane (GERMAN, 1990).

In practice two or more techniques mentioned above are combined to accelerate the debinding cycle. One key factor on debinding is to use multiple component binder system, allowing debinding to occur progressively in more than one step, so that after the removal of the first binder, another is still in a sufficient amount to hold the particles cohesively. Reactive atmospheres can reduce the binder removal time, but may also alter the particles composition (GERMAN, 1990).

Another relevant aspect is, when the binder is removed from the interstices of the particles, the compact becomes very fragile until it is sintered, though it must have sufficient strength to retain its shape (GERMAN, 1990). The compact after binder removal is often called brown part, in allusion with the green part after molding.

Usually wax and oils are removed by solvent debinding. On the other hand, the polymers with higher molecular weights are usually thermally removed. Oils and waxes should be over 30 vol.% of the binder, to form a sufficient interconnectivity to the surface and, later, to

provide an interconnected porous network that allows the polymers to evaporate in a subsequent thermal debinding step (GERMAN, 1990). The last polymers to be removed form the so called backbone, and are the binder components that will retain the shape of the compact until the earlier steps of sintering.

The debinding process is highly influenced by the permeability of the particles in the compact. The permeability in its turn is dependent on the packing density of the powder. Large particle size distributions lead to higher densities and decrease the permeability of the compact (GERMAN, 1990). The low permeability caused by dense packing powders difficult the debinding process.

During debinding, capillary forces act pulling particles together. If the compact is less dense than the critical loading, the liquid – molten binder or solvent – lubricates the surface of the particles that will rearrange migrating and sometimes agglomerating. As the binder is removed, the particles approach each other until contact each other, this, summed with possible residual binder, gives the compact strength. The removal of the residual binder can only occur by evaporation, *i.e.* thermal debinding, and must occur at the onset of sintering, since the compact cannot be handled once the binder is totally removed (GERMAN, 1990).

High debinding rates can be achieved with thin compact sections, large particles, high porosity, large pressure gradients and high temperatures (GERMAN, 1990).

2.3.7.1.   Debinding rate and atmosphere

High solid contents make debinding process slower due to reduced permeability of the binder through the denser particles packing. It is proved that shorter debinding times as well as better dimensional control is achieved using a solvent debinding step. Nevertheless all debinding routes end up with thermal evaporation step prior to sintering (GERMAN, 1990).

Basically thermal evaporating rates depend on three factors: binder molecular weight, atmosphere, and temperature. Evaporating rates decreases with increasing molecular weight of the binder. Atmosphere is also a very important factor that influences debinding rates and the selection between oxidizing, inert or reducing atmosphere

must be carefully made. Temperature obviously affects directly the binder removal, and the rate increases with increasing temperatures (GERMAN, 1990).

Oxidizing atmosphere makes debinding faster by oxidative degradation of the binder. The oxygen breaks the binder molecules apart increasing the evaporation rate. For most of metallic powders carry must be taken not to expose the material to oxygen at high temperatures, which would alter the surface chemistry of the particles, making sintering difficult (GERMAN, 1990).

Inert or reducing atmosphere retards the evaporation of the binder as can be seen in Figure 26. The plain binder and a binder mixed with powder shows a different evaporating kinetics as can also be seen in Figure 26.
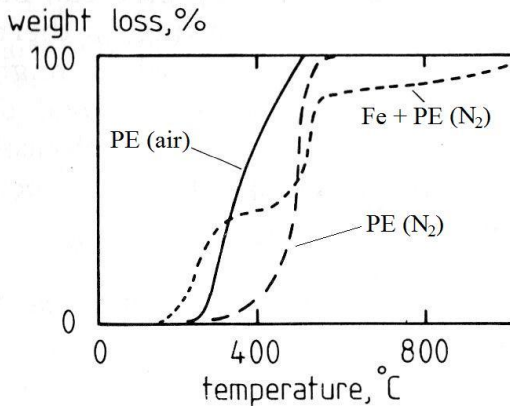
Figure 26 – Cumulative binder weight loss versus temperature for plain polyethylene in Air and N_2 atmosphere; and polyethylene mixed with iron powder in N_2 atmosphere.
Source: German (1990).

Commonly used atmospheres for thermal debinding are air, hydrogen, nitrogen, argon, methane and mixtures such as nitrogen-hydrogen, hydrogen-argon, and nitrogen-hydrogen-water. Vacuum is also used, but is best performed in the presence of a partial pressure atmosphere (GERMAN, 1990).

A problem closely related with atmosphere is residual carbon in the compact. The control of residual carbon is attained through selection of the debinding atmosphere, atmosphere flow rate. Heating rate has

also influence on the formation of residual carbon, however its role is not so clear and residual carbon can form either at low or high heating rates. There are evidences that show that, if the binder is not fully removed until debinding temperature reaches 450 °C, residual carbon may occur. As carbon control is not so simple, usually residual carbon is removed on the sintering step at higher temperatures (GERMAN, 1990).

2.3.7.2.   Debinding defects

The most common defect is the compact deformation by viscous flow, caused by gravity and compact weight. Powder can flow under relative low stresses, leading to distortion during debinding as the binder, which previously retained the compact shape by bonding between the particles, is removed from the compact. Deformation is more likely to happen for larger particle sizes, low solid contents, and higher particle sphericity (GERMAN, 1990).

Blisters, craters and vapor blowholes are other common problems. Vapor bubbles can nucleate during thermal debinding, if permeation or diffusion of vapor from the bubble to the surface does not occur, the pressure increases and displacement of particles may happen, leading to formation of such defects. Vapor diffusivity can decrease for higher packing density, which is influenced by particle size distribution, thicker sections, and larger particles. Blister, craters and blowholes are also particularly common when binder constituents are too volatile or if the heating rate is too fast. Entrapped air can also be a cause (GERMAN, 1990).

Single component binder systems offer higher probability for the appearance of debinding defects, due to difficult extraction (GERMAN, 1990).

2.3.8.   Sintering

Sintering is a heating process that causes particles to bond together and develops the desired microstructure and properties (GERMAN, 2005; GERMAN, 1990; REED, 1995). The term sintering is often erroneously associated with shrinkage and densification.

Although this happens in most of the cases, for some materials and certain applications, *e.g.* porous materials, the products may actually be less dense after sintering and experience swelling instead of shrinkage (REED, 1995).

Sintering triggers at one-half to two-thirds of the absolute melting temperature of the material. This temperature is sufficient to cause atomic diffusion for solid-state sintering (REED, 1995; GERMAN, 2005).

Microscopically, the first effects of sintering start to become evident in the formation of necks on the contact points between adjacent particles (GERMAN, 2005; GERMAN, 1990). Figure 27 show the necks grown in the contact of nickel particles sintered at 1200 °C for one hour.
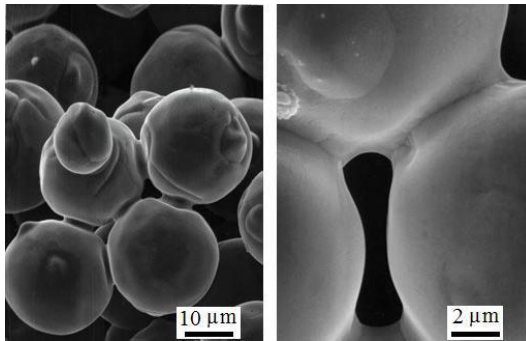
Figure 27 – Scanning electron image of neck formed on nickel particles sintered at 1200 °C for 60 min in vacuum.
Source: Plastics Today (2010).

Sintering is a temperature-dependent mechanism, whose driving force is the reduction of the total Gibb's free energy ΔG_T, which is the sum of change in the free energy associated with volume ΔG_V, boundaries ΔG_B, and surface area ΔG_S of grains, according to Equation 15 (REED, 1995).

Equation 15 $$\Delta G_T = \Delta G_V + \Delta G_B + \Delta G_S$$

The major driving force component in sintering is associated with the free surface energy, which depends directly with surface area ΔA_S, according to Equation 16 (REED, 1995).

Equation 16
$$\Delta G_S = \gamma_S \Delta A_S$$

The reduction in free surface energy is only possible with atomic mobility. For atoms to move, they need to break the bond with neighbor atoms, and for that a minimum energy should be reached. The amount of atoms that have sufficient energy to move increases with temperature exponentially, thus sintering is faster for higher temperatures (GERMAN, 2005).

Sintering is also faster for smaller particles, because of their higher surface area. (GERMAN, 1990; GERMAN, 2005).

2.3.8.1.   Solid-state sintering stages

Sintering evolves through three mains stages named initial, intermediate and final. Figure 28 shows schematically the evolution of loose spherical powder during sintering through the three stages.

The initial stage of sintering is characterized by the formation and growth of several necks. In this stage pores are irregular and angular in shape. This process results on compact shrinkage that is about 3% on the initial stage (GERMAN, 1990; GERMAN, 2005).

Most of the shrinkage and densification occur during the intermediate stage and density reaches 92% of the theoretical value. It is during the intermediate stage that most of the properties development related with the sintering process occur. Pores develop a smoother and rounder or cylindrical shape and their sizes reduce gradually, but an interconnected pore network is present until the end of this stage (GERMAN, 1990; GERMAN, 2005).

loose powder   initial stage

intermediate stage   final stage
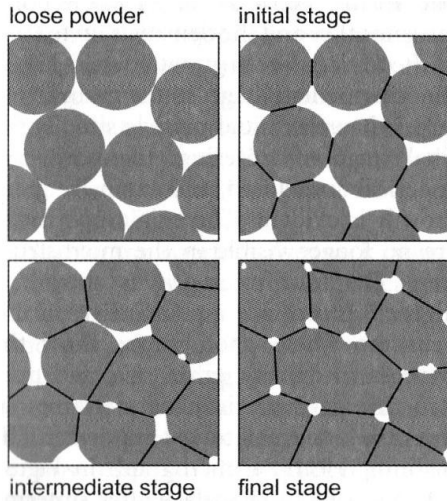
Figure 28 – Conceptual evolution of spherical
particles through the three stages of sintering.
Source: German (2005).

The final stage is denoted by closed pores with spherical or lens
shape and an extensive grain growth occurs. The original particles have
lost their individuality and are no longer distinguishable. It is
characterized by a slow kinetics, since most of the available energy from
the excess surface free energy has been consumed during the previous
stages. The porous are located on the grain boundaries intersections or
inside the grain, isolated from each other (GERMAN, 1990; GERMAN,
2005).

2.3.8.2.   Sintering parameters

Sintering is a process inherently dependent on (GERMAN,
1990):

    i.   Particle size;
   ii.   Initial powder packing uniformity and density;
  iii.   Temperature;
  iv.   Time;

      v.   Heating rate;
     vi.   Atmosphere.

The two first parameters are related with the material and previous process steps, while the other four are the parameters related with the sintering process itself. As mentioned in the previous section, sintering is faster for small particle sizes, as the reduction of the surface free energy is the driving force of the process (GERMAN, 1990).

Powder packing uniformity and a high green density can improve sintering, because of the higher particle contact coordination and lower initial porosity. This leads to a faster sintering and lower shrinkage (GERMAN, 1990).

High heating rates may cause distortion or cracks due to allotropic transformations or non-uniform heating in the case of thick sections. A fast heating may also cause retention of residual carbon (GERMAN, 2005). On the other hand, a too slow heating rate may cause grain growth due to long exposures time at high temperatures (COOVATTANACHAI, et al., 2010).

Increased sintering time results in higher densities but bigger grain sizes (GERMAN, 1990), whereas high temperatures results in greater shrinkage and higher density, but also grain growth and pore coarsening (GERMAN, 1990).

Atmosphere plays an important role during sintering. Common sintering atmospheres are: hydrogen, dissociated ammonia, water vapor, argon, helium, nitrogen, methane, propane, and mixtures of these gases. Vacuum is also often used, with or without partial pressure control. There are three mains aspects to be concerned with the atmosphere during sintering (REED, 1995; GERMAN, 1990; GERMAN, 2005):

      i.   Non-soluble gas proceeding from the atmosphere can be trapped into closed pores refraining pore shrinkage and density improvement;

     ii.   The partial pressure of the gases contained in the atmosphere may control the vaporization of elements or the stoichiometry of compounds in the particles;

    iii.   Reactive gases from the atmosphere may reduce or oxidize the particles elements or compounds;

According to the reactivity of the atmosphere, they can be classified as (GERMAN, 2005):

  i.   *Oxidizing* – carbon dioxide, water or oxygen;
  ii. *Neutral* – argon, helium or vacuum;
  iii. *Reducing* – hydrogen or carbon monoxide;
  iv. *Hydriding* – hydrogen, ammonia;
  v.   *Dehydriding* – vacuum or argon;
  vi. *Nitriding* – nitrogen or ammonia;
  vii. *Carburizing* – methane or propane;
  viii. *Decarburizing* – carbon dioxide, or oxygen.

Oxide ceramics are usually sintered in air, but most of the high-performance materials require protective atmospheres, including even oxides. Metallic powders usually require a protective atmosphere – inert or reducing – to avoid oxidation (GERMAN, 1990).

3. EXPERIMENTAL

This chapter describes the experimental methods used in this work and was divided in three sections. The first one shows all the materials utilized in the work. The second section describes the experimental procedure and the approach used to achieve the objectives of this work. Finally, the instruments and equipment used are specified and briefly described.

3.1. MATERIALS

The materials used are categorized into three groups: *powders*, that include the metallic and ceramic powders; *fibers*, the alumina fibers; and *binders and solvents*, which are the waxes, surfactants and polymers used as binders, and solvents used for solvent debinding.

3.1.1. Powders

Table 6 shows the composition, nominal particle size distribution, tap density, commercial name, and supplier of the powders used. The nomenclature used in the work is also provided.

Table 6 – Basic information provided by the suppliers of the used powders.

Used nomenclature	Type	Composition (%)	Nominal particle size (μm)	Tap density (g/cm^3)	Commercial name	Supplier
Al$_2$O$_3$/ Alumina	Alumina	α-Al$_2$O$_3$ > 99.9	d90 = 3.2 d50 = 2.1 d10 = 1.55	1.3	Sumi-corundum™ AA-2	Sumitomo Chemical Co., Ltd.
IN718 * (1st batch)	Nickel based superalloy	See Table 7	d90 = 9.9 d50 = 5.6 d10 = 3.1	5.1	IN718	Sandvik Osprey Ltd.
IN718 (2nd batch)	Nickel based superalloy	See Table 7	d90 = 9.9 d50 = 6.2 d10 = 3.9	4.8	IN718	Sandvik Osprey Ltd.

* – Used only for behavior comparison during preliminary tests of mixing, warm pressing and debinding.

Table 7 shows the more detailed chemical composition of the nickel based superalloy IN718.

Table 7 – Chemical composition of the nickel based superalloy IN718, after the supplier. Elements with percentage above 1.0% are marked in bold.

Element	Chemical composition (%)	
	IN718 (1st batch)	IN718 (2nd batch)
Ni	**53.0**	**52.9**
Fe	**> 18.7**	**> 18.8**
Cr	**18.4**	**18.5**
Nb	**5.0**	**5.0**
Mo	**3.2**	**3.1**
Ti	0.92	0.88
Al	0.50	0.47
Si	0.100	0.14
C	0.072	0.060
Cu	0.020	0.018
Mn	0.020	0.063
B	0.003	0.003

3.1.2. Fibers

The fibers chosen for the present work were Nextel™ 610 alumina short fibers, 30 mm long, provided by 3M Co. Some characteristics and properties of these fibers, after the manufacturer, are:

     i.   *Sizing color* – off-white;
    ii.   *Chemical composition* – > 99% Al_2O_3;
   iii.   *Melting point* – 2000 °C;
   iv.   *Filament diameter* – 10 – 12 µm;
    v.   *Crystal size* – < 500 nm;
   vi.   *Crystal phase* – α-Al_2O_3;
  vii.   *Density* – 3.9 g/cm^3;
 viii.   *Surface area* – < 0.2 m^2/g;
   ix.   *Filament tensile strength* – 3.1 GPa;
    x.   *Filament tensile modulus* – 380 GPa;

xi. *Coefficient of thermal expansion (100-1100 °C) – 8.0 x 10^{-6} °C^{-1};*

3.1.3. Binders and solvent

The properties and supplier's information of the binders and surfactant are shown in Table 8.

Table 8 – Properties and supplier's information of binders and surfactant used.

Used nomenclature	Common name	Additive Type*	MFI (g/10min)	Density (g/cm³)	T_m (°C)	Commercial name	Supplier
LDPE70	Low density polyethylene	Binder	70	0.919	108	Lacqtene® 1700MN18C	Elf Atochem S.A.
LDPE02	Low density polyethylene	Binder	02	0.930	115	Lacqtene® 1020FE30	Elf Atochem S.A.
PW	Paraffin wax	Binder / Plasticizer	N/A	N/A	58 - 60	Paraffin wax 76231 Fluka	Sigma-Aldrich Co.
SA	Stearic acid	Surfactant / Dispersant / Plasticizer	N/A	0.845	67-69	Stearic acid 93661 Fluka	Sigma-Aldrich Co.

* The additives were classified according to the definitions of their functions (REED, 1995), this information was not provided by the suppliers.

The solvent used for solvent debinding was commercial ethanol 95%.

3.2. METHODS

3.2.1. Feedstock development

Before the extrusion of the tubes, attention was given to the feedstock behavior during mixing, shaping and, especially, debinding. To develop the feedstock, no fibers were added in the mixture, so that

only the powders, binders and additives would influence the rheological behavior and debinding kinetics.

Two main parameters of the feedstock were investigated and defined. The first was the filling level, *i.e.* solid volume content. The second parameter was the binder system, *i.e.* the types and proportions of binders and additives. Hereafter binder system must be considered a mixture of all binders and additives, regardless if a component of the mixture has the binder function or not. The idea was to develop a feedstock that could be used for both alumina and IN718 powders. As a starting point, preliminary tests were performed performed with a feedstock composed of LDPE70 and 54 vol.% of solids.

Mixing was always carried out in the kneader adding first the binder with highest melting point and subsequently the binders with lower melting point. After all the binders were molten, the powder was added. The chamber effective volume was 69 cm^3, however only 70 % of the volume was used, *i.e.* 48.3 cm^3. The procedure was in agreement with the literature (GERMAN, 1990; CHENG, et al., 2001). Mixing occurred in 2 steps. First, a pre-mixing at 180 °C for 30 minutes, then a final mixing at 152 °C for 40 minutes. The rotation speed was 10 RPM in both steps. The first step was responsible for mixing the binder components and adsorbing binder to powder and breakage of fibers. The second step, at lower temperature and consequently higher shear stress, was responsible for breakage of agglomerates and fibers.

The prepared feedstock was then granulated in a capillary rheometer at 140 °C through a cylindrical die with diameter of 1.0 mm and length of 28 mm. Granulation was performed at three different piston speeds, with the corresponding shear rate and granulation speed shown in Table 9. Granulation speed means the velocity at which the extrudate comes out o the die[5]. During granulation, cylinder pressure and piston force were measured.

Table 9 – Granulation parameters.

Piston speed (mm/min)	Granulation speed (mm/min)	Shear rate (s^{-1})
1.04	600	80
1.30	750	100
1.56	900	120

---

[5] Granulation speed was calculated with a simple geometric relation between the area of the cylinder and the area of the die channel cross sections. By knowing the speed of the piston inside the cylinder was possible to calculate the speed of the extrudate on the die channel.

During feedstock development, no tubes were extruded. Instead, the feedstock granules were warm pressed into disc-shaped samples of 28 mm of diameter. The amount of granules pressed was calculated to produce discs with thickness of 0.8 mm, however, due to feedstocks loss through the gaps between die and punchers, the thickness was slightly lower than that. The samples were pressed under 10 kN (corresponding pressure of 163.9 bar) at various temperatures, weighted and their densities were measured by the Archimedes method.

Debinding of the disc samples was made in a tube furnace with controlled atmosphere. The debinding program was defined according to the results of thermogravimetric analysis (TGA) used for the characterization of the binders. The following debinding atmospheres were used under atmospheric pressure:

i. *Reducing* – forming gas (N_2 + 8%H_2) with a flow rate of 0.2 *l*/min;
ii. *Oxidizing* – air without forced flow;

Figure 29 schematically shows the experimental procedure followed in the feedstock development.
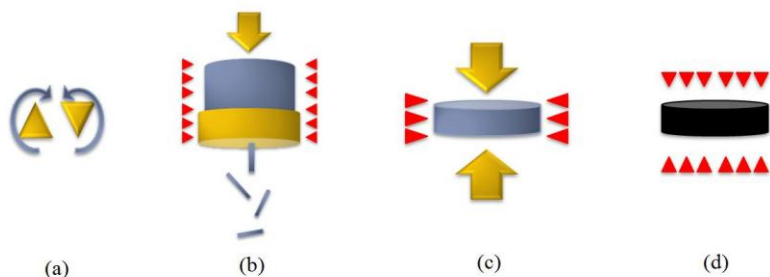
Figure 29 – Schematic diagram of the procedure used in the feedstock development. (a) Mixing, (b) granulation, (c) warm-pressing and (d) debinding.

3.2.1.1. Filling level definition and maximum filling level determination

To define the solid volume content and determine the maximum filling level several feedstocks, with a simple binder system, composed of plain LDPE, were prepared. The solids content varied between 54 and 62 vol.%, that is roughly the same range usually used in PIM (GERMAN, 1990). Mixing was carried out in the kneader at 152 °C.

To define the maximum filling level, in which viscosity approaches infinite, and so as the mixing torque, a relationship between the solids-binder ratio and the inverse of mixing torque was used. This method was developed in the group of Clemens and is going to be shown in a later section. For this method, the torque data of unfilled LDPE, *i.e.* no powder addition, was also included. To validate the results and the method, data was compared with different viscosity models.

The following characteristics were considered during the definition of the filling level:

i. Mixing torque;
ii. Maximum filling level;
iii. Debinding behavior.

Mixing torque should not be too high, close to the limit of the kneader, because although the addition of paraffin wax in the binder system during binder system definition would reduce the torque, the fiber addition for tube extrusion would, on the contrary, increase it. What effect would be predominant was difficult to estimate, so that a safety margin should be given. The defined filling level should also be, obviously, below the maximum filling level (GERMAN, 1990).

All samples were warm pressed at 140 °C under 10 kN (corresponding pressure of 163.9 bar).

The debinding behavior was analyzed considering the presence of defects in the samples after the debinding cycle, such as deformation, edge rounding and blisters.

3.2.1.2. Binder system definition

After defining the filling level, the binder system had to be developed. A three component binder system composed by low density polyethylene (LDPE), paraffin wax (PW) and stearic acid (SA) was used. A multi-component binder system would, according to the literature, permit faster debinding less prone to the formation of debinding defects.

As surfactant, SA was used in a small amount, fixed in 5.0 vol.% of the total amount of binder, as used in many others similar PIM binder systems (GERMAN, 1990). So what had to be investigated was the volume fractions of LDPE and PW.

Several amounts of PW content were investigated varying from zero to 95 vol.%. SA was used in a fix value of 5 vol.%. The balance was LDPE.

The warm pressing temperature was empirically determined in a way that perfect discs were produced. With too low temperatures, the feedstock could not fill the mold properly, while with too high temperatures an excess of flash was produced and material was lost through the gap of the mould. The temperature varied from 95 to 140 °C. Pressing was performed under 10 kN (corresponding pressure of 163.9 bar).

The amount of PW was defined based on the debinding behavior, *i.e.* absence of deformation, edge rounding and blisters.

3.2.2. Tube extrusion

After feedstock development, 30 vol.% of Nextel™ 610 fibers were incorporated into the solids content of feedstock, being the other 70 vol.% alumina or IN718 powder. This amount was also fixed according to previous studies for other CMCs and MMCs (CHAWLA, 2003; CHAWLA, et al., 2006; SURESH, et al., 1993; MILEIKO, 1997). Figure 30 shows schematically the composition of the feedstock after binder system definition and the introduction of fibers.
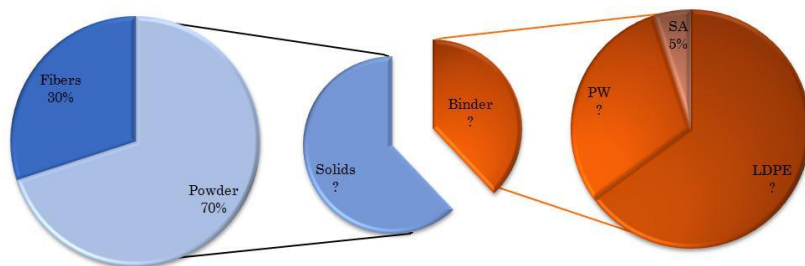
Figure 30 – Schematic graphic of feedstock composition. Question marks denote the amount to be defined during feedstock development.

Tube extrusion was also carried out in the capillary rheometer adapted with special tube production dies. Three different tube geometries were produced as follows:

    i.   10.0 mm of external diameter and 1.0 mm of thickness;
    ii.   10.0 mm of external diameter and 0.6 mm of thickness;
    iii.   4.5 mm of external diameter and 1.0 mm of thickness.

Figure 31 illustrates the three different tube geometries.
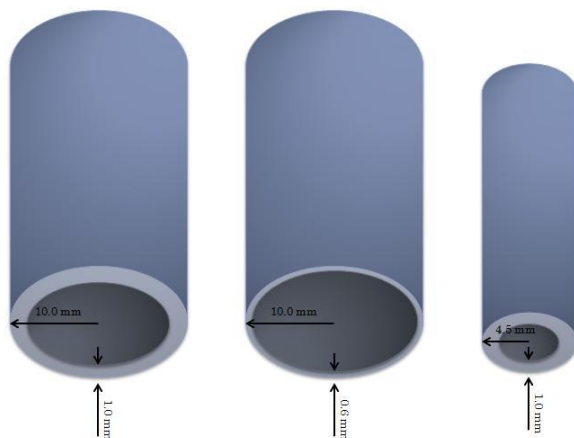
Figure 31 – Sketch of the three different geometries of the extruded tubes.

The adapted capillary rheometer permitted the control of three process parameters:

i.   *Cylinder temperature* – ranging from temperatures under and above the LDPE melting temperature (108 °C);
ii. *Die temperature* – also ranging from under and above LDPE melting temperature;
iii. *Extrusion piston speed* – ranging from 0.39 to 2.00 mm/min.

The extrusion parameters were controlled until a perfect extrudate, without any visual defects, such as warping and extrudate fracture. After a perfect extrudate was produced, samples were analyzed by scanning electron microscopy (SEM) in order to check the fiber alignment.

3.2.3.   Tubes debinding

Tubes samples were cut, weighted and had their length measured prior to debinding. Priority was given to a simple program of thermal debinding. Solvent debinding would have been used only in the case of failure of the fully thermal debinding, *i.e.* appearance of debinding defects, such as deformation and blisters.

Thermal debinding of the extruded tubes was performed according to TGA analysis of the feedstock constituents.

3.2.3.1.   Solvent debinding

Solvent debinding was used to extract PW and SA before the thermal extraction of the backbone (LDPE). The samples were held in an ethanol bath at 60 °C for 5 hours.

After solvent debinding, the samples were weighted to check the percentage of binder removed. Then a normal thermal debinding cycle was used to extract the LDPE.

3.2.4. Tubes sintering

The tubes were sintered in the same furnace used for thermal debinding. All the tubes were sintered at 1300 °C for 60 minutes, with a heating rate of 5.0 °C/min. The temperature was chosen to provide a certain degree of sintering without, though, damaging the Nextel™ fibers that starts to degrade above 1300 °C (LEE, et al., 2003). For the same reason, a short period of exposure to high temperature, 60 minutes, was stipulated. At this temperature and time a porous structure, similar to those produced by WHIPOX™ process, was expected to be produced (CHAWLA, 2003). The following sintering atmospheres were used under atmospheric pressure:

    i.   *Reducing* – forming gas (N_2 + 8% H_2) with a flow rate of 0.2 l/min;

    ii.   *Oxidizing* – air (only for CMCs) without forced flow;

After sintering samples were weighted and, afterwards, broken transversally and parallelly to extrusion direction for SEM analysis. The samples were broken instead of cut in order to expose the fibers on the surface, making it easier to visualize their alignment.

3.3. INSTRUMENTS

3.3.1. Processing instruments

For the feedstock production and characterization a torque rheometer (kneader) Thermo Scientific model Haake PolyLab OS RheoDrive 4 was used. The chamber volume without the rotors was 120 cm^3. The rotors used were Roller-Rotors R600 type, shown in Figure 32. With these rotors the chamber effective volume was reduced to 69 cm^3. The maximum speed and maximum torque of this equipment was 250 RPM and 160 Nm, respectively.

Figure 32 – Rotors used for mixing in the kneader. Rotors type: Roller-Rotors R600.

The disc-shaped samples were warm-pressed in a manual press from Paul-Otto Weber GmbH, model not specified, with a maximum force of 200 kN. A cylindrical die with diameter of 28.0 mm was heated up to pressing temperature by means of a heating band with controlled temperature. Figure 33 shows the die and punches used and Figure 34 shows the setup made for warm pressing, composed by press, die, heating band and temperature controller.
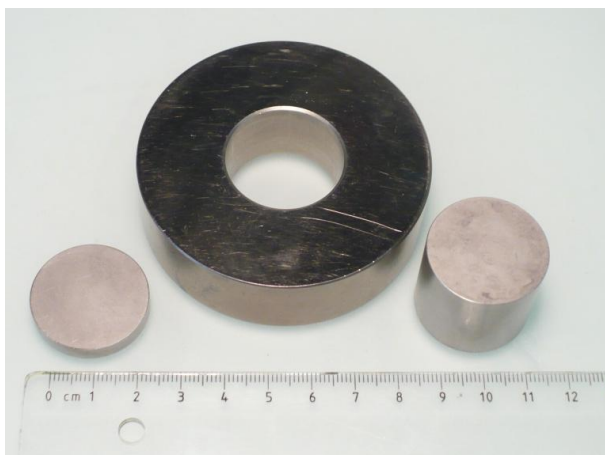
Figure 33 – Picture of the die, upper punch (bigger) and lower punch (smaller) used for warm-pressing the disc-shaped samples.
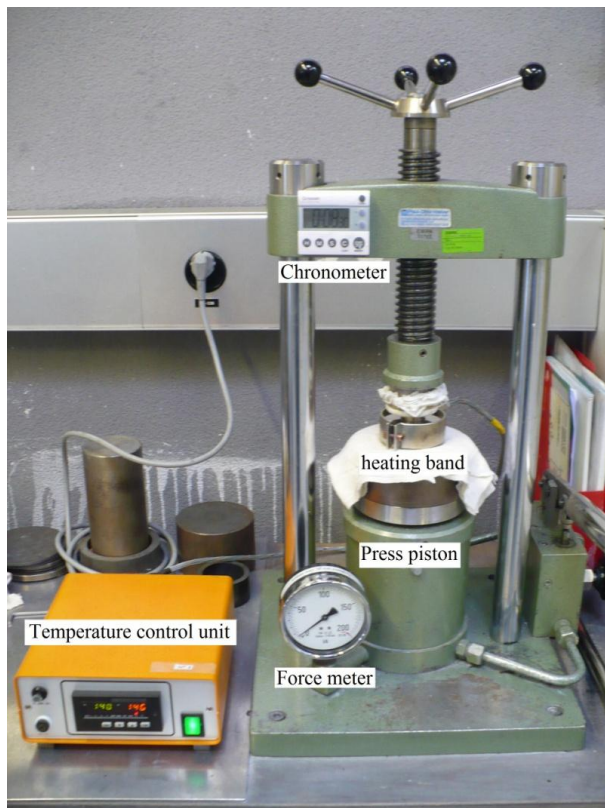
Figure 34 – Warm-pressing setup, showing the press and its piston, the heating band around the die, the force meter, chronometer, and temperature control unit.

The feedstock granulation and tube extrusion have been performed in a capillary rheometer from Bohlin Instruments Rosand, model RH7 Flowmaster, shown in Figure 35. For granulation a die with length of 28.0 mm, diameter of 1.0 mm and entrance angle of 0° was used, see Figure 36. In the case of tube extrusion dies with an entrance angle of 45°, with 10.0 and 4.5 mm of diameter were used. Three different pin diameters were used, 2.5 mm, 8.0 mm and 8.8 mm in combination with the two dies to produce the three different tubes geometries. Table 10 shows the combination of dies and pins, with the respective produced tubes geometries. Figure 37 shows a sketch of the tubes production dies.

Table 10 – Dies and pins basic geometries used for tube production and the respective produced tube geometries.

Die diameter (mm)	Die entrance angle (°)	Pin diameter (mm)	Tube external diameter (mm)	Tube thickness (mm)
10.0	45	8.8	10.0	0.6
10.0	45	8.0	10.0	1.0
4.5	45	2.5	10.0	1.0

Figure 35 – Capillary rheometer used to granulate the feedstock and to extrude the tubes.
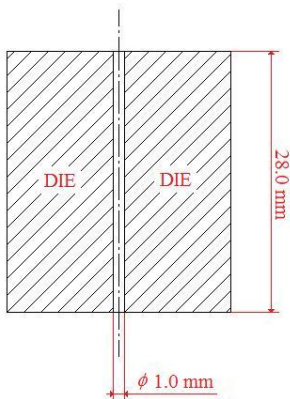
Figure 36 – Sketch of the die used for feedstock granulation.
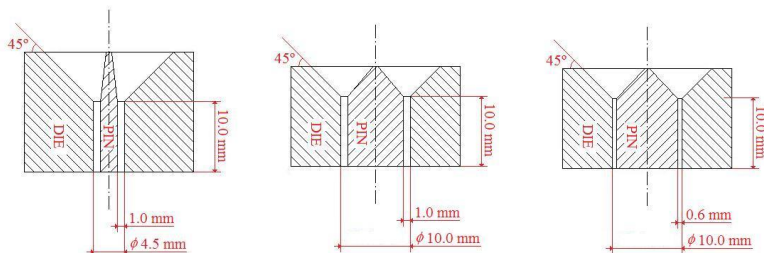
Figure 37 – Sketch of the dies used for tube extrusion, showing the die diameter, the extrudate thickness and the die entrance angle.

Figure 38 shows the setup made for solvent debinding. In this setup the solvent temperature could be controlled with a thermocouple inside the chamber in the bath. The chamber was held in atmospheric pressure and a condenser was positioned above the chamber, where most of solvent vapor was recovered.
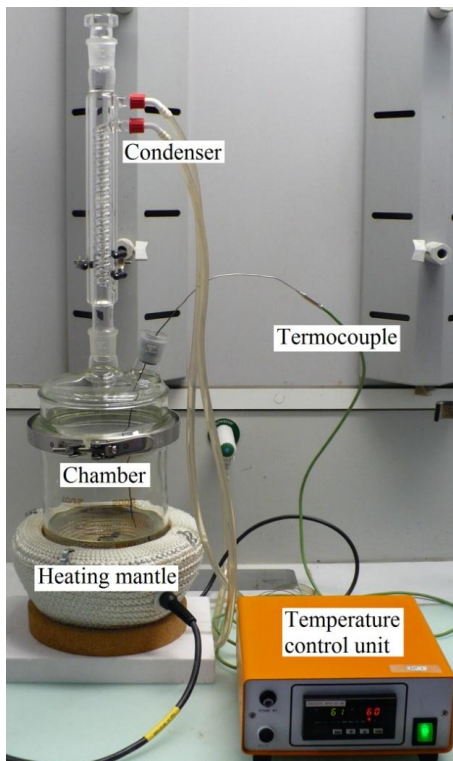
Figure 38 – Solvent debinding setup.

Thermal debinding and sintering was carried out in a tube furnace from Carbolite GmbH model Rohrofen HST 15/-/610.

3.3.2.   Characterization instruments

The following techniques and their respective instruments were used for the characterization of powders, fibers, binders, warm-pressed samples and tubes:

i. *SEM* – Tescan model Vega Plus TS 5136 MM, at various voltage and sport sizes, a work distance of 10 mm using the secondary and backscattered electrons detectors;

ii. *Coating of SEM samples* – Sputter Coater Cressington model 108auto Au/Pl, using argon as sputtering gas, at 60 mA during 60 seconds;

iii. *Archimedes density* – Mettler Toledo model AG204 DeltaRange, using water as measurement media;

iv. *Helium pycnometry* – Micrometrics model AccuPyc® 1330;

v. *Particle size analysis* – Coulter model LS 230, using Fraunhofer diffraction and deionized water as measuring media;

vi. *BET surface area analysis* – Coulter model SA 3100, using the BET-5 measurement profile;

vii. *TGA/SDTA* – Mettler Toledo model TGA/SDTA851^e, under forming gas (N_2 + 8% H_2) and atmospheric air;

viii. *Mercury porosimetry* – Thermo Fisher Mercury Intrusion Porosimeter model Pascal 140/440, with a surface tension and a mercury contact angle set to 0.480 N/m and 140°, respectively;

ix. *X-ray diffractometry* – PANalytical Diffractometer model X'Pert PRO MPD, using Cu Kα radiation and an angular range from 5 to 80° (2θ).

4. RESULTS AND DISCUSSIONS

4.1. MATERIALS CHARACTERIZATION

The IN718 and alumina powders were characterized as received. Figure 39 and Figure 40 show the SEM image of the IN718 (2nd batch)[6] and alumina powders respectively.
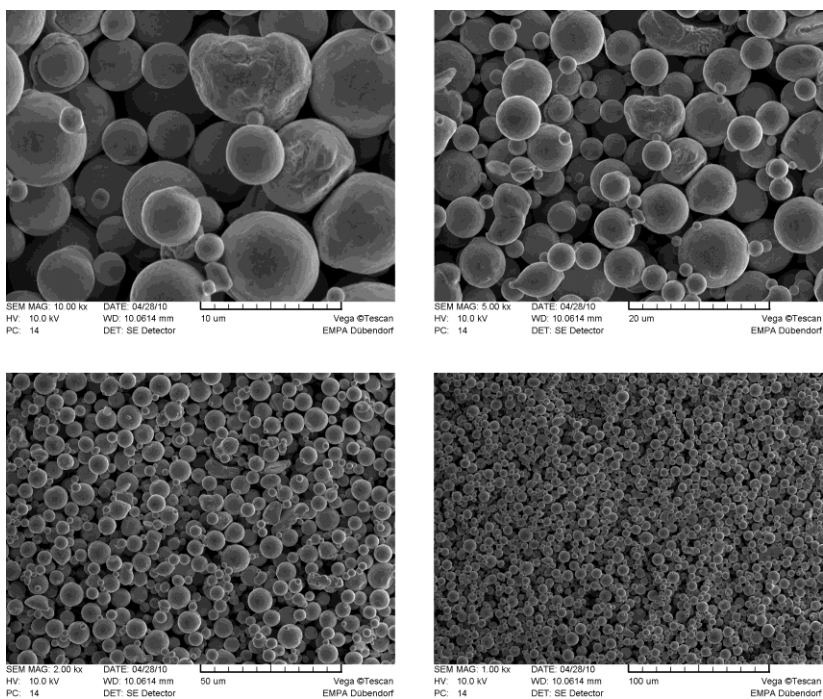
Figure 39 – SEM images of IN718 powder in four different magnifications, 10000, 5000, 2000 and 1000x.

From the images is possible to see differences in morphology, size and particle size distribution of the two different powders. Most of the atomized IN718 particles have an almost perfect spherical shape,

---

[6] As the morphological characteristics of the particles of the first and second batches were almost identical, in the present work SEM images of only one of them were shown.

despite some irregular, yet rounded, particles are also present. On the other hand the particles of the alumina powder are overall of polygonal shape. Another evident difference is the mean size of the particles, which is larger for the IN718 powder.
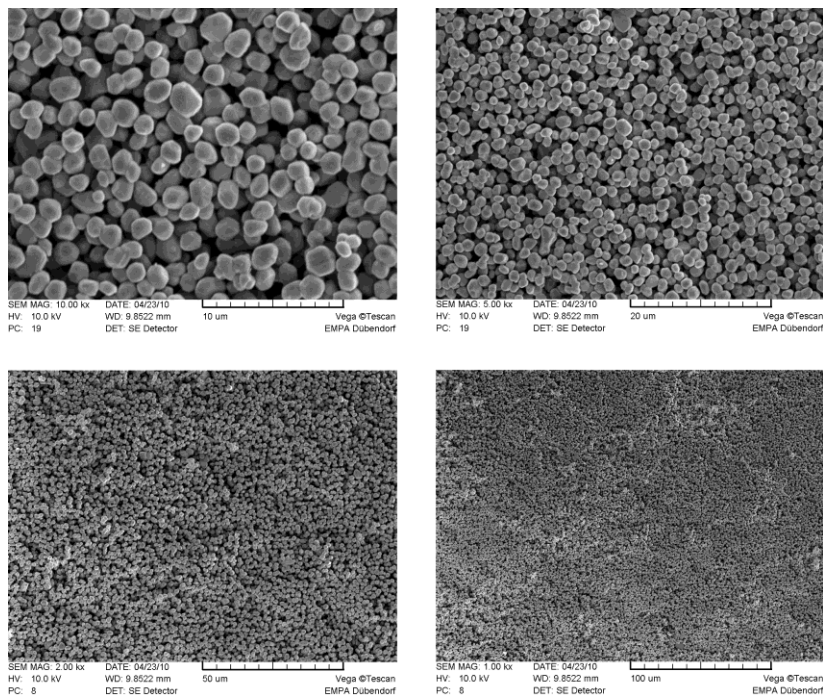
Figure 40 – SEM images of alumina powder in four different magnifications, 10000, 5000, 2000 and 1000x.

The particle size and PSD of the powders were measured by a laser light scattering particle size analyzer and the results can be seen in Figure 41 and Figure 42. Surprisingly a bimodal PSD was found for all the powders, being more evident on the alumina powder. The particles found in the submicrometric scale in the alumina powder might be an analysis error due to the method used (Fraunhofer diffraction), which is not the most adequate for ceramic particles. In the case of the metallic powder it is hard to say what is the reason for the detection of submicrometric particles. Helium pycnometry and BET analyses were also performed and the results are summarized in Table 11.
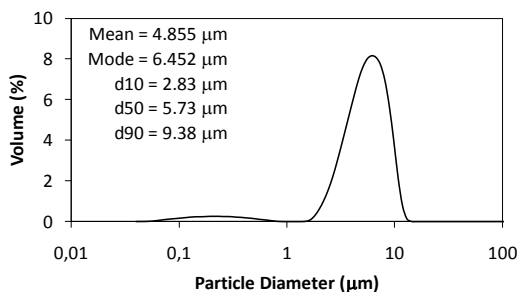
Figure 41 – PSD analysis of the IN718 powder from 2nd batch.
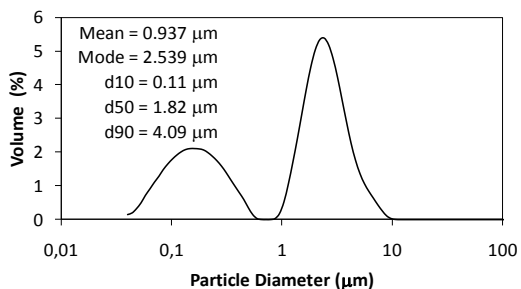
Figure 42 – PSD analysis of the alumina powder.

Table 11 – Results of helium pycnometry and BET analysis for the two different powders.

Powder	He Pycnometer Density (g/cm^3)	BET surface area (m^2/g)
IN718 (1st batch)	8.1924	0.229
IN718 (2nd batch)	8.1759	0.216
Alumina	4.0000	0.777

Figure 43 shows the SEM images of the Nextel™ 610 fibers. Note that the fibers have smooth surfaces but not perfectly cylinder-like shape, which cannot be clearly seen in these images.
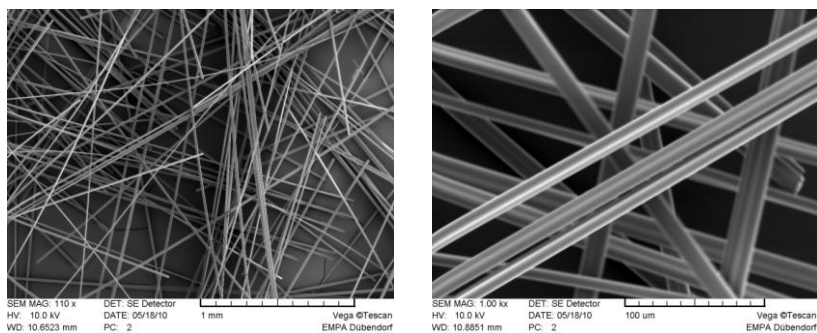
Figure 43 – SEM images of Nextel™ 610 alumina fibers. Magnification: 110 and 1000 x.

The temperature of degradation/evaporation of the binders was characterized by thermogravimetric analysis (TGA). Samples were analyzed in a forming gas atmosphere, from room temperature to 600 °C, with a heating rate of 5.0 °C/min. The results are shown in Figure 44 to Figure 47. As it can be seen, both LDPE's evaporate/degrade at more or less the same temperature range, with maximum mass loss rate at 459 °C for LDPE70 and 470 °C for LDPE02. The LDPE's show the higher extraction temperatures and are completely removed close to 490 °C. Paraffin wax and stearic acid show their maximum mass loss rate at 305 and 263 °C, respectively. Above 330 °C, nearly all paraffin wax is removed, whereas most of stearic acid is removed at 270 °C.
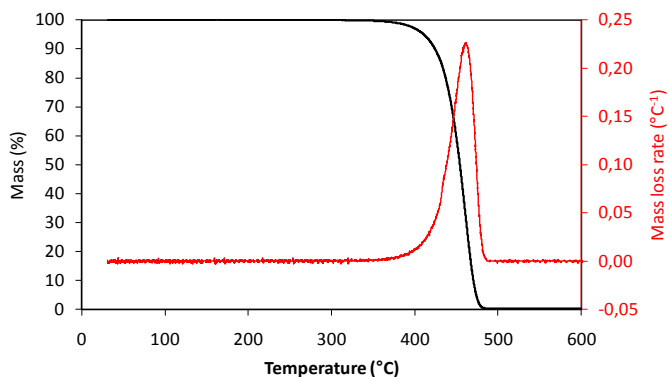
Figure 44 – Thermogravimetric analysis of LDPE70 in forming gas.
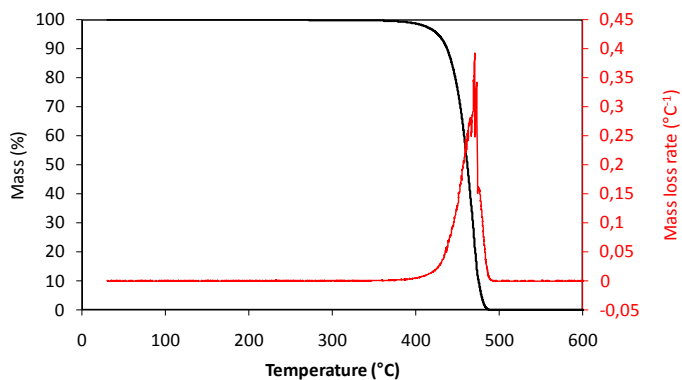
Figure 45 – Thermogravimetric analysis of LDPE02 in forming gas.
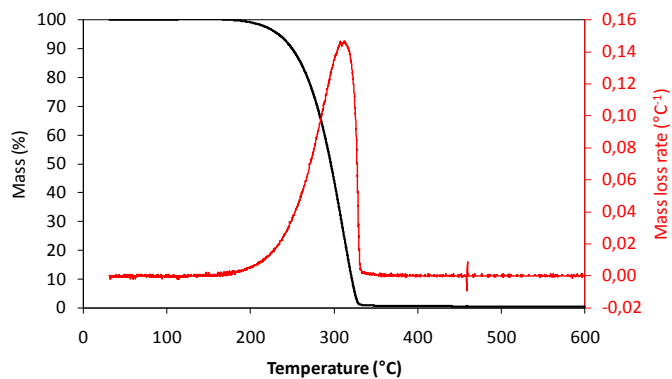
Figure 46 – Thermogravimetric analysis of PW in forming gas.

118
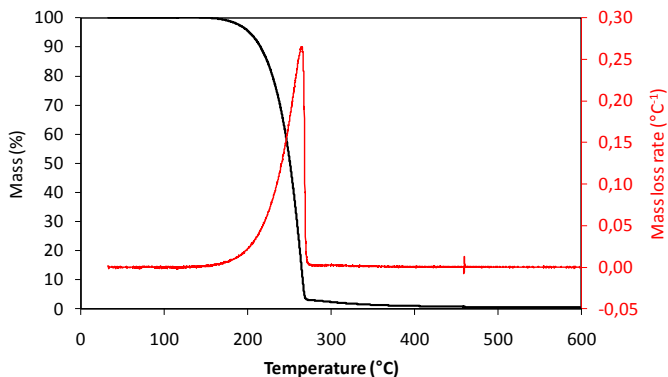
Figure 47 – Thermogravimetric analysis of SA in forming gas.

4.2. PRELIMINARY TESTS

4.2.1. Alumina and IN718 feedstocks with plain LDPE70

4.2.1.1. Mixing

The starting point of the study was a feedstock with 54 vol.% of solids a LDPE70 binder system. Figure 48 to Figure 51 show the plot of the torque and temperature versus time during pre-mixing and mixing of the nickel-based and alumina powders. The conditions of pre-mixing and mixing were the same for both powders, as described in the previous section.

As it can be seen in Figure 48 to Figure 51, the mixing of both powders followed a typical behavior (GERMAN, 1990), showing first an increase of torque, with a decrease of temperature as the materials were introduced in the mixing chamber. As the temperature increased, either by the heating elements or by interparticle friction, the torque decreased until a certain homogeneity level in which both torque and temperature stabilized, which denotes good mixing. It can be also

noticed that the torque of the pre-mixing was lower than the torque during mixing, for both alumina and IN718, since the temperature during pre-mixing was higher than during mixing.
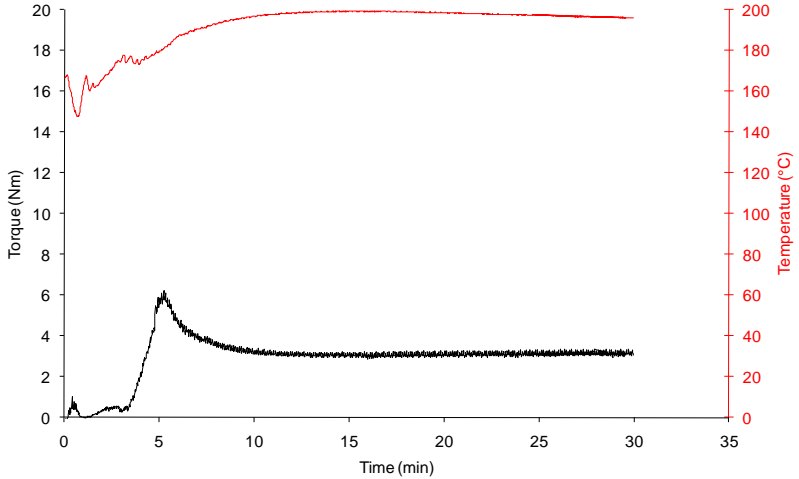
Figure 48 – Plot of pre-mixing torque and temperature versus mixing time of 54 vol.% of alumina powder with a plain LDPE70 binder system.
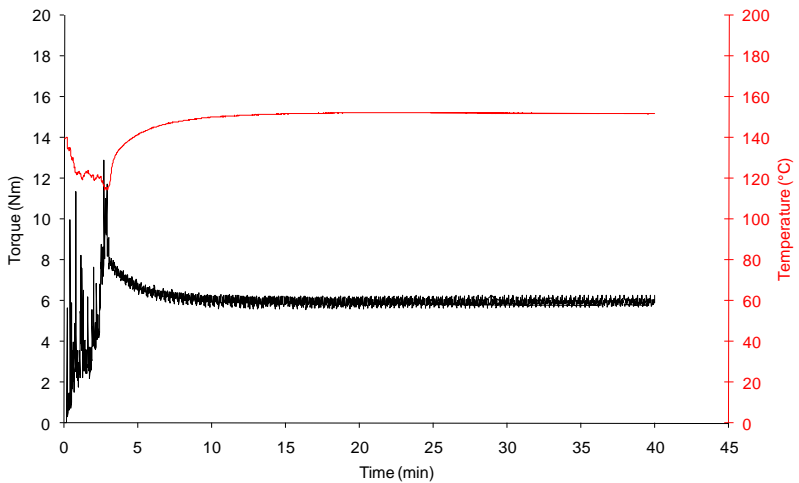
Figure 49 – Plot of mixing torque and temperature versus mixing time of 54 vol.% of alumina powder with a plain LDPE70 binder system.
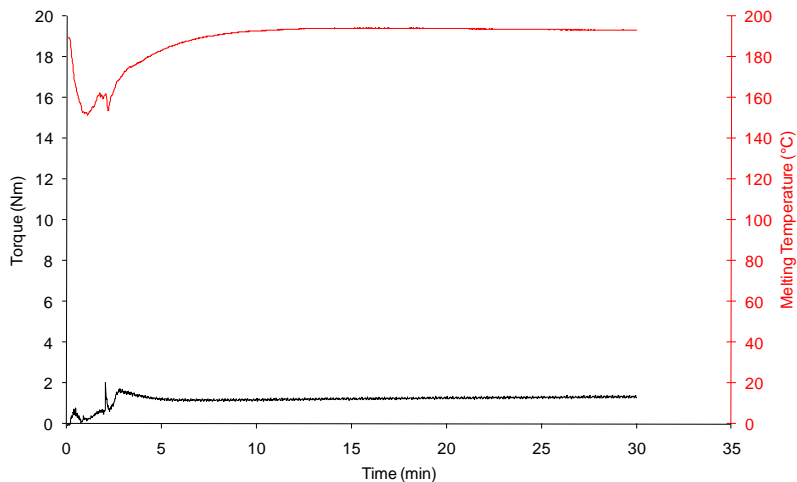
Figure 50 – Plot of pre-mixing torque and temperature versus mixing time of 54 vol.% of IN718 powder with a plain LDPE70 binder system.
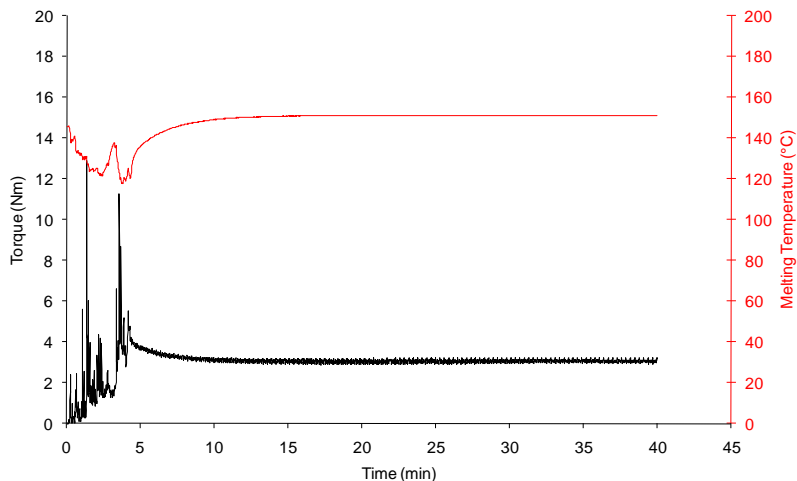
Figure 51 – Plot of mixing torque and temperature versus mixing time of 54 vol.% of IN718 powder with a plain LDPE70 binder system.

In order to have a better overview and to compare the behavior of the different powders, Figure 52 shows the plot of torque versus time of the final mixing of IN718 and alumina powders. Although the behavior

of both materials was quite similar, in terms of torque curve shape, the difference in average torque is very clear, 5.94 Nm for alumina and 3.07 Nm for IN718. The higher torque for the alumina powder, almost twice higher, might be associated with the difference in powder characteristics, mainly particle size, PSD and powder shape (GERMAN, 1990; SHENOY, 1999). The particle shape in this case is of great importance, since the polygonal shape of alumina particles offers a much higher inter-particle friction than the round IN718 particles (GERMAN, 1990). Another factor may be related with surface physics, *e.g.* wetting, which induces a different interaction powder-binder, causing lower or higher frictions.
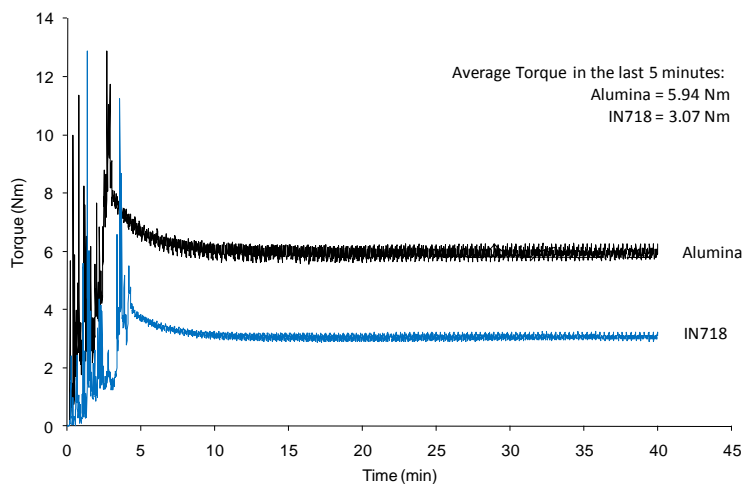
Figure 52 – Plot of mixing torque versus time of alumina and IN718 feedstocks with 54 vol.% of solids and a plain LDPE70 binder system. The mixing temperature at stable torque stage was 152 °C.

4.2.1.2. Granulation

The feedstocks have also shown a similar relation during granulation. Figure 53 and Figure 54 show the cylinder pressure and the piston force, respectively, during granulation of IN718 and alumina feedstocks. Each plateau corresponds to the stabilization of pressure or force at the three different shear rates and the corresponding granulation speeds. Table 12 shows the average pressure and piston force during granulation at the three different granulation speeds and shear rates.
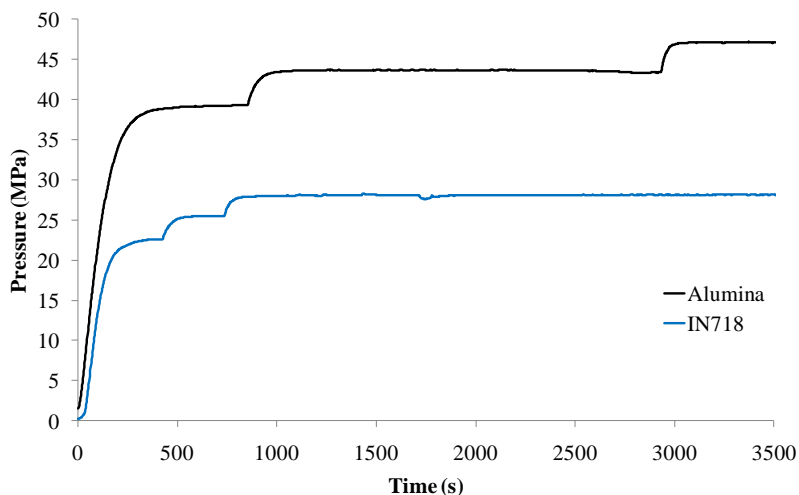
Figure 53 – Cylinder pressure during granulation of IN718 and alumina feedstocks with 54 vol.% of solids and a plain LDPE70 binder system. The temperature during granulation was 140 °C.
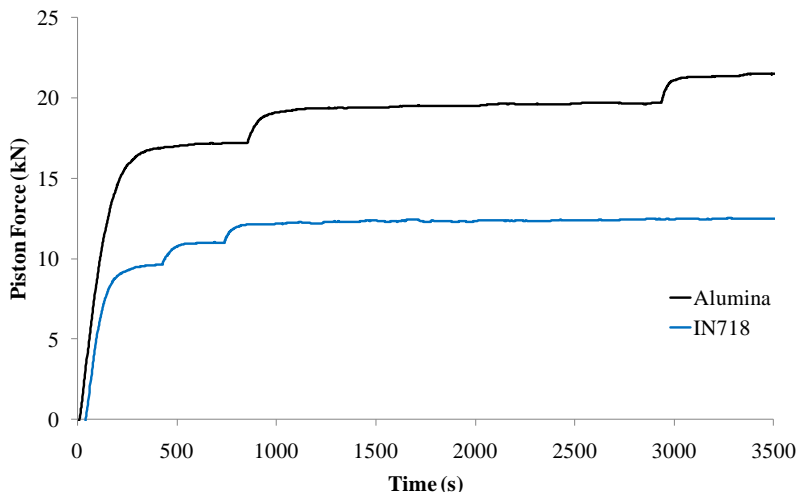
Figure 54 – Piston force during granulation of IN718 and alumina feedstocks with 54 vol.% of solids and a plain LDPE70 binder system. The temperature during granulation was 140 °C.

Table 12 – Average pressure and piston force at plateau during granulation of IN718 and alumina feedstocks at the three different shear rates and granulation speeds.

Feedstock	Shear rate (s^{-1})	Granulation speed (mm/min)	Average pressure (MPa)	Average piston force (kN)
Alumina	80	600	39.28	17.19
	100	750	43.49	19.66
	120	900	47.15	21.49
IN718	80	600	22.52	9.57
	100	750	25.47	10.99
	120	900	28.13	12.50

Figure 55 shows the plot of the average pressure versus the shear rate imposed to the feedstocks. Note that both feedstocks show roughly the same sensitivity to the shear rate, showing nearly the same increment on pressure with the increase of shear rate, which means that the difference on morphology and PSD of the powders have virtually no influence on the pseudoplasticity of the feedstocks for this shear rates range.

124
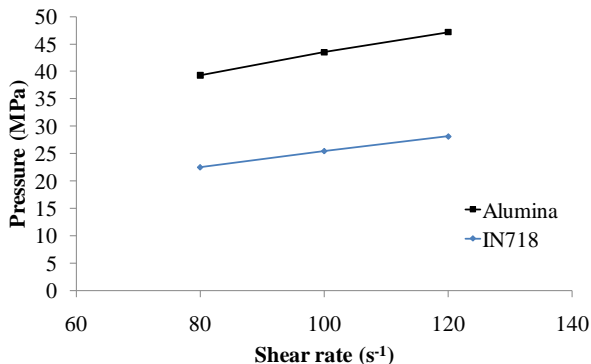
Figure 55 – Cylinder pressure as a function of shear rate during feedstock granulation.

The granules were then analyzed by TGA and compared with the TGA results of plain LDPE70. Again TGA was performed in forming gas from room temperature to 600 °C, with a heating rate of 5.0 °C/min. Figure 56 shows the TGA results of plain LDPE70, alumina-LDPE70 feedstock and IN718-LDPE70 feedstock. A slightly higher onset evaporation/degradation temperature could be noticed for the IN718-LDPE70 feedstock, probably related with the PSD of IN718 powder (GERMAN, 1990).
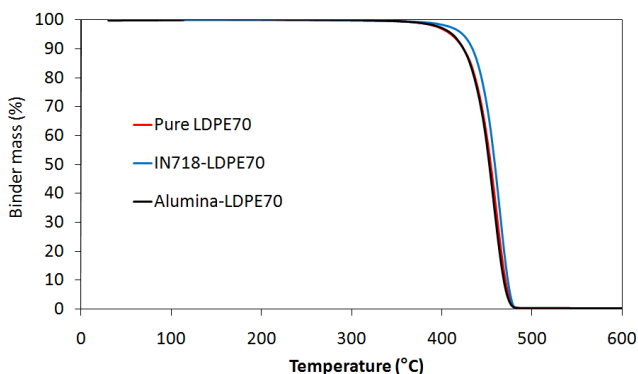
Figure 56 – Thermogravimetric analysis of plain LDPE70, alumina and IN718 based feedstocks. TGA was performed in forming gas. Total mass has been normalized to binder mass to make it easy to compare the three different analyses.

Alumina based feedstock was also analyzed in an oxygen rich atmosphere (air). The comparison between the TGA in the two different atmospheres is shown in Figure 57. It is clear the difference in kinetics behavior for the two different atmospheres. For an oxidizing atmosphere, the evaporation/degradation of the polymer occurs more gradually, during a larger temperature range, starting at a lower temperature (~250 °C) in comparison with a reducing atmosphere (~350 °C). The difference of degradation kinetics under reducing and oxidizing atmosphere is in agreement with the literature (GERMAN, 1990).
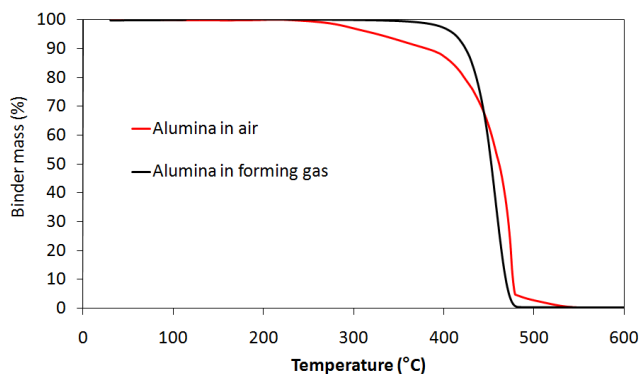
Figure 57 – Thermogravimetric analysis of alumina-LDPE70 based feedstocks performed in forming gas and in air. Total mass has been normalized to binder mass.

4.2.1.3. Warm-pressing

After granulation, disc-shaped samples were produced via warm-pressing. Figure 58 shows examples of IN718 and alumina warm-pressed samples. Densities achieved were close to theoretical as shown in Table 13. The theoretical density was calculated with the densities and volumes of particles and binders used to produce the feedstocks, considering a total absence of voids. This table also shows the average thickness of the samples. Note that the thickness was lower than 0.8 mm, which was the calculated thickness according to the amount of

granules pressed. This happened due to loss of feedstocks through the
gaps between die and punchers.
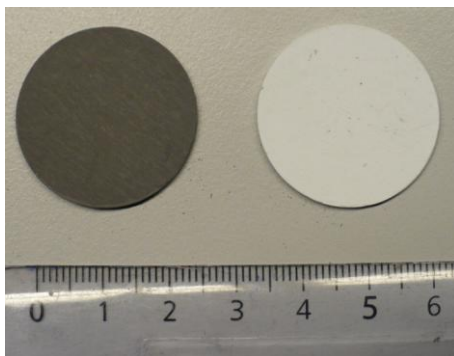
Figure 58 – IN718 and alumina warm-pressed
samples.

Table 13 – Density and thickness of warm pressed samples with a plain
LDPE70 binder system and 54 vol.% of solids.

Feedstock	Average density (g/cm³)	Theoretical density (g/cm³)	Percentage of theoretical density (%)	Average thickness (mm)
Alumina	2.561 ± 0.014	2.5827	99.15 ± 0.53	0.72 ± 0.05
IN718	4.807 ± 0.011	4.8466	99.18 ± 0.24	0.75 ± 0.04

Figure 59 and Figure 60 show the SEM images of the green
warm-pressed discs of alumina and IN718 powders, respectively. It can
be seen that the LPDE and the powders were homogeneously
distributed, with no segregation or clusters formation. Wetting of the
powders by LDPE was also good.
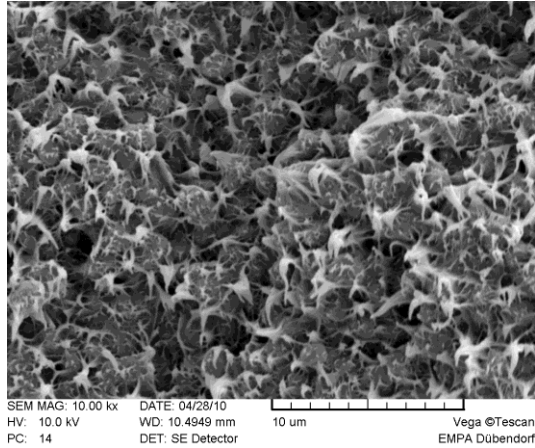
Figure 59 – SEM image of a green warm-pressed alumina disc, with 54 vol.% of solids and plain LDPE70. Magnification: 10000 x.
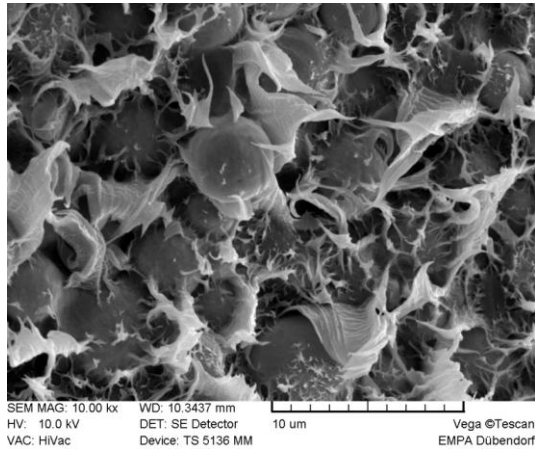
Figure 60 – SEM image of a green warm-pressed IN718 disc, with 54 vol.% of solids and plain LDPE70. Magnification: 10000 x.

4.2.1.4. Thermal debinding

According to the TGA analyses of LDPE70 and the feedstocks, the debinding program should be carried until a temperature of at least 500 °C. To assure the complete binder removal, a basic program was defined to be at 600 °C, with a heating rate of 0.5 °C/min and a dwell time of 60 min. The low heating rate was defined to avoid as much as possible the formation of blisters, without however impractically extending the debinding cycle.

Debinding of alumina samples was carried out in oxidizing atmosphere (air) and in reducing atmosphere (forming gas), whereas debinding of IN718 was performed only in reducing atmosphere. The pictures of the samples after debinding are shown in Figure 61. As it can be seen, the alumina sample submitted to debinding in air has shown a perfect defect-free sample, with no blisters, no deformation, no warping, no edge rounding and no color change. On the other hand, both alumina and IN718 discs, submitted to debinding in reducing atmosphere, underwent edge rounding, deformation and blister formation. These defects are more likely to happen in single component binder systems, such as the one used (GERMAN, 1990). The alumina sample debinding in forming gas has shown also a slight darkening due to carburization, which can also be seen in the alumina support (in the picture background). It is presumed that IN718 samples have also undergone carburizing, since the binder system and debinding cycle were the same, however it is not visible due to the originally dark color of the IN718 feedstock.

| (a) | (b) | (c) |
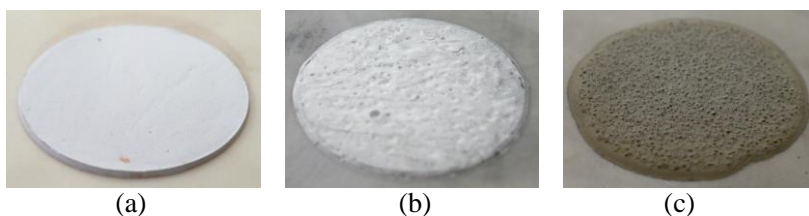
Figure 61 – Picture of disc-shaped samples after thermal debinding. (a) Alumina in oxidizing atmosphere, (b) alumina in reducing atmosphere and (c) IN718 in reducing atmosphere.

The difference in debinding behavior in air and in forming gas was somehow predicted, due to the difference observed in the TGA of

alumina samples showed in Figure 57. As the evaporation/degradation rate of LDPE70 in air is lower and happens in a larger temperature interval, it avoids the formation of blisters. Blisters happen when the rate of formation of vapor or degradation gases is faster than the rate of diffusion of these gases through the compact towards the surface (GERMAN, 1990).

Edge rounding, on the other hand, is related with the temperature in which debinding starts. As shown in Figure 57, for debinding in air, polymer extraction starts at 250 °C, whereas for debinding in forming gas considerable amount of polymer starts to be extracted just at 350 °C. Considering a lower heating rate, 0.5 °C/min, when the material reaches 350 °C in air, a great amount of binder, if not all of it, has already been removed. When the debinding is carried in reducing atmosphere, at 350 °C nearly no binder has yet been removed and, as the viscosity of the binder reduces drastically with temperature, deformation and edge rounding at such higher temperatures is much more likely to occur.

Moreover edge rounding and deformation is also closely related with the inter-particle friction. As the polygonal shape of the alumina particles offers a much higher inter-particle friction than the round IN718 particles, the IN718 samples underwent considerably higher deformation and edge rounding, as it can be seen in Figure 61c.
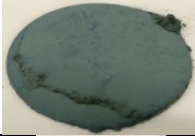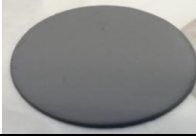
All programs have successfully removed all the binder. For the debinding of the alumina sample in air, 100.00 % of binder was removed[7]. In forming gas, 100.00 % and 98.53 % of the binder was removed from the alumina and IN718 samples, respectively.

Finally, various debinding programs were used to test the possibility of reducing defect formation during debinding of IN718 disc-shaped samples. Table 14 shows the programs used and images of the samples afterwards.

Program #1 shows that an oxidizing atmosphere, although detrimental to the metallic powder due to oxidation, reduces deformation and eliminates blister formation. However, edge rounding still occurred, which shows that this type of defect is more influenced by the powder characteristics.

---

[7] The actual values of removed binder for the alumina samples after debinding in air and in forming gas were 102.51 % and 101.59 %, respectively. However the maximum amount of binder passive to be removed is, obviously, 100.00 % and therefore this was the reported value for both samples.

Table 14 – Various debinding programs imposed to the IN718 disc-shaped samples in the attempt to reduce defects formation during thermal debinding. The parameters that differ from the basic program are highlighted. As a reference, the basic program is also shown as program #0.

#	Temperature (°C)	Dwell time (min)	Heating rate (°C/min)	Atmosphere	Binder removed (%)	Image
0	600	60	0.5	Forming gas	98.53	
1	600	60	0.5	**Air**	N/A[a]	
2	600	60	**0.1**	Forming gas	N/A[b]	*Fractured sample.
3	600	60	**1.0**	Forming gas	98.10	
4	**300** 600	**0** 60	**5.0** 0.5	Forming gas	98.04	
5	**250**	60	0.5	Forming gas	N/A[c]	

 a – The actual amount of binder removed in the sample submitted to debinding in air is unknown, because the oxidation caused by the oxidizing atmosphere increases sample weight, due to incorporation of oxygen in the structure of the material.
b – Data not measured due to fracture of the sample.
c – Data not measured, but expected to be 0.00 %.

From program #2 it is still possible to see that the amount of blisters reduced significantly by reducing the heating rate, which is coherent and expected, since the extraction gases have more time to diffuse through the compact, nevertheless some blisters still occurred. To remove them an even lower heating rate would be necessary, what would be impracticable; the debinding time for program #2 was already 95 hours.

The result of program #3 shows that a higher heating rate seemed not to be relevant for blister formation and deformation. The results were roughly the same as for the basic program.

The idea of program #4 was to reduce the exposure time of the sample to high temperature before the extraction of the polymer was triggered, in an attempt to reduce deformation and edge rounding. This program seemed to be effective and deformation was reduced; however another type of defect occurred, and the sample showed a peeling defect.

Finally program #5 has been made just to confirm that until 250 °C, temperature at which debinding of PW triggers, no deformation, edge rounding or blisters occur.

4.2.2. Alumina feedstock with plain LDPE02

In order to avoid the formation of defects during debinding, an alumina based feedstock with a LDPE02 was investigated. The proposal was to check if the debinding defects, such as edge rounding, deformation and, eventually, blisters formation would be reduced with the use of a low melt flow index LDPE.

4.2.2.1. Mixing

Figure 62 and Figure 63 show the plot of torque and temperature versus time during pre-mixing and mixing of the feedstock of alumina powder with 54 vol.% of solids with plain LDPE02 binder. The mixing behavior was the same as for the feedstock with LDPE70 as binder, with an initial increase of torque as the temperature decrease, followed by a period of torque and temperature stabilization.
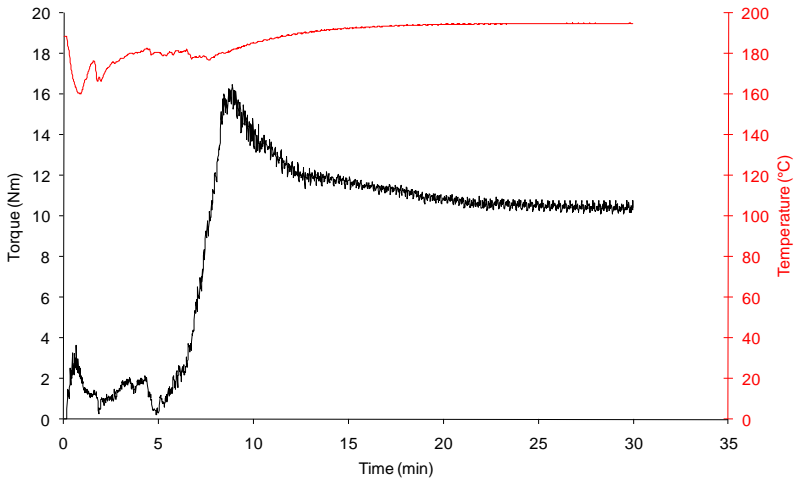
Figure 62 – Plot of pre-mixing torque and temperature versus mixing time of 54 vol.% of alumina powder with a plain LDPE02 binder system.
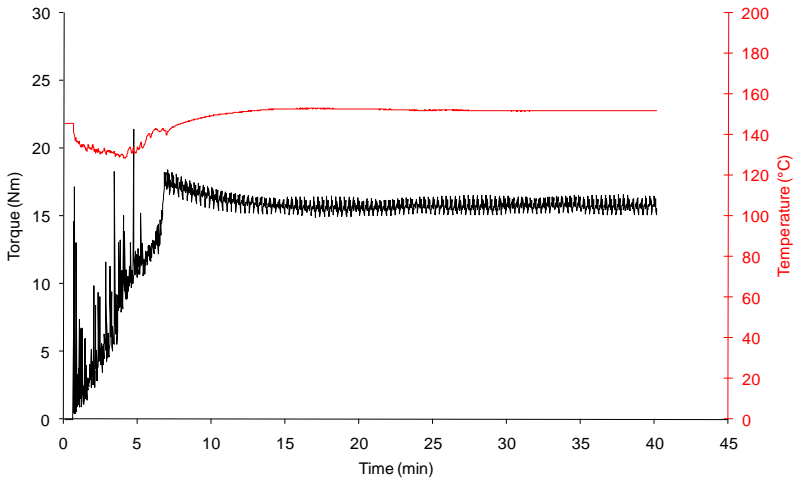
Figure 63 – Plot of final mixing torque and temperature versus mixing time of 54 vol.% of alumina powder with a plain LDPE02 binder system.

Figure 64 compares the final mixing of the alumina powder with LDPE70 and LDPE02. As it can be seen in Figure 64, the higher

viscosity of LDPE02 produces higher mixing torques (2.65 times higher).
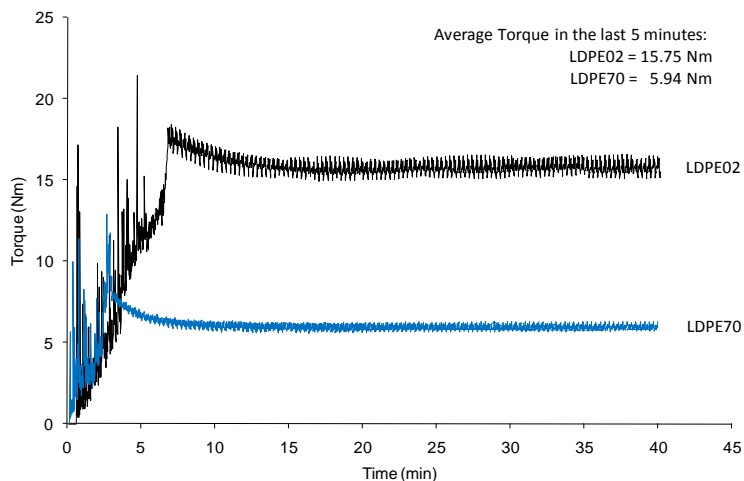
Figure 64 – Plot of final mixing torque versus time of alumina feedstocks with LDPE70 and LDPE02 as binders, with 54 vol.% of solids. The mixing temperature at stable torque stage was 152 °C.

4.2.2.2.   Granulation

The granulation of the feedstock was carried out the same way and in the same conditions as previously described for the feedstocks using LDPE70 as binder. Figure 65 and Figure 66 show the cylinder pressure and the piston force, respectively, during granulation of LDPE02 and LDPE07 based feedstocks. Each plateau corresponds to the stabilization of pressure or force at the three different shear rates and their corresponding granulation speeds. Table 15 shows the average pressure and piston force during granulation at the three different granulation speeds and shear rates.
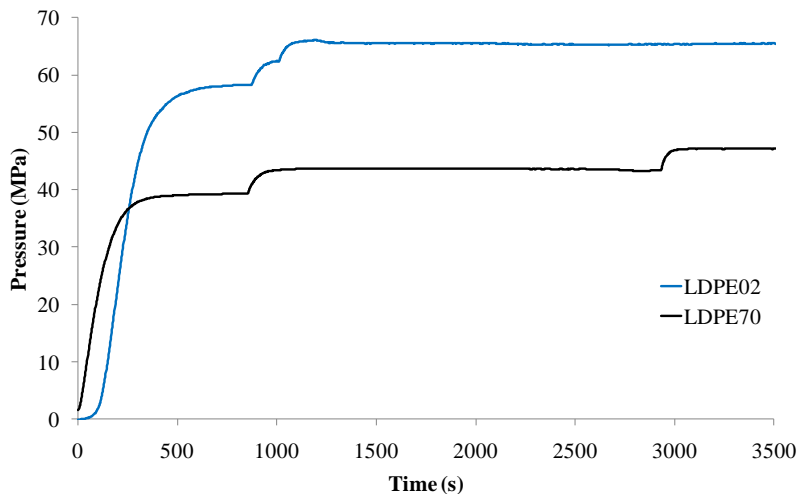
Figure 65 – Cylinder pressure during granulation of alumina feedstocks with 54 vol.% of solids, with two different binders: LDPE70 and LDPE02. The temperature during granulation was 140 °C.
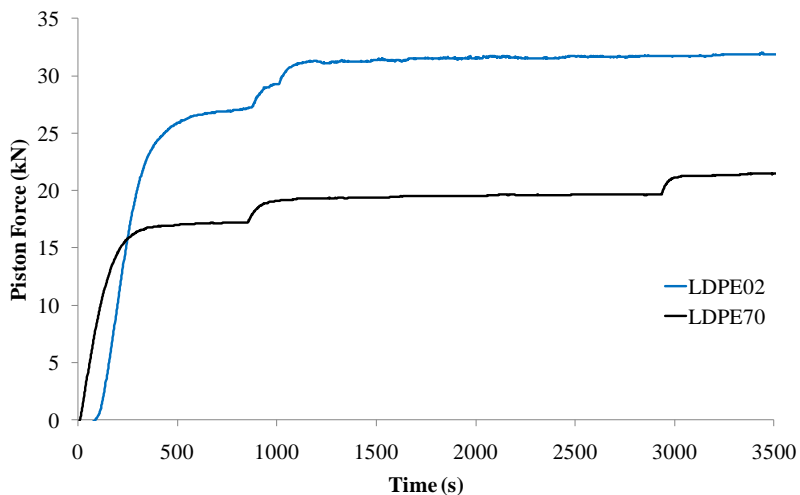
Figure 66 – Piston force during granulation of alumina feedstocks with 54 vol.% of solids, with two different binders: LDPE70 and LDPE02. The temperature during granulation was 140 °C.

Table 15 – Average pressure and piston force at plateau during granulation of alumina feedstocks with LDPE02 and LDPE70 at the three different shear rates and granulation speeds.

Binder	Shear rate (s^{-1})	Granulation speed (mm/min)	Average pressure (MPa)	Average piston force (kN)
LDPE70	80	600	39.28	17.19
	100	750	43.49	19.66
	120	900	47.15	21.49
LDPE02	80	600	58.16	27.00
	100	750	62.30	29.22
	120	900	65.55	32.17

Figure 67 shows the plot of the average pressure versus the shear rate imposed to the feedstocks. Note that again both feedstocks show roughly the same sensitivity to the shear rate, showing nearly the same increment on pressure with the increase of shear rate, which means that both LDPE's have the same influence on the pseudoplasticity of the feedstocks for this shear rates range.
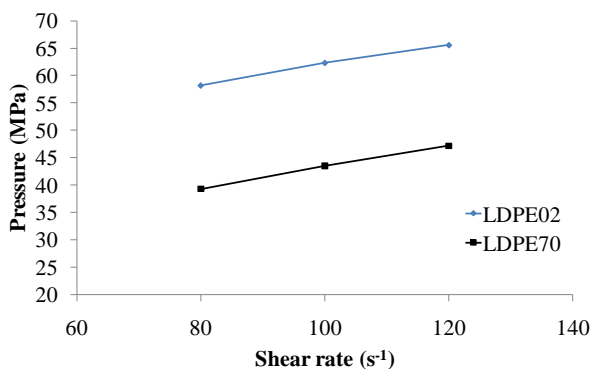
Figure 67 – Cylinder pressure as a function of shear rate during feedstock granulation of alumina based feedstocks with LDPE02 and LDPE70 as binders.

4.2.2.3. Warm-pressing

After granulation, warm-pressed disc-shaped samples were also produced for the alumina feedstock with LDPE02 as binder. This time, to achieve high densities and defect-free warm-pressed samples, a higher pressing temperature (148 °C) had to be used. This happened because of the higher viscosity (lower melt flow index) and higher melting point of LDPE02. Table 16 compares the characteristics of the warm-pressed discs of alumina with LDPE02 and LDPE70 as binder. What is worthy to highlight here is the higher thickness of the LDPE02 samples. This is related with the smaller amount of feedstock slipping through the gaps between die and punchers during warm-pressing, which is another consequence of the higher viscosity of LDPE02.

Table 16 - Density and thickness of warm pressed alumina samples with plain LDPE70 and plain LDPE02 binder systems, with a solids load of 54 vol.%.

Binder	Average density (g/cm^3)	Theoretical density (g/cm^3)	Percentage of theoretical density (%)	Average thickness (mm)
LDPE70	2.561 ± 0.014	2.5827	99.15 ± 0.53	0.72 ± 0.05
LDPE02	2.565 ± 0.006	2.5878	99.11 ± 0.23	0.81 ± 0.01

4.2.2.4. Debinding

Warm-pressed samples of alumina feedstock with LDPE70 and LDPE02 binders were submitted to the basic debinding program at 600 °C, with a heating rate of 0.5 °C/min and a dwell time of 60 min, in forming gas. The program successfully removed 100.00 % of the binder in both samples, with LDPE70 and LDPE02[8]. Figure 68 shows the pictures of both samples after debinding. As it can be seen, the use of LDPE02 did not help to remove the defects found in the samples with LDPE70, *i.e.* blisters, edge rounding and deformation, and both samples showed apparently the same amount of such defects. The use of LDPE02 was thus discontinued and LDPE70, with lower viscosity (higher melt flow index), was the only polyethylene used as binder

---

[8] Again the real calculated values of the binder removal was 101.70 % for the sample with LDPE70 and 101.27 % for the sample with LDPE02.

further in this work. The selection of the LDPE with lower viscosity was not to reach too high pressures during the extrusion of the tubes, whose feedstocks would have incorporated fibers, which would by itself increase the extrusion pressure.

(a)　　　　　　　　　(b)
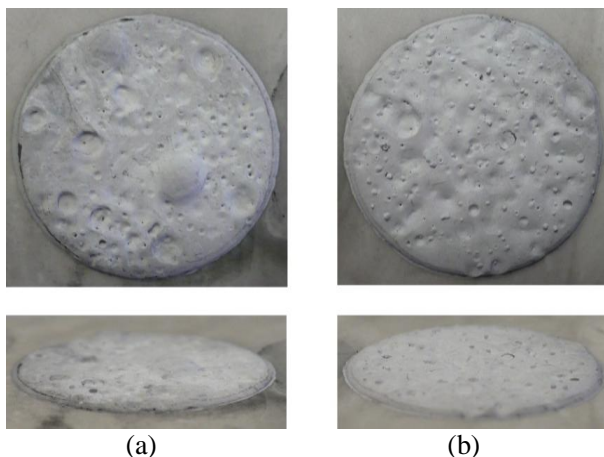
Figure 68 – Alumina discs with 54 vol.% of solids. (a) plain LDPE70 and (b) plain LDPE02 as binders after debinding program.

4.3. FEEDSTOCK DEVELOPMENT

4.3.1. Filling level definition

To define the solid volume content, alumina has been chosen to be the powder tested for two reasons. Firstly, an economical reason, the lower price and the larger amount of this powder available. The second reason, from an engineering point of view, was the higher viscosity of the alumina feedstock with 54 vol.% of solids, compared with the viscosity of the IN718 feedstock shown in the preliminary tests. The higher torque of the alumina feedstock could, eventually, limit the solid content to a level that the mixing torque would not exceed the equipment maximum permitted torque. Here it is worthy to remember

that both feedstocks, for alumina and IN718 powders, would have in the end the same characteristics, *i.e.* filling level and binder system composition. Plain LDPE70 was the only polymer used in the binder system for the filling level definition.

4.3.1.1. Mixing

The range of solids volume content tested was, as mentioned previously, 54, 56, 58, 60 and 62 vol.%. Figure 69 and Figure 70 show the plot of the torque versus time during pre-mixing and final mixing of the alumina powder with LDPE70. The conditions of pre-mixing and final mixing were the same for all filling levels as described in the previous section.
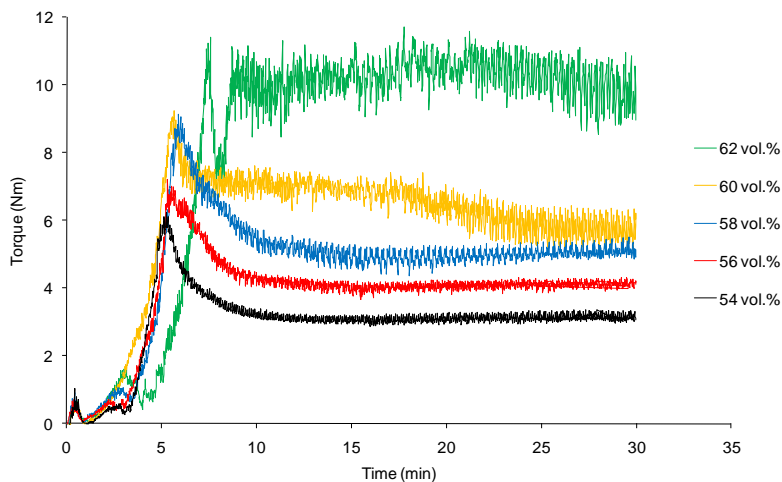
Figure 69 – Plot of mixing torque versus time during pre-mixing of alumina feedstocks with 54, 56, 58, 60 and 62 vol.% of solids at 180 °C.
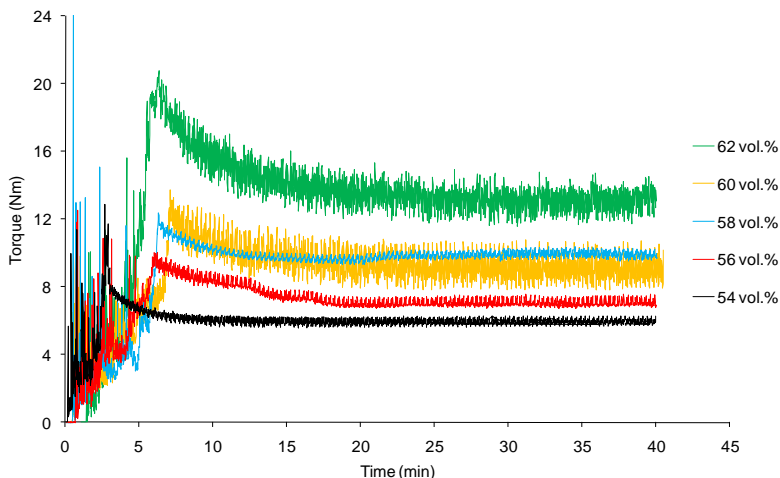
Figure 70 – Plot of mixing torque versus time during final mixing of alumina feedstocks with 54, 56, 58, 60 and 62 vol.% of solids at 152 °C.

The evolution of the mixing torque with increase of filling level occurred as expected, *i.e.* the higher the filling level, the higher the mixing torque (GERMAN, 1990). Another expected characteristic was the level of noise in the curves that increased for higher filling levels, that can be noticed clearly in the mixing curves of the feedstocks with 60 and 62 vol.% of solids. The level of noise for increased filling levels is due to the increasing interaction of particles as they get closer to each other as the binder amount decreases. Figure 71 shows the average torque of the final mixing and the corresponding error bars, which are associated with the level of noise in the data. In Figure 70, the mixing torque of the feedstock with 58 vol.% has overcome the mixing torque of the feedstock with 60 vol.%, however, the level of noise of the latter may confuse the results, as shown by the error bars in Figure 71. Moreover, an error associated with the calibration of the machine may have influenced the average torque of both curves, 58 and 60 vol.%.
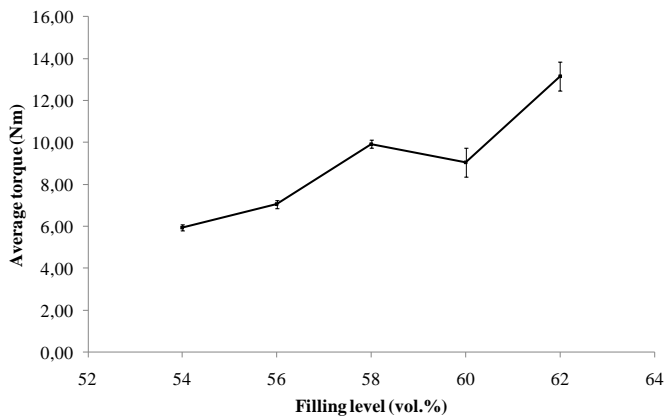
Figure 71 – Average torque during final mixing versus filling level for alumina feedstock with plain LDPE70.

4.3.1.1.1. *Maximum filling level calculation*

To calculate the maximum filling level the volume content ratio between LDPE70 and Alumina powders (LDPE/Al_2O_3) was plotted versus 1/torque, as shown in Figure 72. The extrapolation of the line to the point where the inverse of torque is equal to zero, *i.e.* torque is infinite, gives the minimum LDPE/Al_2O_3 ratio where the amount of Al_2O_3 is maximum. The minimum LDPE/Al_2O_3 ratio value was calculated with the regression equation of Figure 72. Table 17 shows the values of the inverse of torque and LDPE/Al_2O_3 ratio, including the extrapolated value. Using this method, the maximum filling level was found to be 71.4 vol.% of solids.
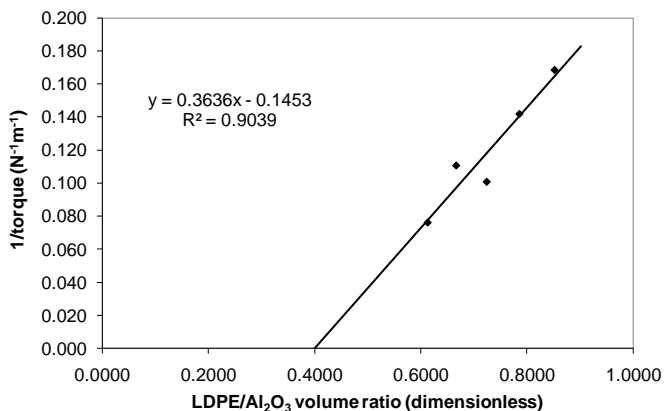
Figure 72 – Regression curve and equation of LDPE/Al$_2$O$_3$ ratio versus inverse of torque.

Table 17 – Solid load and torque data according to measured values and calculated values according to regression equation from Figure 72.

Solids load (vol.%)	LDPE/Al$_2$O$_3$ volume ratio (dimensionless)	Torque (Nm)	Inverse of torque (N^{-1}m^{-1})
54.00	0.8519	5.94	0.168
56.00	0.7857	7.05	0.142
58.00	0.7241	9.93	0.101
60.00	0.6667	9.05	0.111
62.00	0.6129	13.2	0.076
71.4*	0.400*	∞	0.000

* Extrapolated values according to regression equation.

4.3.1.1.2. Viscosity models comparison

From the various proposed viscosity models found in the literature, six among the most cited models were chosen to be compared with the torque data versus filling level discussed in the previous sub-session. The chosen models were the following:

  i.   *Eilers' model* – Equation 9;
  ii. *Mooney's model* – Equation 10;
  iii. *Kriger and Dougherty's model* – Equation 11;
  iv. *Frankel and Acrivos' model* – Equation 12;

      v.   *Chong's model* – Equation 13;
     vi.   *Quemada's model* – Equation 14.

Note that all these models correlate solids load and the apparent viscosity. In this work, no viscosity data was calculated, and the solids load was correlated with the mixing torque instead. It was thus assumed that the torque and the apparent viscosity are directly proportional for the feedstock in question. Moreover, for all the models the constant η_0 had to be defined, which is the apparent viscosity of the unfilled binder. For that a mixing run of plain LDPE70, under the same conditions of the feedstock mixing, was made. The average torque for the plain LDPE70 was 0.61 ± 0.02 Nm. In the models the maximum filling level ϕ_m, calculated in the previous section, is also included. The remaining empirical constants of the models were arbitrarily chosen to best fit the results.

Figure 73 shows the plot of the fitted models and the measured torque data as a function of the filling level. For low volume fractions (low filling levels), until approximately 0.3, all the models showed more or less the same behavior. From 0.3 on, Mooney's and Quemada's models exhibited a much faster torque increase with volume fraction. The models of Chong, Krieger-Dougherty and Eilers have shown an almost identical behavior. On its turn, the model of Frankel and Acrivos was definitely the one that best fitted the results of the present work. Figure 74 show a detail from the curves of Figure 73 around the volume fraction of the measured data, to show the fitting of the models in this region.
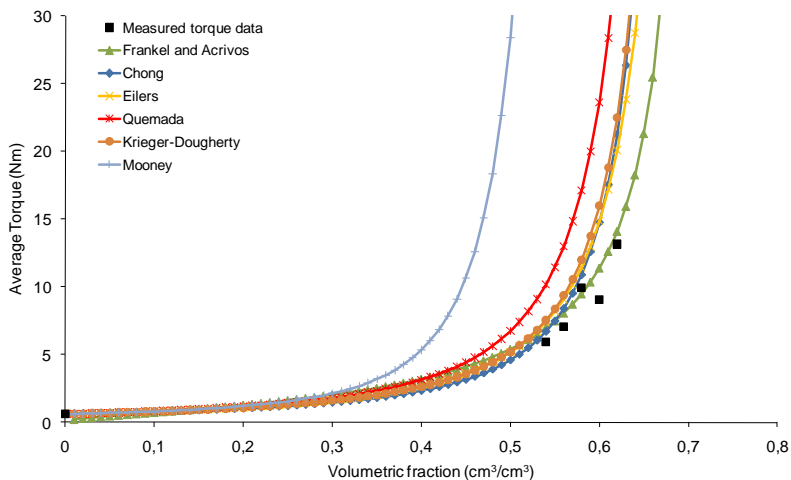
Figure 73 – Plot of filling level versus mixing torque of alumina feedstocks compared with various viscosity models.
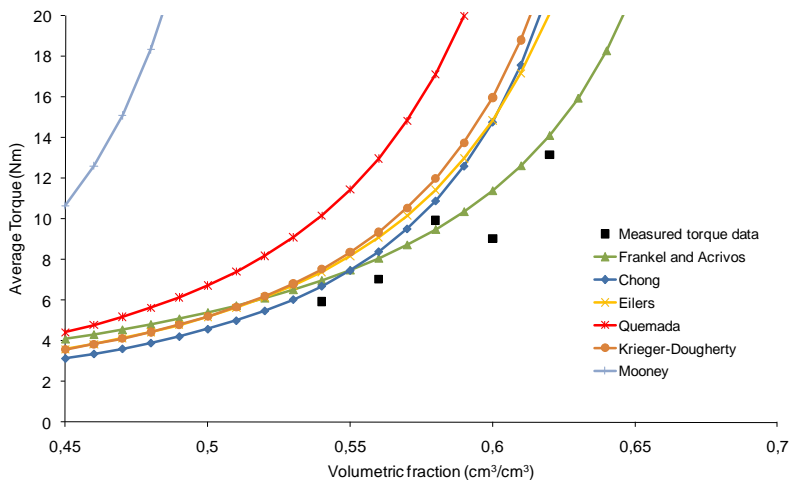
Figure 74 – Detail of the plot of filling level versus mixing torque of alumina feedstocks compared with various viscosity models, in the region of the measured data.

144

4.3.1.2. Granulation

Granulation was performed under the same conditions as before. Due to high abrasion effect of the feedstock, the o-ring around the piston, which avoids back-flow of the feedstock during granulation (extrusion), has broken during granulation of all different feedstocks, yielding no good results. For this reason these data were not considered in this work.

4.3.1.3. Warm-pressing

Disc shaped samples, with filling levels varying from 54 to 62 vol.%, were warm-pressed at 140 °C. Table 18 summarizes the characteristics of the produced discs.

Table 18 – Density and thickness of warm-pressed alumina samples with plain LDPE70 with different filling levels.

Filling level	Average density (g/cm³)	Theoretical density (g/cm³)	Percentage of theoretical density (%)	Average thickness (mm)
54	2.561 ± 0.014	2.5827	99.15 ± 0.53	0.72 ± 0.05
56	2.633 ± 0.001	2.6444	99.55 ± 0.03	0.79 ± 0.01
58	2.693 ± 0.003	2.7060	99.52 ± 0.10	0.79 ± 0.01
60	2.749 ± 0.004	2.7676	99.31 ± 0.13	0.79 ± 0.01
62	2.790 ± 0.004	2.8292	98.61 ± 0.15	0.80 ± 0.00

4.3.1.4. Debinding

The samples with different filling levels were submitted to the basic debinding program. The program successfully removed 100.00% of the binder[9] in samples with filling level from 54 to 60 vol.%; the sample with 62 vol.% of solid had 99.70 % of the binder removed. Figure 75 shows the pictures of the samples after debinding. As it can be

[9] The real calculated values were 100.53, 101.10, 100.20 and 100.25 % for the samples with 54, 56, 58 and 60 vol.% of solids, respectively.

seen, the filling level did not have any influence on the blisters. However, with increasing of filling level, edge rounding has been significantly improved. The sample with 62 vol.% of solids showed no edge rounding. Based on these results, the filling level was defined to be 62 vol.% for further studies in the present work. This value is also much lower than the calculated maximum filling level (71.4 vol.%), which is good to avoid amplified volume errors due to weighting errors (GERMAN, 1990), as shown in Figure 16. The optimal filling level should have 2 to 5 vol.% less powder than the maximum filling level (GERMAN, 1990); however, as fibers would be introduced in the system afterwards, and the high aspect ratio of the fibers would decrease the maximum filling level (GERMAN, 1990), it was decided to keep the filling level at 62 vol.%, which is about 9.6 vol% lower than the calculated maximum filling level.

(a)   (b)   (c)

(d)   (e)
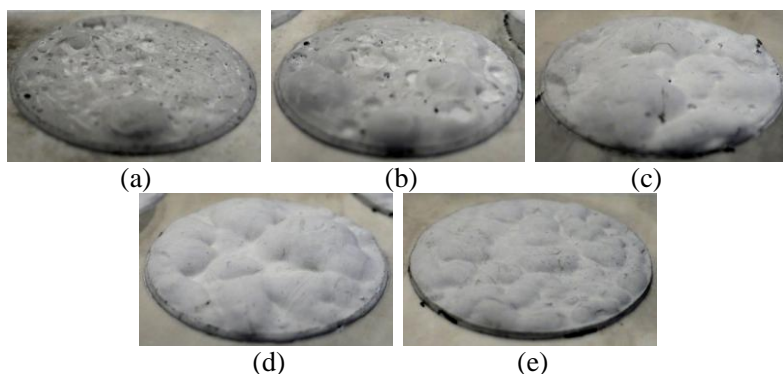
Figure 75 – Alumina discs with filling levels of (a) 54, (b) 56, (c) 58, (d) 60 and (e) 62 vol.% after debinding program.

4.3.2. Paraffin wax content definition

To define the paraffin content, feedstocks with alumina and IN718 powders were prepared with binder systems composed by 5.0 vol.% of stearic acid and different amounts of paraffin wax, with the balance of LDPE70. The PW volume contents tested are shown in Table 19 and Figure 76.

Table 19 – Binder composition of alumina and IN718 feedstocks during tests to define PW content. All feedstock had a filling level of 62 vol.%.

Binder formulation	LDPE (vol.%)	PW (vol.%)	SA (vol.%)
1	95.0	0.0	5.0
2	75.0	20.0	5.0
3	70.0	25.0	5.0
4	65.0	30.0	5.0
5	56.0	39.0	5.0
6	47.5	47.5	5.0
7	0.0	95.0	5.0
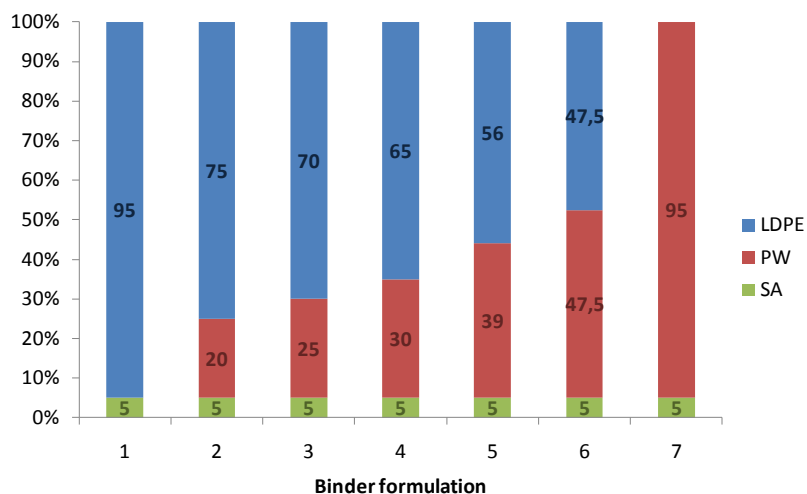
Figure 76 – Binder composition of alumina and IN718 feedstocks during tests to define PW content. All feedstock had a filling level of 62 vol.%.

4.3.2.1. Mixing

Figure 77 and Figure 78 show the plot of the torque versus mixing time during final mixing of the alumina and IN718 feedstocks with the different binder systems. The conditions of mixing were the same as performed previously. As expected the mixing torque decreased with the increasing amount of PW.
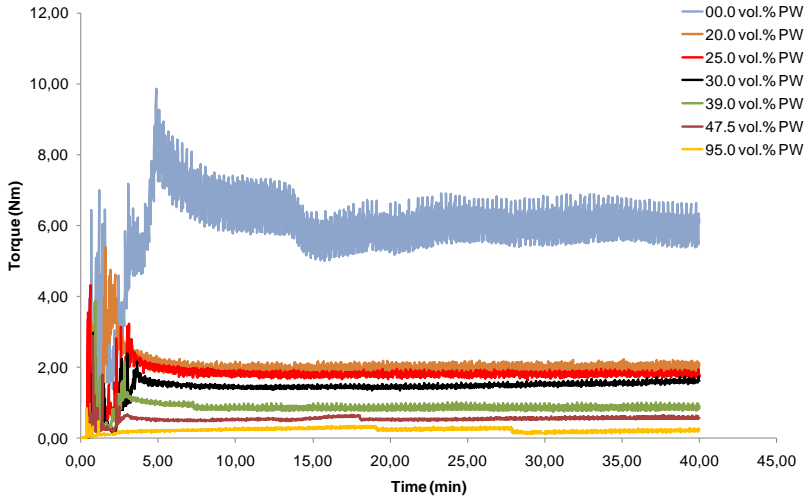
Figure 77 – Plot of mixing torque versus time during final mixing of alumina feedstocks with different binder systems and 62 vol.% of solids at 152 °C. All binders systems have 5 vol.% of PW and the balance of LDPE70.
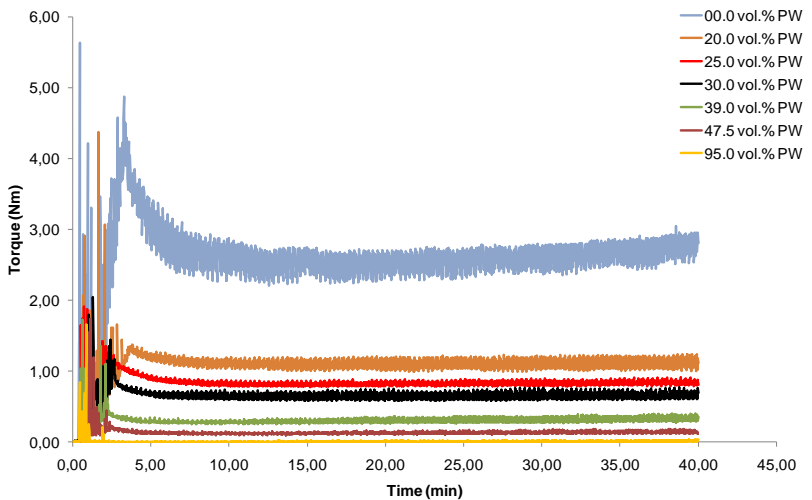
Figure 78 – Plot of mixing torque versus time during final mixing of IN718 feedstocks with different binder systems and 62 vol.% of solids at 152 °C. All binders systems have 5 vol.% of PW and the balance of LDPE70.

Figure 79 shows the evolution of mixing torque with the PW volume content. As it can be seen, the influence of PW on the mixing torque is very high, and with 20 vol.% the mixing torque, for both alumina and IN718 feedstocks, have drop to roughly one third of the torque without PW. The torque keeps decreasing fast with addition of PW until an amount of 47.5 vol.%, *i.e.* LDPE/PW ratio equals to unit. After that, the feedstock viscosity is approximately the same as a feedstock composed only of PW (95 vol.%) and SA (5 vol.%).
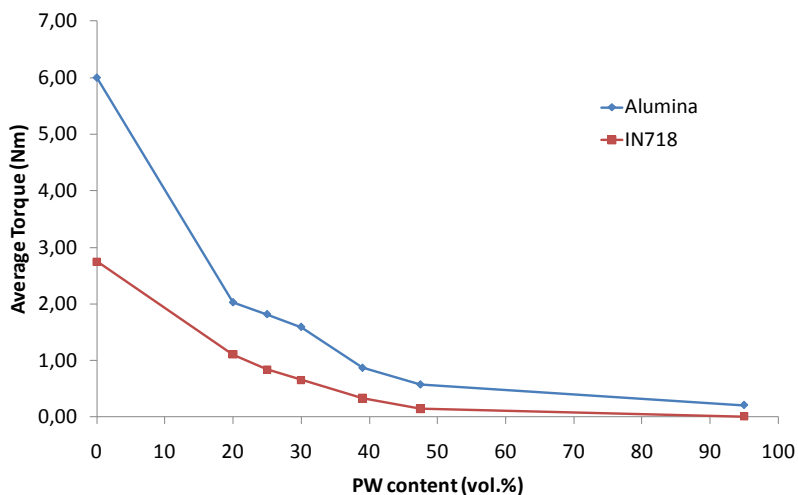
Figure 79 – Evolution of mixing torque with increase of PW volume content and corresponding decrease of LDPE70 content. The amount of SA was fixed in all binders at 5 vol.%.

4.3.2.2. Granulation

The granulation of the alumina and IN718 feedstocks was performed such as previously done for the feedstocks with plain LDPE70. Nevertheless the granulation pressures were too low, lower than the measuring range of the pressure transducers. For this reasons, this data were not explored.

4.3.2.3. Warm-pressing

The decrement of viscosity with the addition of PW has had a very high effect on the facility of the feedstock to flow from the warm-pressing die, through the gaps between punchers and die. For this reason the warm-pressing of the feedstocks containing SA and PW was carried in lower temperatures compared with the feedstocks with plain LDPE. Table 20 summarizes the characteristics of the produced warm-pressed discs, as well as their pressing temperature.

Table 20 – Warm-pressing temperature, density and thickness of warm-pressed alumina and IN718 samples with different binder systems. All binder system contains 5 vol.% of SA and LDPE as balance.

Powder	PW content (vol.%)	Pressing Temperature (°C)	Average density (g/cm^3)	Theoretical density (g/cm^3)	Percentage of theoretical density (%)	Average thickness (mm)
Alumina	0	130	2.767*	2.8278	97.85*	0.76*
Alumina	20	130	2.763 ± 0.012	2.8271	97.71 ± 0.43	0.79 ± 0.02
Alumina	25	130	2.762 ± 0.008	2.8269	97.69 ± 0.28	0.76 ± 0.02
Alumina	30	120	2.748 ± 0.013	2.8267	97.23 ± 0.45	0.75 ± 0.07
Alumina	39	115	2.713 ± 0.061	2.8264	95.99 ± 2.15	0.79 ± 0.04
Alumina	47.5	105	2.718 ± 0.011	2.8261	96.17 ± 0.38	0.82 ± 0.03
IN718	0	120	5.407 ± 0.004	5.4169	99.82 ± 0.08	0.78 ± 0.07
IN718	20	120	5.421 ± 0.022	5.4162	100.10 ± 0.14	0.77 ± 0.03
IN718	25	120	5.433 ± 0.010	5.4160	100.31 ± 0.18	0.77 ± 0.02
IN718	30	115	5.423 ± 0.023	5.4158	100.14 ± 0.43	0.68 ± 0.11
IN718	39	100	5.450 ± 0.041	5.4155	100.63 ± 0.76	0.65 ± 0.08
IN718	47.5	95	5.448 ± 0.041	5.4152	100.60 ± 0.75	0.77 ± 0.05

* Only one sample was produced, no statistical data available.

Figure 80 and Figure 81 show the SEM images of the green warm-pressed discs of alumina and IN718 feedstocks. The figures compare the feedstocks with 54 vol.% of solids with binder system composed of plain LDPE and the feedstocks with 62 vol.% of solids with binder system composed of 5 vol.% of SA, 30 vol.% of PW and 65 vol.% of LDPE. Comparing images (a) and (b) of Figure 80 and Figure 81 it can clearly be seen the reduced amount of binder in between the particles, due to the higher solids content. The wetting of the binder

150

remained good and also no segregation of particles or clusters were found.

(a) (b)
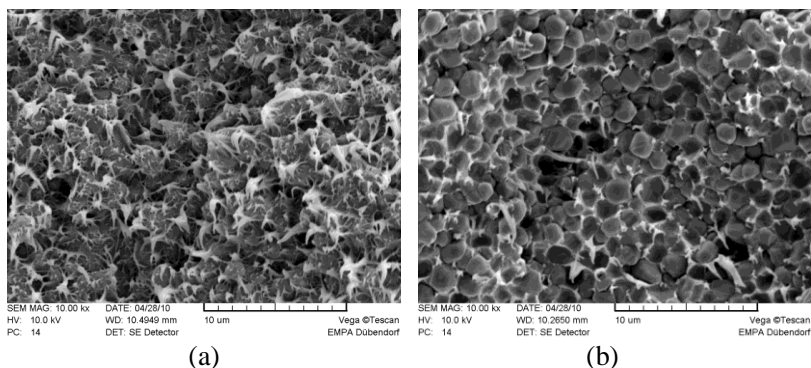
Figure 80 – SEM images of green warm-pressed alumina discs. (a) 54 vol.% of solids and plain LDPE as binder. (b) 62 vol.% of solids and binder system composed of 5 vol.% of SA, 30 vol.% of PW and 75 vol.% of LDPE. Magnification: 10000 x.

(a) (b)
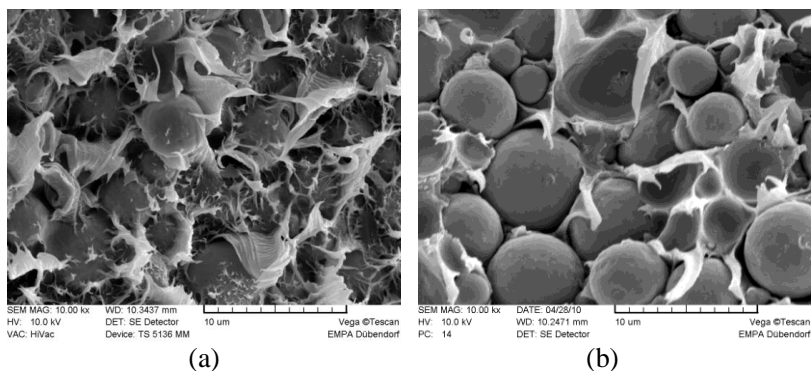
Figure 81 – SEM images of green warm-pressed IN718 discs. (a) 54 vol.% of solids and plain LDPE as binder. (b) 62 vol.% of solids and binder system composed of 5 vol.% of SA, 30 vol.% of PW and 75 vol.% of LDPE. Magnification: 10000 x.

4.3.2.4.   Thermal debinding

Alumina and IN718 warm-pressed discs with the different binder systems, summarized in Table 20, were submitted to the basic thermal debinding program in forming gas atmosphere. Table 21 shows the percentage of binder removed from all discs. As it can be seen, the debinding process successfully removed almost all the binder of the discs. A lower percentage of binder removal from the IN718 discs may be attributed to a slight oxidation of the samples, which increases the weight of the metallic powder. The weight increment input an error in the calculation of the binder removal percentage that is made by weighting of the samples. This explains the lower binder removal value of the IN718 sample with 47.5 vol.% of PW. For this sample, the o-ring that seals the furnace probably have not been correctly positioned, allowing more oxygen entering the furnace and contaminating the atmosphere.

Table 21 – Percentage of binder removed from alumina and IN718 discs with different binder systems.

Powder	PW content (vol.%)	Binder removed (%)
Alumina	0	99.91
Alumina	20	99.11
Alumina	25	99.17
Alumina	30	99.33
Alumina	39	99.12
Alumina	47.5	99.58
IN718	0	96.66
IN718	20	95.18
IN718	25	95.30
IN718	30	94.55
IN718	39	94.23
IN718	47.5	87.59

Figure 82 and Figure 83 show the discs after the debinding process. As it can be seen, the introduction of PW and SA in the binder system solved the problem of blister formation. This happened because the removal of binder occurred in two steps. First, the SA and PW were removed at temperatures around 260 and 300 °C, respectively, leaving a porous structure behind that allows the free flow of LDPE degradation

gases, which are produced in the second step of the thermal debinding, at temperatures around 460 °C.

It can also be seen that the minimum amount of PW for alumina and IN718 feedstocks is different, 25 vol.% for the alumina feedstock and 30 vol.% for IN718 feedstocks. Below these values blisters starts to disrupt on the surface of the samples. The different limits of PW content are correlated with the difference in powder morphology and PSD which leads to a different powder packing factor (GERMAN, 1990), probably denser for the IN718 powder. Denser packing makes debinding slower for the IN718 powder, which makes the samples of this powder more prone to blister formation. With this results the PW volume content has being defined to 30 vol.% of the binder system, so that both alumina and IN718 show no blister formation during debinding. This result is in agreement with what is found in the literature, which states that a minimum of 30 vol.% of low molecular binder should be used to form a sufficient interconnected network, alloying efficient solvent debinding, which could later provide an interconnected porous network for the subsequent thermal debinding (GERMAN, 1990).

(a)   (b)   (c)

(d)   (e)   (f)
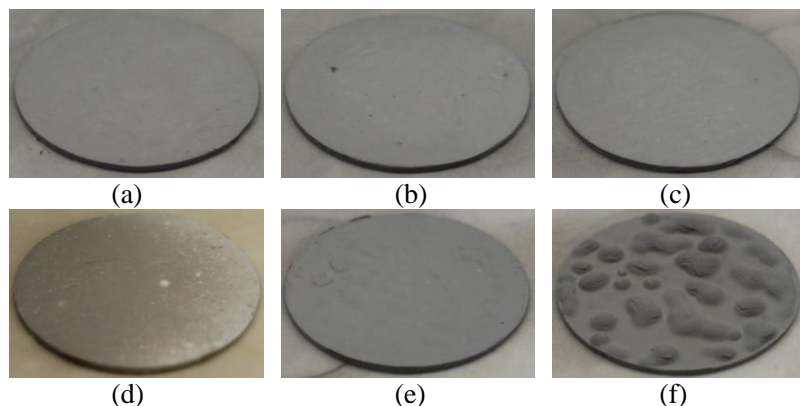
Figure 82 – Alumina discs after debinding process in forming gas atmosphere. Feedstocks have the following PW content: (a) 47.5, (b) 39, (c) 30, (d) 25, (e) 20 and (f) 0 (zero) vol.%.
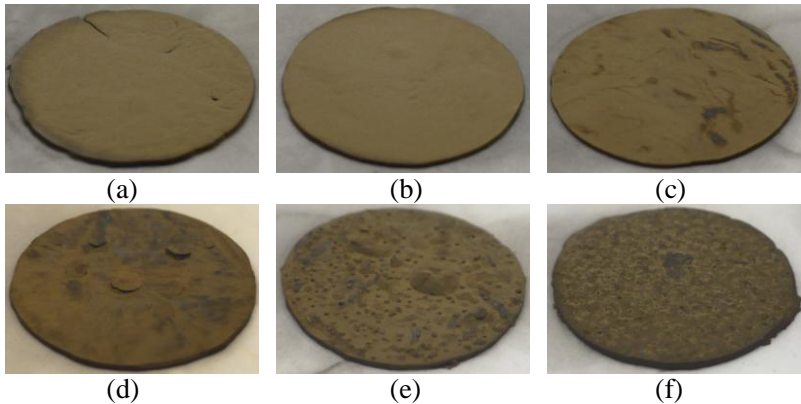
Figure 83 – IN718 discs after debinding process in forming gas atmosphere. Feedstocks have the following PW content: (a) 47.5, (b) 39, (c) 30, (d) 25, (e) 20 and (f) 0 (zero) vol.%.

4.3.3.   Ultimate extrusion feedstock

With the results of the two previous sections the extrusion feedstock was defined to be as shown graphically in Figure 84. For the ultimate extrusion feedstocks 30 vol.% of Nextel™ 610 fibers were incorporated in the solids content.
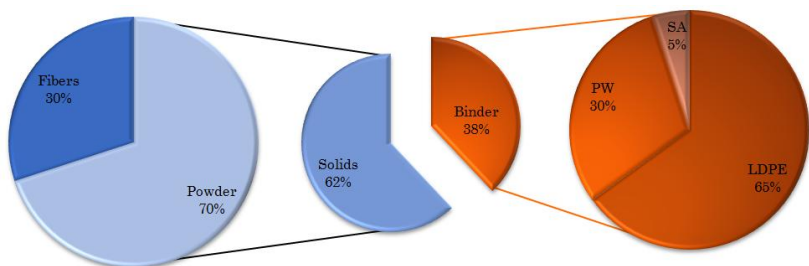
Figure 84 – Schematic graphic representing the ultimate extrusion feedstock composition.

4.3.3.1.   Mixing

Figure 85 and Figure 86 show the pre-mixing torque of the ultimate alumina and IN718 feedstocks with Nextel™ fibers. For both feedstocks, the pre-mixing curves show a different behavior than previously observed for the feedstocks without fibers. This can be seen in the stabilization time that is much longer, with a torque decrease during almost all pre-mixing time. This is associated with fiber breaking during mixing, *i.e.* as the fibers break and have their average length decreased, the mixing torque decreases correspondently.

Figure 87 and Figure 88 compare the final mixing torque of the feedstocks with and without fibers, for alumina and IN718 feedstocks, respectively. The compared feedstocks have the same binder system, *i.e.* 65 vol.% of LDPE, 30 vol.% of PW and 5 vol.% of SA. As expected, the feedstocks with fibers show higher mixing torque than their correspondent feedstocks without fibers. Nevertheless this effect was more evident for the IN718 feedstocks, for which the mixing torque has almost doubled and remained higher after mixing for 40 minutes.

For the alumina feedstock, the mixing torque started higher, however, fiber breakage has still occurred during final mixing, leading to a torque decrease until the end of mixing. In the end the mixing torque of the alumina feedstocks with and without fibers were nearly the same. It seems that the particle-particle friction and particle-fiber friction are of the same magnitude when the fibers break to shorter lengths. This effect that is observed for the alumina feedstock but not for the IN718 feedstock may be related with the powder composition, but also with the powder morphology and particle size distribution, which are all different comparing both powders.

Nevertheless it should be also emphasized that the mixing torque of the feedstock without fiber has also shown an unusual increase of mixing torque during the last minutes, what cannot be clearly explained and this contributes to the equalization of torque for the feedstocks with and without fibers. Normally a feedstock should show a thixotropic behavior (GERMAN, 1990), *i.e.* exhibits a decrease in shear stress with time at constant shear rate, but in this case a rheopectic behavior has been observed.
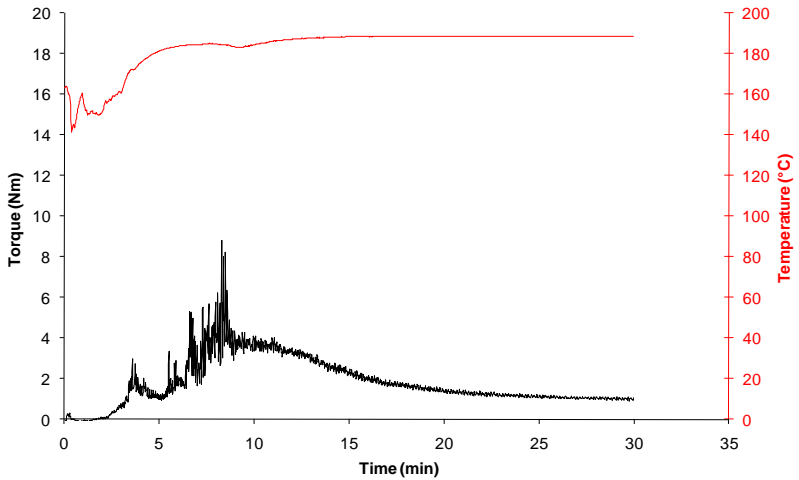
Figure 85 – Plot of pre-mixing torque and pre-mixing temperature versus time of the ultimate alumina feedstock with Nextel™ fibers.
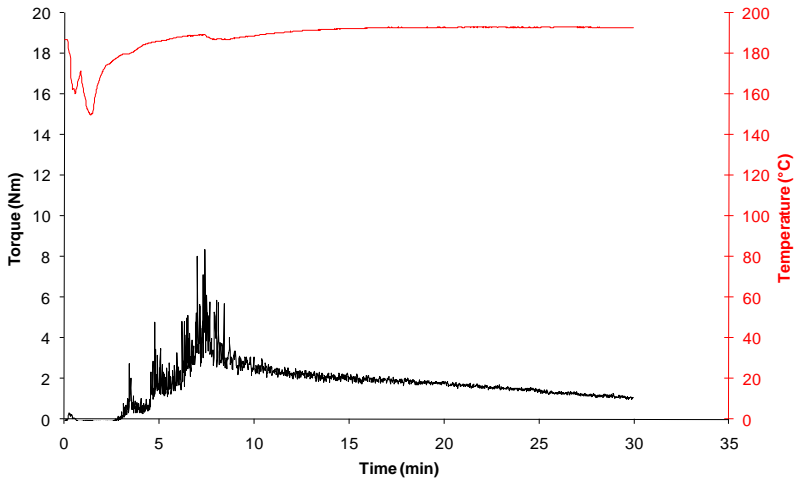
Figure 86 – Plot of pre-mixing torque and pre-mixing temperature versus time of the ultimate IN718 feedstock with Nextel™ fibers.
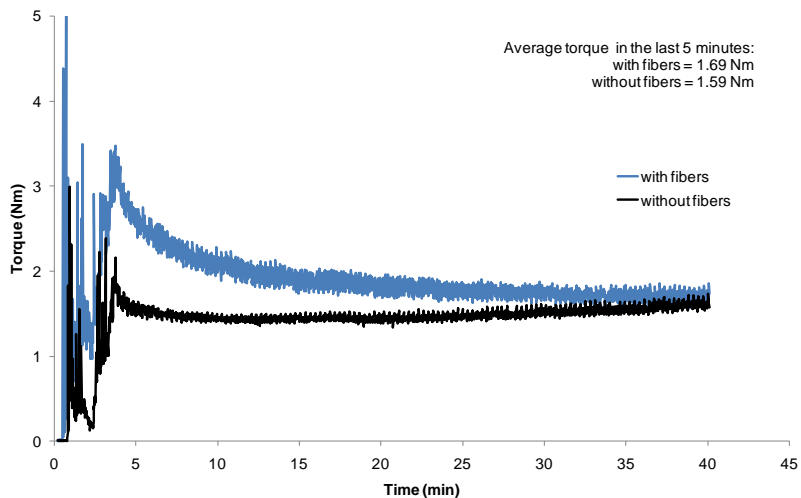
Figure 87 – Plot of final mixing torque versus time of the ultimate alumina feedstock with Nextel™ fibers in comparison with the correspondent alumina feedstock without fibers.
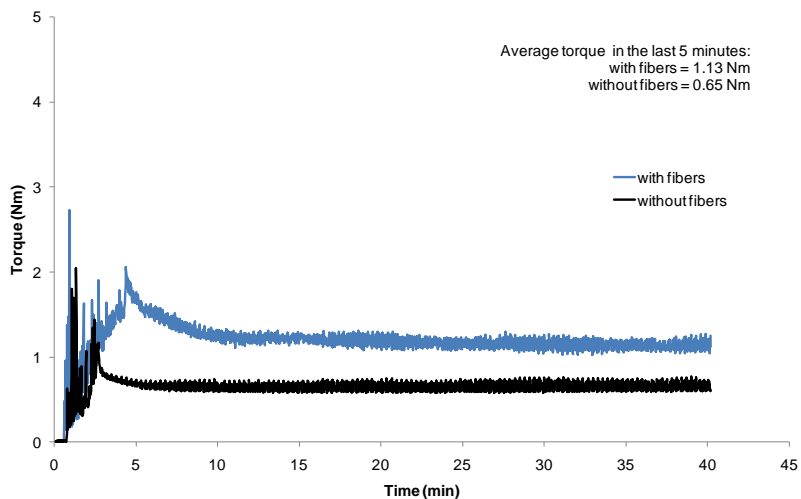
Figure 88 – Plot of final mixing torque versus time of the ultimate IN718 feedstock with Nextel™ fibers in comparison with the correspondent IN718 feedstock without fibers.

Figure 89 and Figure 90 show the TGA results of the ultimate alumina and IN718 feedstocks with fibers. The analyses were performed in forming gas atmosphere, from room temperature up to 600 °C, with a heating rate of 5 °C/min. Both curves, for alumina and IN718 powders, are nearly the same showing no influence of the different powders on the kinetics of binder thermal extraction. The low molecular weight binders, SA and PW, were extracted before, at the temperature range from 200 to 300 °C. As the extraction temperature range of both SA and PW are nearly the same, no separation of the extraction peaks was noticeable, which means that they were extracted simultaneously. The remaining binder, LDPE, that correspond to 65.46 wt.% was extracted at temperatures above 400 °C.
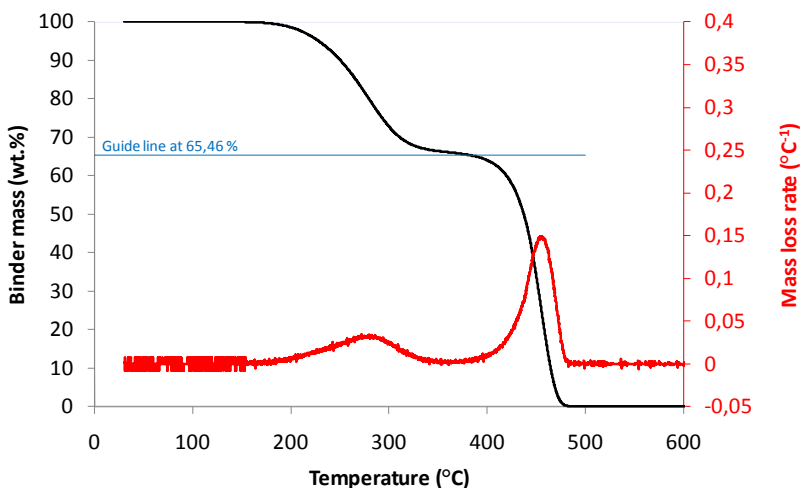
Figure 89 – Thermogravimetric analysis of the ultimate alumina feedstock with Nextel™ fibers. Atmosphere: forming gas. Total mass has been normalized to binder mass to facilitate the interpretation of the curve. The guide line at 65,46 wt.% represents the LDPE amount that remains after the removal of SA and PW.

158
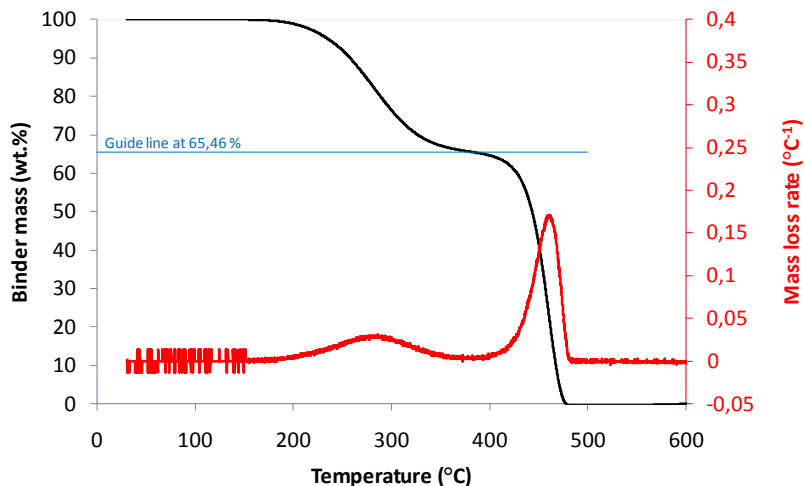
Figure 90 – Thermogravimetric analysis of the ultimate IN718 feedstock with Nextel™ fibers. Atmosphere: forming gas. Total mass has been normalized to binder mass to facilitate the interpretation of the curve. The guide line at 65,46 wt.% represents the LDPE amount that remains after the removal of SA and PW.

4.3.3.2.   Granulation

The attempt to granulate the feedstocks with fibers has not been successful. Fibers have clogged the narrow orifice of the granulation die, which had 1.0 mm of diameter. Thus rough chopped feedstock has been used for the warm-pressing of discs.

4.3.3.3.   Warm-pressing

Table 22 shows the characteristics of warm-pressed discs of alumina and IN718 feedstocks with fibers. Pressing temperatures were the same used for the correspondent feedstocks without fibers. As it can be seen, the fiber content has not interfered negatively in the pressing process, allowing high densities to be achieved. The theoretical density

was for the ultimate feedstock was also calculated with the densities and volumes of particles, fibers and binders used to produce the feedstocks, considering a total absence of voids

Table 22 – Density, thickness and pressing temperature of warm-pressed alumina and IN718 discs with the ultimate feedstocks containing fibers.

Powder	Pressing temperature (°C)	Density (g/cm³)	Theoretical density (g/cm³)	Percentage of theoretical density (%)	Thickness (mm)
Alumina	120	2.828	2.8081	100.71	0.74
IN718	115	4.629	4.6205	100.18	0.78

4.3.3.4. Debinding

The warm-pressed samples have been submitted to the basic debinding program in forming gas atmosphere. The program successfully removed 95.10 % and 96.95 % of the binder for the IN718 and alumina samples, respectively. The remaining binder is expected to be carburized at higher temperatures during the sintering step. Figure 91 shows the pictures of the samples after the debinding process. Again no blisters, deformation or edge rounding have been observed. Such result indicates that the fibers do not play a significant role in the debinding mechanism.

(a)   (b)
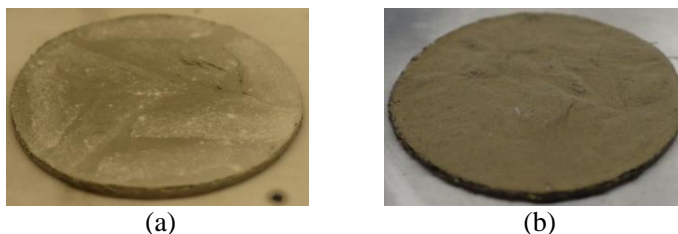
Figure 91 – Discs after debinding process in forming gas atmosphere. (a) Alumina and (b) IN718 ultimate feedstocks with fibers.

160

4.4.   TUBES EXTRUSION

The extrusion of tubes has been performed with the ultimate alumina and IN718 feedstocks developed and showed in the previous sections. The following sections describe the approach to achieve uniform and visually defect-free tubes produced via extrusion. As mentioned before, extrusion was carried out in a capillary rheometer adapted with tube extruding dies in three different configurations, allowing the production of three different tube geometries.

As the extrusion equipment was relatively simply built, only two parameters could be controlled, namely cylinder temperature and piston speed. A third parameter, die temperature, has also been investigated, however, no electronic automated control was originally built in the machine, and a cooling setup with the use of a refrigerant fluid, has been adapted, which has given the die temperature two states, cooled and not cooled. The control of these three parameters, which is going to be discussed in the following sections, was the most important aspect on the extrusion optimization, and has been done mainly in an empirical way.

4.4.1.   Cylinder temperature control

The cylinder temperature has been set in six different temperatures: 90, 95, 100, 110, 120 and 140 °C. Considering the melting point of the high molecular polymer, LDPE70, that is 108 °C, the temperature varied from below to above the melting point of this polymer, which is the backbone of the system. Thus the tubes were extruded in the solid and molten states. The solid state extrusion is of industrial practice and is only possible with plunger type extruders (RAUWENDAAL, 1986), with a configuration similar to the adapted capillary rheometer used in the present work.

With this temperature variation, differences were expected on the surface finishing of the tubes, as well as some deformation and, of course, differences on extruding pressures. During the control of cylinder temperature, no die cooling has been applied and the piston speed was fixed at 1.0 mm/min.

The first aspect noticed was that there was no possibility to extrude the tubes at 140 °C. The viscosity of the feedstock in the exit of

the die was so low at such high temperature, that the tubes were collapsing, and any attempt to improve the process, reducing for example the extruding speed, was useless. So without controlling the die temperature, extrusion was only possible at low temperatures, close to the melting point of the backbone.

The second aspect observed was that the cylinder temperature affects tremendously the extrusion pressure. Figure 92 shows the influence of cylinder temperature on extruding pressure for alumina tubes with 10.0 mm of diameter and 0.6 mm of wall thickness, with piston speed of 1.00 mm/min. The figure shows that the pressure decreases drastically with increasing temperatures. Very low pressures, below 1.0 MPa, could be achieved at temperatures above the melting point of the backbone polymer. The low pressures reflect the very low viscosity of the feedstock at such temperatures, which makes difficult the maintenance of extrudate shape once it exits the die. Moreover low pressures imply low shear rates that could possibly not be sufficient to align the fibers properly.

Figure 92 – Plot of extrusion pressure versus cylinder temperature of alumina tubes with 10.0 mm of diameter and 0.6 mm of wall thickness. Piston speed: 1.00 mm/min.

Making use of Equation 5 and adjusting the activation energy E, it was possible to fit the curve generated by the equation with the experimental data in the Arrhenius plot of Figure 93. The equation

correlates viscosity with temperature, however, it fitted quite well the experimental data, which correlates extrusion pressure with temperature. The activation energy of the feedstock, also shown in Figure 93, was much higher than that of the plain binder, which are 4.4 kJ/mol for PW and 19.0 kJ/mol for PE (GERMAN, 1990). This is because of the difference in the thermal expansion of the binders and particles, which makes the feedstock much more thermal sensitive than the unfilled binders (GERMAN, 1990).
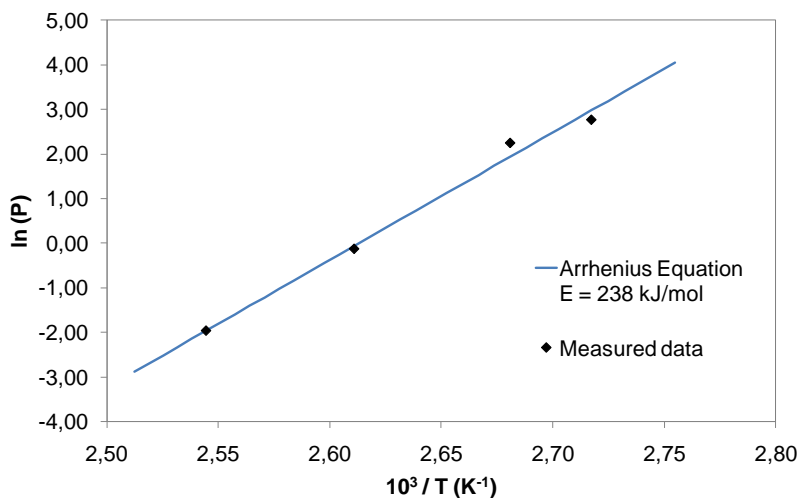
Figure 93 – Arrhenius plot of the natural logarithm of extrusion pressure *P* versus the inverse of extrusion temperature *T*. The measured data are from the extrusion of alumina tubes with 10.0 mm of diameter and 0.6 mm of wall thickness with a piston speed of 1.00 mm/min.

Extruding temperature also showed to be an important parameter regarding the surface visual aspect of the tubes. Temperatures above 120 °C, which is above the melting point of the backbone, have yielded tubes with *rough surface* and *banana shape* (warping). Figure 94 shows examples of tubes extruded at high temperatures with such defects.

<center>(a)   (b)</center>
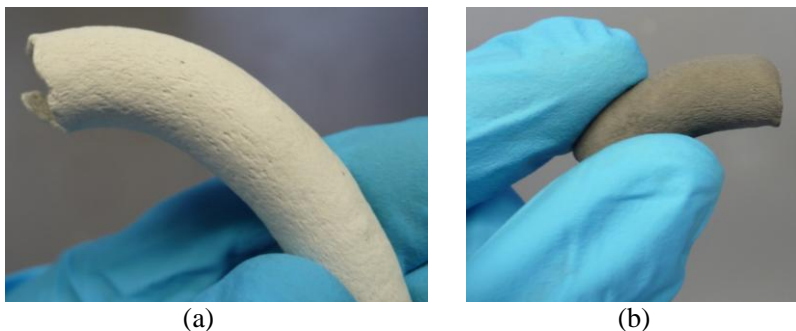
Figure 94 – Picture of extruded tubes with surface defect associated with extrusion above the melting point of the backbone polymer. (a) Alumina tube extruded at 120 °C and (b) IN718 tube extruded at 120 °C showing both rough surface and banana shape. The tubes were extruded with a piston speed of 1.00 mm/min, with no die temperature control.

On the other hand, extrusion at temperatures below or close to the melting point of the backbone resulted in tubes with polished surface, however with two other surface defects: (a) *fish scale*, also known as *bamboo* (RAUWENDAAL, 1986), and (b) *stains*, which are similar to the surface defect known as *shark skin*, associated with both extrusion temperature and speed (RAUWENDAAL, 1986). Figure 95 show examples of these two defects proceeding from extrusion at low temperatures.

<center>(a)   (b)   (c)</center>
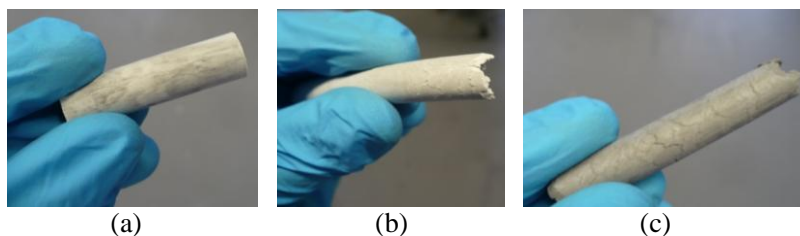
Figure 95 – Picture of extruded tubes with surface defect associated with extrusion below or close to the melting point of the backbone polymer. (a) Alumina tube extruded at 100 °C showing stains on the surface, (b) alumina tube extruded at 110 °C showing fish scale and (c) IN718 tube extruded at 110 °C showing also fish scale. The tubes were extruded with a piston speed of 1.00 mm/min, with no die temperature control.

4.4.2. Die temperature control

As already mentioned, the equipment used in this work had no die temperature control. Without any cooling, the die achieved roughly the same temperature of the cylinder. As showed in the previous section, no matter what temperature of the cylinder has been used, tubes with different defects have been produced and no defect-free product has been achieved this way.

To solve this problem, a refrigerant fluid has been used to cool down the die. For that, a beaker full of fluid was positioned right under the die exit, in a way that the refrigerant fluid was in permanent contact with the die, just as it is shown in Figure 96. Water and ethanol have been chosen as refrigerants, being the former used exclusively with alumina tubes and the latter for both alumina and IN718 tubes, to avoid oxidation of the nickel alloy in water.

(a)   (b)
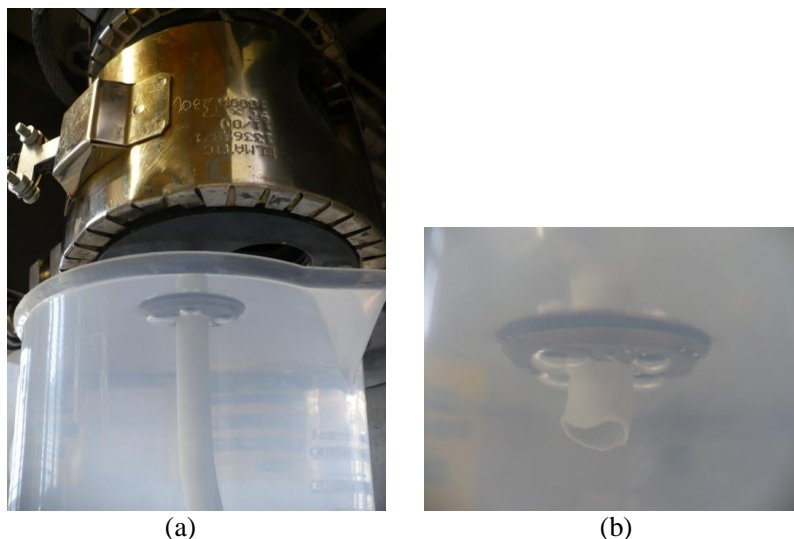
Figure 96 – Pictures of die cooling setup showing: (a) the refrigerant fluid (ethanol) inside the beaker in contact with the extrusion die to reduce its temperature; and (b) detail of the die submerged in the ethanol bath and the alumina extrudate exiting the die.

With this setup it was possible to cool the lower part of the die down to the boiling temperature of the chosen refrigerant fluid, *i.e.* 100

°C for water and 78 °C for ethanol. So what has been done was to set the cylinder to high temperature, *i.e.* above melting point of LDPE, and cool the die end with the refrigerant.

Although using the die cooling setup the die end could be kept at a temperature close to the boiling point of water or ethanol, the die entrance had still roughly the same temperature of the cylinder. This means that the feedstock was being shaped into the die in the molten state, and only in the very end of the die, where no more shape change was imposed to the feedstock, the extrudate was cooled down below the melting point of the backbone, but still inside the die. With this the surface finishing of the extrudate should be the same as the surface finishing of the die walls, in a process close to solid state extrusion, in which a much better surface quality is also attained (RAUWENDAAL, 1986). Moreover, an increase in pressure has been experienced with the use of the die cooling setup, related the higher friction between the solidified extrudate and the die walls. Higher pressures lead to a more compacted extruded structure, with higher particle contact, which increases the shape stability, especially during debinding and sintering. On the other hand a more compacted extruded structure may also have residual stresses that would be detrimental to shape maintenance during reheating.

The results seemed much better with the use of this setup, even allowing the temperature of the cylinder to be set as high as 140 °C, what was impracticable without cooling the die. Some results can be seen in Figure 97. The tubes produced without the use of the die cooling setup have a *rough surface* and show a *banana shape* deformation, defects that are solved with the use of the cooling setup.
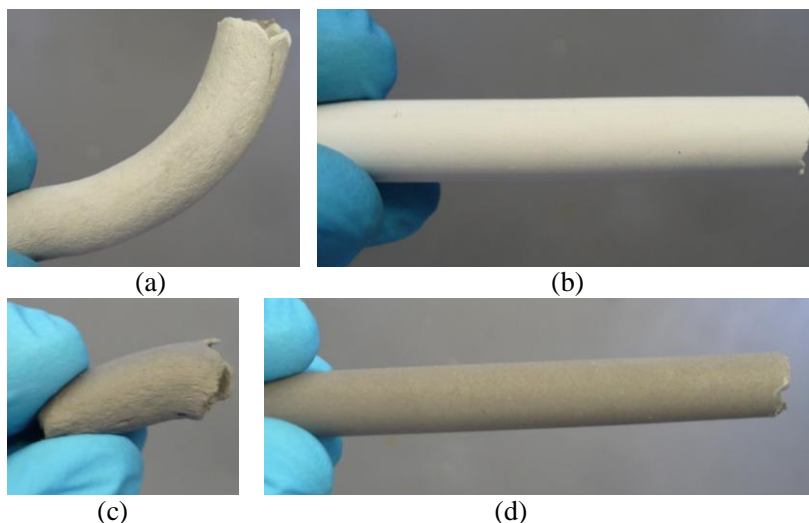
Figure 97 – Pictures of tubes produced without and with the setup for cooling the die. (a) Alumina tube extruded at 120 °C without die cooling setup. (b) Alumina tube extruded at 120 °C with die cooling setup, using ethanol as refrigerant. (c) IN718 tube extruded at 120 °C without die cooling setup. (d) IN718 tube extruded at 120 °C with die cooling setup, using ethanol as refrigerant. All tubes were extruded with a piston speed of 1.00 mm/min. All tubes have 10.0 mm of diameter and 1.0 mm of thickness.

4.4.3. Piston speed control

The influence of piston speed on extrusion pressure is shown on Figure 98. As it can be seen the pressure inside the cylinder increases more or less proportionally with the increase of piston speed until a piston speed of 2.00 mm/min. Above this speed the pressure seems not to increase relevantly, which may be related with the shear thinning behavior (pseudoplasticity) of the feedstock.
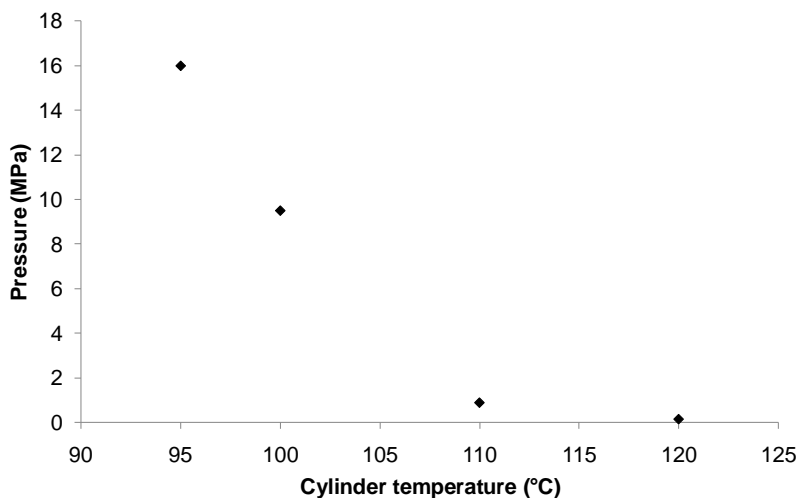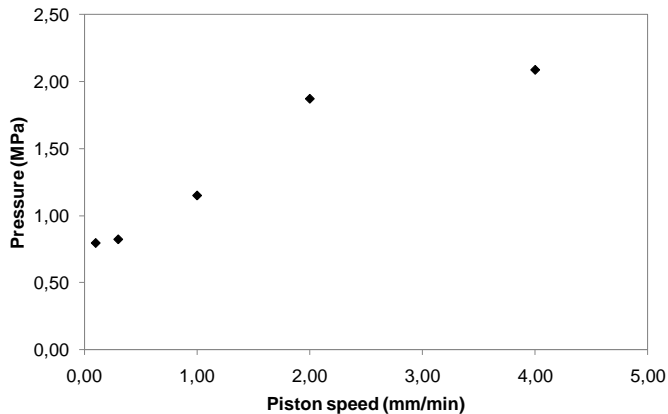
Figure 98 – Plot of extrusion pressure versus piston speed of IN718 tubes with 10.0 mm of diameter and 0.6 mm of wall thickness extruded at 120 °C using the die cooling setup with ethanol.

The influence of piston speed on the extrudate has shown to be on both surface finishing and shape maintenance. Extrusion speed is directly proportional to the piston speed. It was observed that the lower the extrusion speed, the better is the surface and lower is the curvature of the banana shape defect.

To make it clear, piston speed is the velocity with which the piston presses the feedstock against the die during the extrusion process. Piston speed is set by the operator and controlled automatically by the device. Extrusion speed is the velocity with which the feedstock is extruded, *i.e.* the velocity of tube production, and depends on the piston speed, piston section area and die section area. Larger die section areas allow higher volumes of material to be extruded, producing thus, for a certain piston speed, lower extrusion speeds. Smaller die section areas allow lower volumes of materials to be extruded, producing, for the same piston speed, higher extrusion speeds.

A simple geometric analysis was used to estimate the extrusion speed as a function of piston speed. No extrudate swell or viscoelastic behavior of the feedstock was included in the calculation, which gives only an approximate value as a reference.

The volume of feedstock displaced by the piston V_P depends on the piston speed v_P, piston section area A_P and time t, according to Equation 17.

168

Equation 17 $$V_P = v_P \cdot A_P \cdot t$$

In the same way, the extruded volume V_E depends on the extrusion speed v_E, die section area A_D and time t, according to Equation 18.

Equation 18 $$V_E = v_E \cdot A_D \cdot t$$

But the extruded feedstock volume V_E is equivalent to the feedstock volume displaced by the piston V_P:

Equation 19 $$V_E \cong V_P$$

So, substituting Equation 17 on Equation 18:

Equation 20 $$v_E \cdot A_D \cdot t \cong v_P \cdot A_P \cdot t$$

Then v_E is given by:

Equation 21 $$v_E \cong \frac{v_P \cdot A_P}{A_D}$$

Equation 21 shows that the extrusion speed v_E is directly proportional to the piston speed v_P and inversely proportional to the die section area A_D. The calculated section areas of the piston and the dies are given in Table 23.

Table 23 – Calculated section areas of the piston and dies.

Nominal die diameter (mm)	Nominal die thickness (mm)	Real die diameter (mm)	Real die thickness (mm)	Die section area A_D (mm²)	Piston diameter (mm)	Piston section area A_P (mm²)
10.0	1.0	10.00	1.03	**28.9**		
10.0	0.6	10.00	0.60	**17.7**	24.00	**452.4**
4.5	1.0	4.53	1.03	**11.4**		

For the quality of the extrudate, what really matters is the extrudate speed v_E. With a piston speed v_P of 1.00 mm/min it was possible to produce defect-free tubes with the die of 10.0 mm of diameter and 1.0 mm of thickness, as shown before in Figure 97. However, using the same piston speed for the other two dies, *fish scale* and *banana shape* defects were evident on the tubes, as it can be seen in Figure 99.

(a)

(b)

(c)

(d)
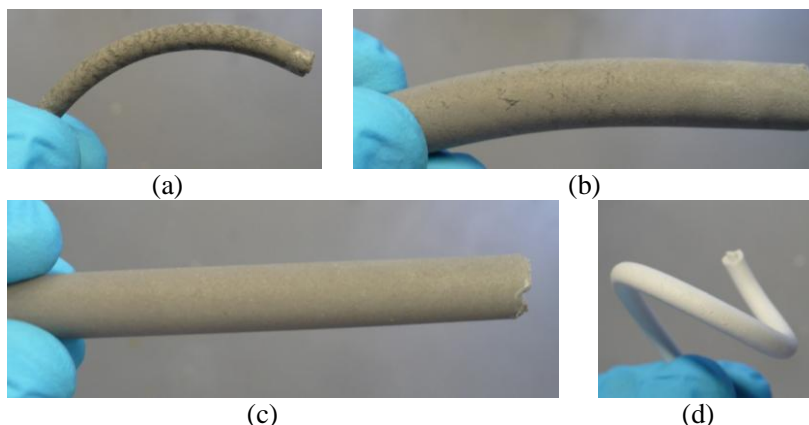
Figure 99 – Picture of tubes extruded with piston speed of 1.00 mm/min. (a) IN718 tube with 4.5 mm of diameter and 1.0 mm of thickness showing fish scale and banana shape. (b) IN718 tube with 10.0 mm of diameter and 0.6 mm of thickness showing fish scale and banana shape. (c) Defect-free IN718 tube with 10.0 mm of diameter and 1.0 mm of thickness. (d) Alumina tube with 4.5 mm of diameter and 1.0 mm of thickness showing fish scale and banana shape. All tubes were produced with the use of the die cooling setup with ethanol as refrigerant.

The defects shown in Figure 99 (a), (b) and (d) were produced due to the high extrusion speed imposed to the tubes. Applying Equation 21 the extrusion speed v_E is calculated for the three different dies geometries, using a piston speed v_P of 1.00 mm/min. The results are shown in Table 24.

Table 24 – Calculated extrusion speeds v_E for the three different dies geometries for a piston speed v_P of 1.00 mm/min.

Die diameter (mm)	Die thickness (mm)	v_P (mm/min)	v_E (mm/min)
10.0	1.0	1.00	**15.7**
10.0	0.6	1.00	**25.5**
4.5	1.0	1.00	**39.7**

As defect-free tubes could be produced with a v_E of 15.7 mm/min for the die of 10.0 mm of diameter and 1.0 mm of thickness, it was expected to produce defect-free tubes also with the other two dies at the same v_E. Table 25 shows the calculated v_P for the dies to produce a v_E of 15.7 mm/min.

Table 25 – Calculated piston speed v_P for the three different dies geometries to achieve an extrusion speed v_E of 15.7 mm/min.

Die diameter (mm)	Die thickness (mm)	v_P (mm/min)	v_E (mm/min)
10.0	1.0	**1.00**	15.7
10.0	0.6	**0.61**	15.7
4.5	1.0	**0.39**	15.7

Extruding tubes with any of the three dies using up to a maximum extrusion speed v_E of around 15.7 mm/min has yielded defect-free tubes as can be seen in Figure 100.

(a)   (b)

(c)   (d)

(e)   (f)
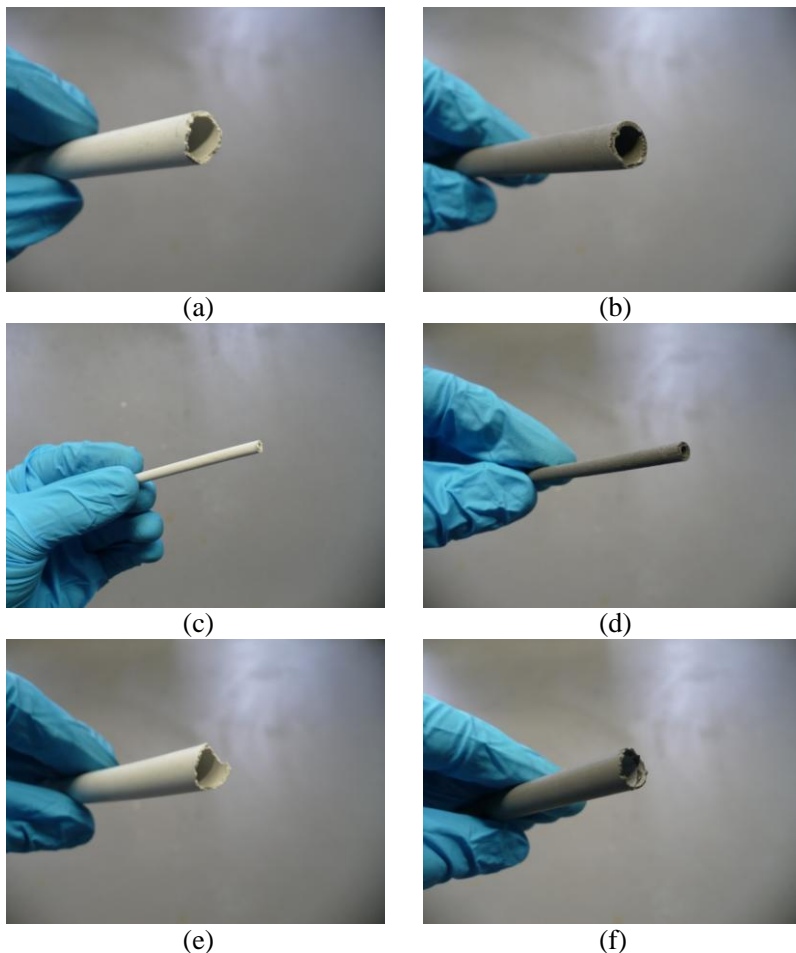
Figure 100 – Pictures of defect-free tubes extruded with extrusion speed v_E of 15.7 mm/min. (a) Alumina and (b) IN718 tubes with 10.0 mm of diameter and 1.0 mm of thickness. (c) Alumina and (d) IN718 tubes with 4.5 mm of diameter and 1.0 mm of thickness. (e) Alumina and (f) IN718 tubes with 10.0 mm of diameter and 1.0 mm of thickness. All tubes extruded at 120 °C using the die cooling setup with ethanol.

4.4.4. Ultimate extrusion conditions

After several extrusion trials, to study the control of the parameters described in the three previous sub-sections, the ultimate extrusion conditions have been defined as follows:

    i.   *Cylinder temperature* – 120 °C;

    ii.   *Die temperature* – using the die cooling setup with ethanol;
        a. *Die entrance* – 120 °C (cylinder set temperature);
        b. *Die exit* – 78 °C (ethanol boiling point);

    iii.   *Extrusion speed* – 15.7 mm/min;
        a. *Die of 10.0 mm of diameter and 1.0 mm of thickness* – Piston speed of 1.00 mm/min required;
        b. *Die of 10.0 mm of diameter and 0.6 mm of thickness* – Piston speed of 0.61 mm/min required;
        c. *Die of 4.5 mm of diameter and 1.0 mm of thickness* – Piston speed of 0.39 mm/min required;

Figure 101 show the tubes produced under the above ultimate extrusion parameters. It can be seen that tubes with high length/diameter ratio could be extruded. Tubes longer than 15 cm were not produced due to mere limitation of the ethanol beaker height.
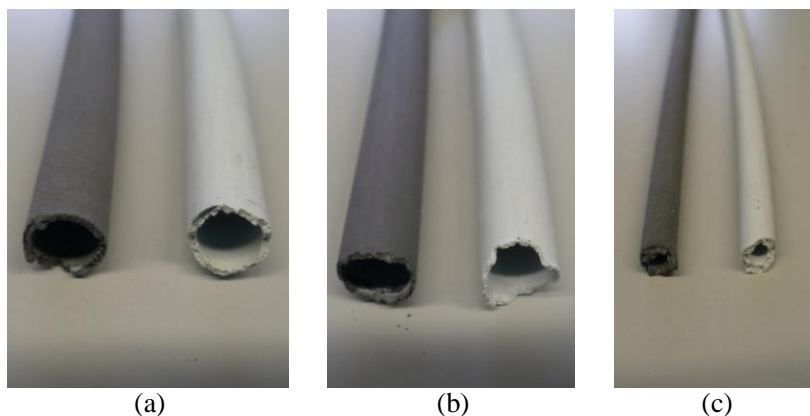
Figure 101 – Pictures of defect-free tubes extruded under the ultimate extrusion conditions. (a) IN718 [gray] and alumina [white] tubes with 10.0 mm of diameter and 1.0 mm of thickness. (b) IN718 [gray] and alumina [white] tubes with 10.0 mm of diameter and 0.6 mm of thickness. (c) IN718 [gray] and alumina [white] tubes with 4.5 mm of diameter and 1.0 mm of thickness.

No extruded tube showed the effect of extrudate swell. According to what could be found in the literature, the reasons for this phenomenon not to occur are the following:

  i. *Low die-end temperature* – as the die end is at a temperature below the melting point of the backbone, which is the main binder of the system, its molecules are already with too low mobility by the time the extrudate leaves the die. This is what happens in solid state extrusion, which also shows virtually no extrudate swell (RAUWENDAAL, 1986).

  ii. *Low extrusion speed* – molecular alignment is associated with high shear rates, which on its turn happens under high extrusion speeds. With low degree of alignment of the molecules, a lower elastic recover shall occur (CHEREMISINOFF, 1987). Moreover, even if the molecules could have been sufficiently aligned, the long residence time inside the die avoided the elastic recover that is time-dependent and can only occur after a limited time subsequent to the undergone deformation (RAUWENDAAL, 1986).

    iii.   *Low molecular weight binders* – the considerable amount of PW and SA, which are binders with short chains, must have diminished the amount of extrudate swell which is proportional to molecule length (CHEREMISINOFF, 1987).

    iv.   *Nextel™ fibers content* – the alumina fibers, which have a relative high rigidity, could have also worked as anchors, refraining the elastic recover.

Figure 102 and Figure 103 show the SEM images of the longitudinal section of the alumina and IN718 green tubes, respectively. In the images, it can be seen the good fiber alignment of the Nextel™ fibers in the direction of extrusion. This evidence shows that the shear rate was high enough to produce fiber alignment, although it was not sufficient to align the molecules.

(a)   Extrusion direction →   (b)
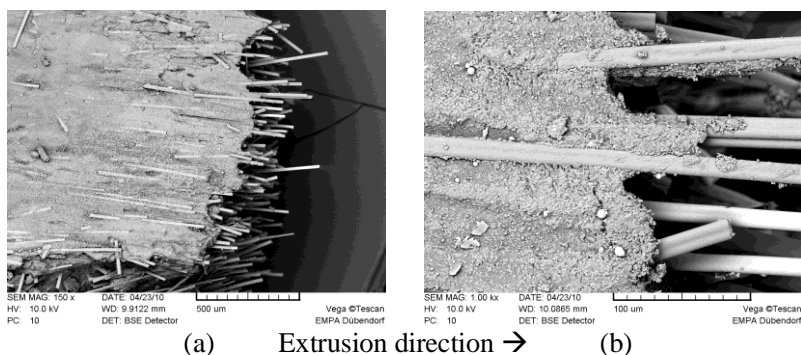
Figure 102 – SEM image of extruded alumina green tube. The images are from a tube with 10.0 mm of diameter and 1.0 mm of thickness. Magnification: (a) 150x and (b) 1000x.

A good distribution of particles along both the longitudinal and transversal sections can be seen, which indicates low level of agglomeration or segregation. The samples have been broken transversally, to avoid fiber cutting that would happen using any cutting instrument. In Figure 103b, it can be seen the original sites of fibers that have been pulled out during sample breakage. Note that at these sites some particles emerge from the binder, indicating that, before debinding, good particle-particle and particle-fiber contact already existed due to the high filling level used (62 vol.%). Another important

fact observed in the SEM images is that the fibers, once 30 mm long, have been broken during kneading down to lengths of approximately 0.5 mm.

(a)   Extrusion direction →   (b)
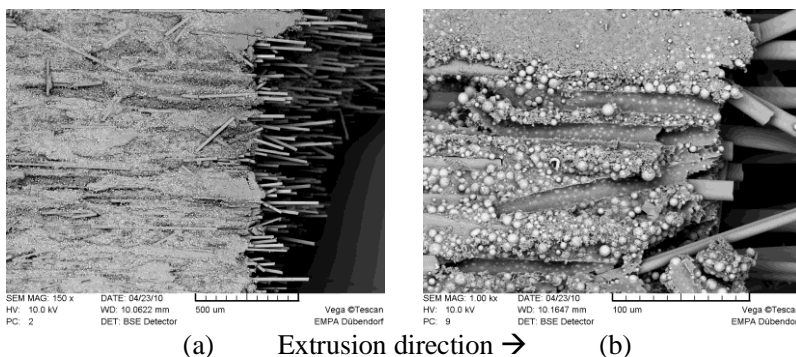
Figure 103 – SEM image of extruded IN718 green tube. The images are from a tube with 10.0 mm of diameter and 1.0 mm of thickness. Magnification: (a) 150x and (b) 1000x.

4.5.   TUBES DEBINDING AND SINTERING

In this section the steps of debinding and sintering were put together for a reason. With the disc-shaped samples it was noticed that, after debinding at 600 °C, the green strength of the samples was too low for any handling. Every attempt to handle the samples and remove them from the alumina support has resulted on sample fracture. Thus, to avoid any tube fracture, all the samples have been sintered directly after thermal debinding.

The sintering program for all samples was from 600 to 1300 °C, with a heating rate of 5 °C/min and a dwell time of 60 min at 1300 °C.

4.5.1.   Thermal debinding and sintering without previous solvent debinding

As the warm-pressed discs have presented good results with fully thermal debinding, the first approach for tube debinding was a simple

thermal cycle. So just like the warm-pressed samples, the tubes were submitted to the basic thermal debinding program and subsequently sintered at 1300 °C in forming gas atmosphere.

The thermal debinding and sintering program has successfully removed 100.47 ± 3.31% of the binder of the alumina tubes[10]. In the case of IN718 tubes, a mass gain apparently due to oxidation, carburization or even nitriding, has disguised the effect of binder removal, so that the calculated binder removal by weight loss was only of 59.95 ± 6.18%, which might not be true and a value close to 100% would be the reality. The hypothesis of oxidation is going to be discussed further on.

(a)   (b)   (c)

Figure 104 – Picture of alumina tubes after thermal debinding and sintering in forming gas. (a) Two samples of 10.0 mm of diameter and 1.0 mm of thickness; (b) Two samples of 10.0 mm of diameter and 0.6 mm of thickness and (c) One sample of 4.5 mm of diameter and 1.0 mm of thickness.

(a)   (b)

Figure 105 – Pictures of IN718 tubes after thermal debinding and sintering in forming gas. Tubes geometry: (a) 10.0 mm of diameter and 1.0 mm of thickness and (b) 4.5 mm of diameter and 1.0 mm of thickness.

---

[10] The maximum expected value of binder removal was 100.00%, however, due to error associated with weighting and sample mass loss on handling, this value can exceed 100.00%.

Figure 104 and Figure 105 show pictures of tubes after the debinding and sintering programs. All samples have undergone unacceptable deformation. The IN718 tubes have undergone the most severe deformation, collapsing completely.

Alumina tubes were also submitted to thermal debinding and sintering in air. But the results were not better, as it can be seen in Figure 106. The measured binder removal in this case was 98.11 ± 0.90%. Again the tubes have undergone deformation, except the tube with 4.5 mm of diameter (c), that seemed to have undergone no deformation. Nevertheless these results were unacceptable and to solve the problem a solvent debinding step was proposed.

<div align="center">(a)   (b)   (c)</div>

Figure 106 - Picture of alumina tubes after thermal debinding and sintering in air. (a) 10.0 mm of diameter and 1.0 mm of thickness; (b) 10.0 mm of diameter and 0.6 mm of thickness and (c) 4.5 mm of diameter and 1.0 mm of thickness. The dark edges of tubes (a) and (b) are contamination originated from the cutting disc. The curvature of the tube (c) is not related with the debinding and sintering, but was already present on the green tube.

4.5.2. Solvent debinding followed by thermal debinding and sintering

In order to diminish the deformation during thermal debinding, the samples were submitted to a cycle of solvent debinding. Ethanol heated at 60 °C was used as solvent. The samples were submerged in ethanol bath for 5 hours. Solvent debinding was able to remove 90.96 ± 4.35 % and 92.44 ± 3.17 % of the low molecular weight binders of the alumina and IN718 tubes, respectively.

Samples of the tubes after solvent debinding were analyzed via SEM. The comparative images are shown in Figure 107 and Figure 108.

The microstructure of the alumina tubes after solvent debinding did not have significant alterations, except some channels that seem to have appeared after solvent debinding, but are somewhat confused with some cracks originated during the transversal breakage of the sample. On the other hand, for the IN718 tubes, a noticeable difference on the microstructure is evident and a more porous structure is observed after solvent debinding. This shows that solvent debinding was fulfilling its role on letting a porous structure with channels, allowing the backbone polymer to be easily extracted by thermal evaporation/degradation.

(a)   (b)
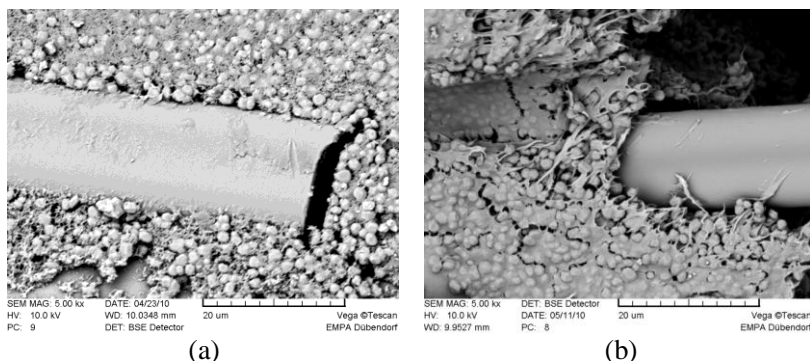
Figure 107 – SEM images of extruded alumina tubes (a) before solvent debinding and (b) after solvent debinding. Magnification: 5000x.

(a)   (b)
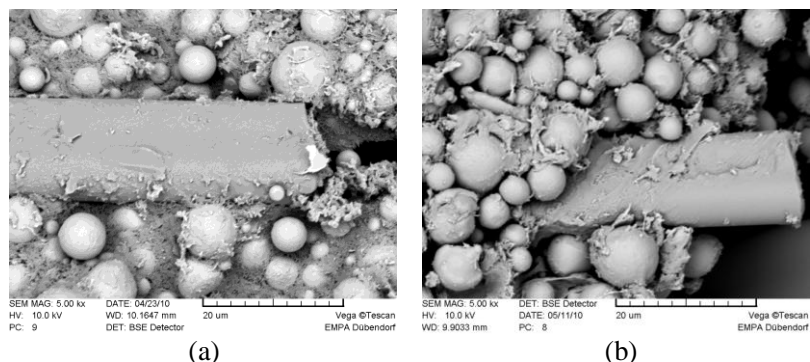
Figure 108 – SEM images of extruded IN718 tubes (a) before solvent debinding and (b) after solvent debinding. Magnification: 5000x.

After solvent debinding, the samples were submitted to thermal debinding and sintering the same way as in the previous section. The

alumina tubes submitted to thermal debinding and sintering in forming gas had 97.58 ± 2.30% of the binder removed. The IN718 tubes had again the same problem of weight gain previously discussed, most probably due to oxidation, carburization or nitriding, and the calculated value of binder removal, which might be false, was only 60.46 ± 4.02%. Alumina tubes were also submitted to thermal debinding and sintering under air atmosphere and had 100.22 ± 4.09% of the binder removed[11].

Figure 109 and Figure 110 show pictures of alumina and IN718 tubes after solvent debinding, thermal debinding and sintering in forming gas. Figure 111 shows pictures of alumina tubes after thermal debinding and sintering in air atmosphere. As it can be seen, solvent debinding was indeed helpful on avoiding deformation during thermal debinding. All the alumina tubes, submitted to thermal debinding and sintering, both in forming gas and air atmosphere have undergone no deformation.

In the case of the IN718 tubes, only the smallest tube, with 4.5 mm of diameter and 1.0 mm of thickness, has not deformed during thermal debinding and sintering. The tube with 10.0 mm diameter with thicker wall (1.0 mm thick) shows a much lower deformation comparing with the sample without solvent debinding, but still a certain amount of deformation is evident. The tube with thinner wall (0.6 mm thick) has deformed considerably more than the thicker one. In fact the sphericity of the IN718 particles, which is much higher than the alumina particles, makes the tubes of the former much more likely to undergo deformation during thermal debinding (GERMAN, 1990).

Another reason for the deformation during thermal debinding could be related with the too low evaporation/degradation temperature of the backbone (around 450 °C). At this temperature, virtually no neck was formed before the last LDPE molecules were removed. Efficient thermal debinding should allow the backbone to be removed at the onset of the sintering temperature of the powder, so that sintering necks would provide strength to the compact before the backbone is completely removed (GERMAN, 1990). Nevertheless this is only possible with low temperature metallic alloys. For refractory alloys, such as nickel superalloys, and ceramics, the onset of sintering temperature is far beyond the degradation temperature of the available polymers.

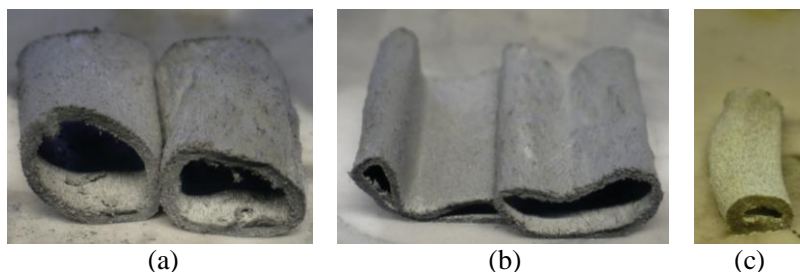[11] Idem note 10.

(a)   (b)   (c)
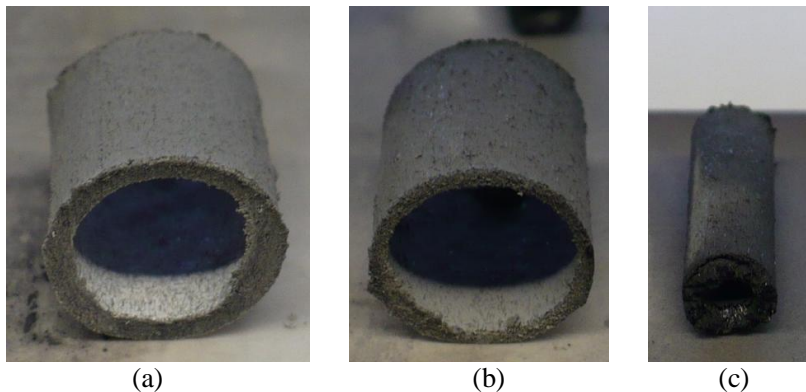
Figure 109 – Picture of alumina tubes after solvent debinding, thermal debinding and sintering in forming gas. (a) 10.0 mm of diameter and 1.0 mm of thickness; (b) 10.0 mm of diameter and 0.6 mm of thickness and (c) 4.5 mm of diameter and 1.0 mm of thickness.

(a)   (b)   (c)
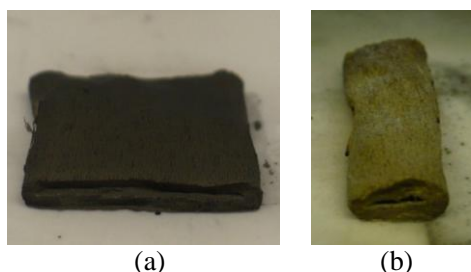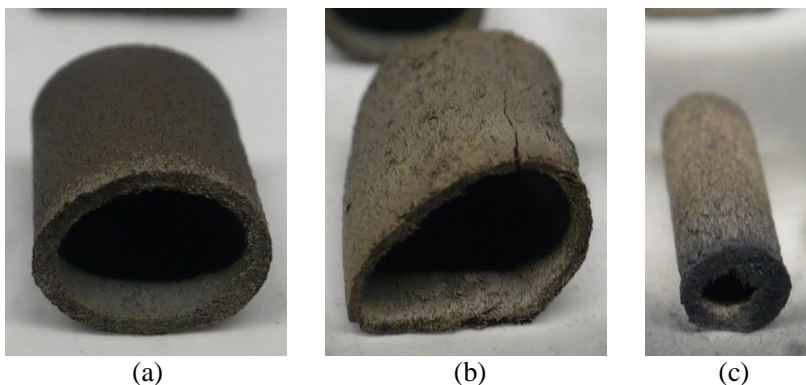
Figure 110 – Picture of IN718 tubes after solvent debinding, thermal debinding and sintering in forming gas. (a) 10.0 mm of diameter and 1.0 mm of thickness; (b) 10.0 mm of diameter and 0.6 mm of thickness and (c) 4.5 mm of diameter and 1.0 mm of thickness.
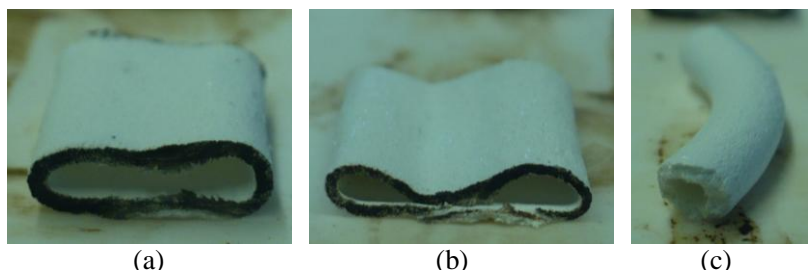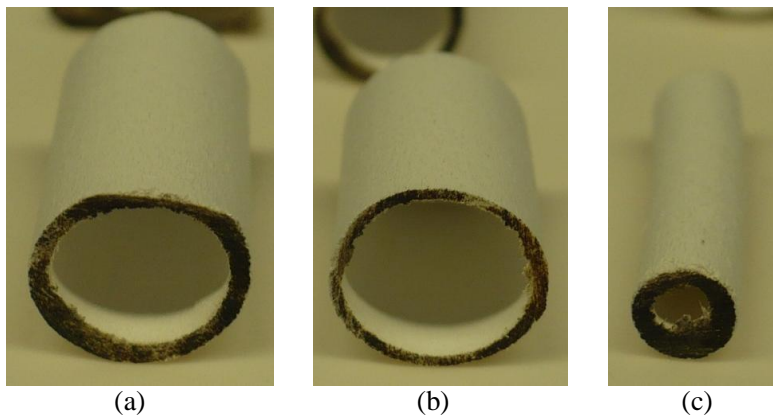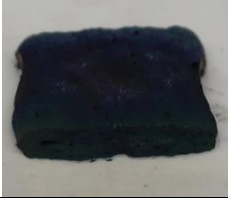
Figure 111 – Picture of alumina tubes after solvent debinding, thermal debinding and sintering in air. (a) 10.0 mm of diameter and 1.0 mm of thickness; (b) 10.0 mm of diameter and 0.6 mm of thickness and (c) 4.5 mm of diameter and 1.0 mm of thickness. The dark edges of the tubes are contamination originated from the cutting disc.

Some attempts have been made to diminish the deformation of IN718 tubes by means of changing the thermal debinding program. Faster heating rates trials have been made under the reasoning that holding the sample longer times above the melting point of the backbone would produce higher deformation. Besides, at higher heating rates, the binder removal should happen at higher temperatures, shifting the thermal debinding to temperatures closer to the onset of sintering, so that neck formation would increase the stability of the compact (GERMAN, 1990; GERMAN, 2005).

Table 26 shows the different programs tried and the picture of the samples after the tests. No program has succeeded. For test #3 the heating rate has been increased only on the beginning of the heating ramp, avoiding the unnecessarily long exposure time above the melting point of LDPE and below the extraction temperature range. Above 350 °C, when the LDPE started to be extracted, the heating rate was decreased to the standard 0.5 °C/min. This program has also failed, making it evident that a faster program would not help, and the deformation was increasing with the increase of heating rate. A slower heating rate could have solved the problem, but it was operationally impracticable.

Table 26 – Different thermal debinding programs used on the attempt to diminish the deformation of IN718 tubes with 10.0 mm of diameter and 1.0 of thickness. All samples have been previously submitted to solvent debinding.

#	Temperature (°C)	Dwell time (min)	Heating rate (°C/min)	Image
0	25-600	60	0.5	
1	25-600	60	1.0	
2	25-600	0	5.0	
3	25-350	0	5.0	
	350-600	60	0.5	

4.5.3.   Sintered tubes characterization

4.5.3.1.   SEM analysis

Figure 112 and Figure 113 show the SEM images of alumina and IN718 tubes after sintering at 1300 °C for 60 min. These tubes have 4.5 mm of diameter and 1.0 mm of thickness. At this sintering temperature and time, some sintering necks were expected on both alumina and IN718 particles. The necks on the alumina particles are not visible with this magnification, but they were presumably formed, as the resistance to fracture of the samples has increased considerably and were not breakable by hand. Analytical mechanical resistance tests were not performed due to lack of measurable samples. In the case of the IN718 sample, the necks are noticeable, though very small.

Sintering at 1300 °C for 60 minutes was not enough, as would suggest the literature (JOHNSON, et al., 2004; CALOW, et al., 1972), being necessary higher sintering temperatures or times to allow neck growth. It seems that no neck formation occurred between the particles and the fibers for both alumina and IN718 powders. Moreover the fibers might have refrained the shrinkage of the compact, and consequently avoided neck growth in both cases. Additionally, the oxidation of the nickel based powder also restrained sintering.

(a)   (b)
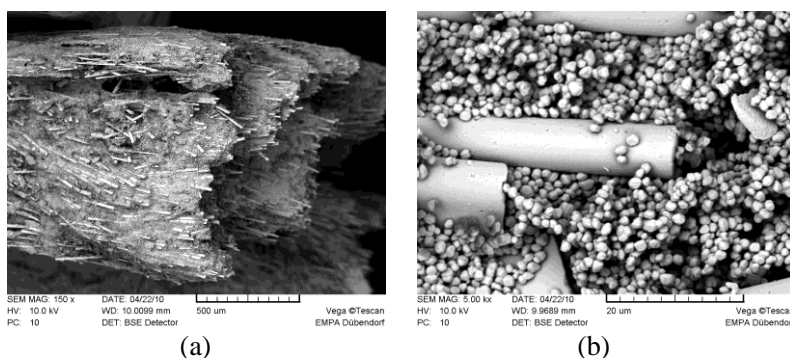
Figure 112 – SEM images of an alumina tube sintered in forming gas at 1300 °C for 60 min. Magnifications: (a) 150x and (b) 5000x.

184

SEM MAG: 150 x	SEM MAG: 5.00 kx
HV: 10.0 kV WD: 9.9988 mm 500 um Vega ©Tescan	HV: 10.0 kV WD: 10.0854 mm 20 um Vega ©Tescan
PC: 10 DET: BSE Detector EMPA Dübendorf	PC: 10 DET: BSE Detector EMPA Dübendorf

(a)   (b)
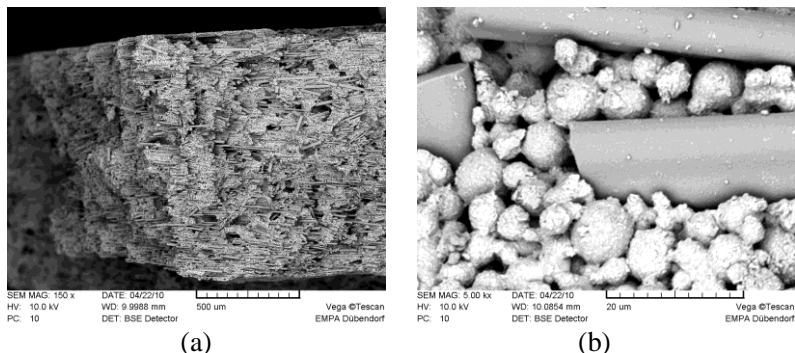
Figure 113 – SEM images of an IN718 tube sintered in forming gas at 1300 °C for 60 min. Magnifications: (a) 150x and (b) 5000x.

4.5.3.2. XRD analysis

Figure 114 shows the XRD analysis results of the sintered and green tubes of alumina. Peaks of alpha alumina crystal, originated from the alumina powder and Nextel™ fibers, were identified along with peaks of $(CH_2)_x$, originated from PW and LDPE of the binder. No significant difference was indentified between the three XRD patterns, excepting the peaks of $(CH_2)_x$ found in the green tube. It may also have occurred an increase in crystallinity of the sintered tubes in comparison with the green tube, which can be noticed on the slightly narrowing of the peaks on the sintered samples. However this difference can also be mere sampling error. No difference at all could be noticed between the tubes sintered in air and in forming gas.
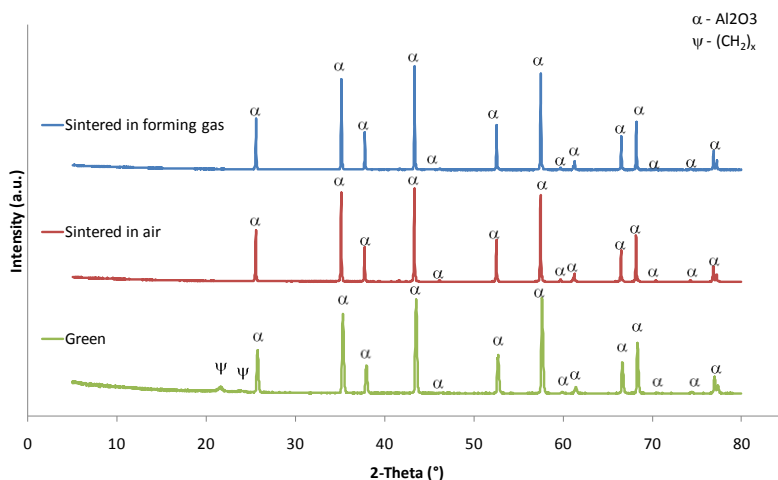
Figure 114 – XRD analyses of green and sintering alumina tubes. Sintering atmospheres: forming gas and air.

Figure 115 shows the XRD results for the green and sintered IN718 tubes. On the green sample peaks of alpha alumina crystals, originated from the Nextel fibers, were identified along with peaks of FeNi alloy, originated from the IN718 powder and related with the two main elements of the alloy. Not surprisingly, on the sintered XRD pattern two other peaks were identified, chromium nitride (Cr_2N) and iron oxide ($Fe_{0.902}O$). The abundant nitrogen from the forming gas atmosphere reacted with chromium, which is one of the most important alloying element (18.5%) of the IN718 nickel superalloy; the reaction product was stable chromium nitride. On the same way, oxygen contamination in the atmosphere has oxidized iron, the most abundant alloying element of IN718 (18.9%). The oxygen may have been adsorbed on the walls of the furnace. Oxygen may also have entered the furnace during sintering, because the sealing of the furnace was not efficient, and gaps were sometimes detected.

The spinel phase ($NiAl_2O_4$), expected to be formed in the alumina and IN718 interfaces (CALOW, et al., 1971; SURESH, et al., 1993; MILEIKO, 1997; MILEIKO, et al., 2002a), has not been detected in the XRD analysis.

186
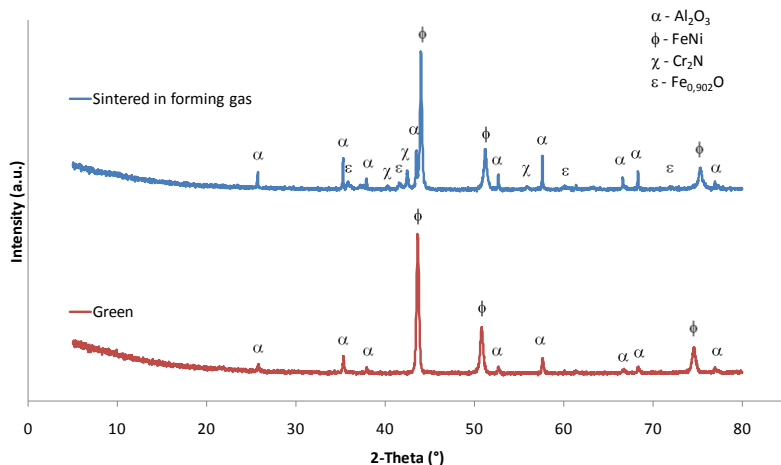
Figure 115 – XRD analysis of green and sintered IN718 tubes. Sintering atmosphere: forming gas.

In order to investigate the influence of the alumina fibers on the sintering of IN718 based tubes, a sample of IN718 without fiber has also been analyzed by XRD after sintering. The comparative results are shown in Figure 116. Niobium and Niobium carbide (NbC) peaks have been identified in the sample without fibers, showing that carburizing was also another effect on the sintering conditions of the present work. Niobium is another important alloying element of the superalloy (5.0%) and reacted with carbon proceeding from the binders. Carburizing was indeed occurring and the alumina support and the alumina tube of the furnace have been clearly carburized, after every thermal debinding and sintering run, showing a typical graphitic color. The carbon on the alumina support and alumina tube of the furnace is an evidence that the atmosphere was rich in carbon during thermal debinding, and a higher gas flow should be helpful to decrease the atmosphere carbon content (GERMAN, 1990). Thus the carbon, which formed the carbide found in the XRD analysis, can be originated from the atmosphere that was rich in carbon after thermal debinding or, eventually, from residual carbon that is likely to happen for low heating rates and in cases where the binders are removed above 450 °C (GERMAN, 1990).

Apart from the different compounds formed, no difference on the characteristic peaks of the nickel superalloy has been identified. The

different carbides, oxides and nitrides formed seem more to be sampling difference and might not have any relationship with the presence or not of alumina fibers during sintering. So far no literature was found reporting the influence of alumina in nickel superalloys on compound formation.
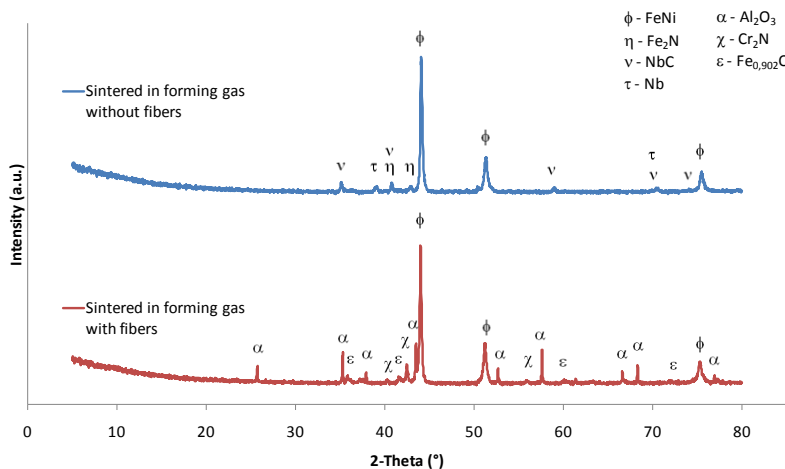
Figure 116 – XRD analysis of sintered IN718 samples with and without Nextel™ fibers. Sintering atmosphere: forming gas

The oxides, nitrides and carbides found in the IN718 samples explain the weight gain discussed previously that have disguised the mass loss during binder extraction. For this reason, the IN718 samples did not reach mass loss equivalent to 100% of binder removal, and values close to 60% have been measured.

Another interesting aspect that might be related with the oxides/nitrides/carbides formation during sintering of the IN718 alloy is a shift of the FeNi peaks, as shown in Figure 117. The three characteristic peaks have all shifted to higher angles after sintering, probably due to distortions in the crystal lattices with the removal of certain amount of iron, chromium and niobium atoms from the alloy, which were previously in solid solution. The peaks shift should have been confirmed with the introduction of a small amount of silicon during the analysis, which would be used as a reference peak, however this procedure was unknown by the author by the time the samples were analyzed.
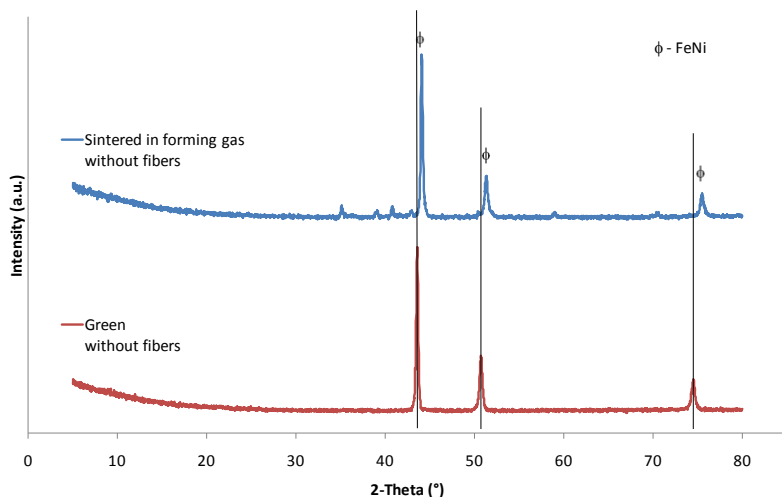
Figure 117 – XRD analysis of IN718 samples before and after sintering. Sintering atmosphere: forming gas. Black lines were added in the graphic to guide the eyes and evidence the peak shift.

4.5.3.3. Porosimetry analysis

The porosity of alumina and IN718 sintered tubes were analyzed by mercury porosimetry and the results are shown in Figure 118 and Figure 119. A considerable amount of mesoporosity has been detected, *i.e.* pores between 2 and 50 nm. But in both alumina and IN718 the biggest amount of porous was in the range of macroporosity, *i.e.* larger than 50 nm.

A higher degree of porosity has been measured in the alumina tube, 40.57 %, with an average pore diameter of 0.62 μm. For the IN718 sintered tube a total porosity of 36.27 % was measured, with an average pore diameter of 1.98 μm. The measured average pore diameter and level of porosity for both alumina and IN718 sintered tubes is adequate for some filtering applications, such as hot-gas filtration, for which a pore size ranging from 0.1 to 50 μm and porosity about 40% are required (FERNANDO, et al., 2005). However, sintering should be improved to allow neck growth between particles and neck formation

between particles and fibers, in order to reach sufficient mechanical strength.
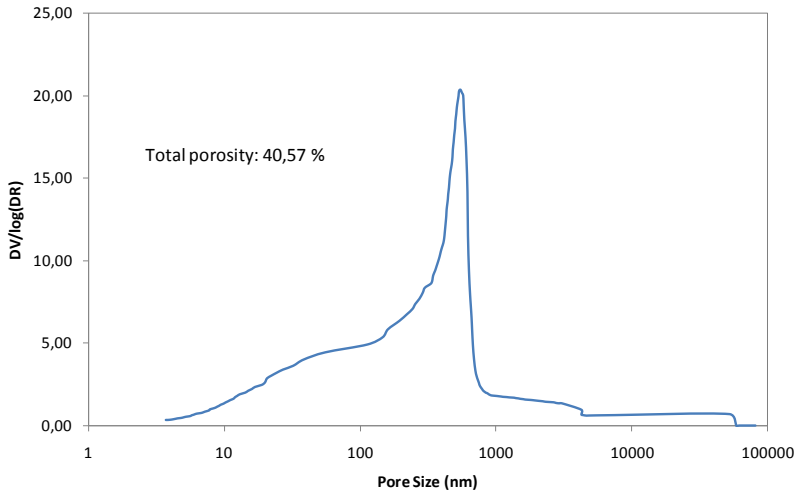
Figure 118 – Pore size distribution measured by mercury porosimetry of alumina sintered tubes.
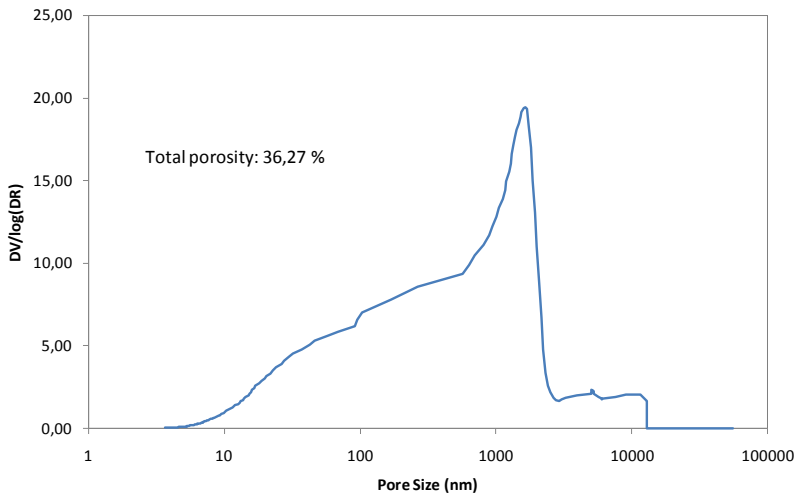
Figure 119 – Pore size distribution measured by mercury porosimetry of IN718 sintered tubes

5. CONCLUSIONS

Regarding the preliminary tests:

i.   The production of disc-shaped samples via feedstock warm-pressing technique showed to be an easy, fast and versatile route for feedstocks development;

ii.   A binder system composed uniquely of LDPE showed to be inadequate for non-oxide powder processing, for which a reducing or inert atmosphere must be used during thermal debinding;

iii.   The use of a LDPE with higher MFI, *i.e.* higher viscosity, does not solve the problems of blisters formation, edge rounding and deformation, originated during thermal debinding in non-oxidizing atmospheres of warm-pressed samples with a binder system consisted of plain LDPE;

Regarding feedstock development:

iv.   Deformation and edge rounding could be eliminated by increasing the solids content in the feedstocks;

v.   The viscosity model of Frankel and Acrivos showed to be the best model to describe the viscosity as a function of solids content for the alumina powder used in the present work;

vi.   The elimination of blisters could only be achieved by introducing at least 30 vol.% of PW in the binder system;

vii.   The introduction of fibers into the feedstock increased considerably the torque during mixing of IN718 feedstock, but not for alumina feedstock. This difference might be related with powder composition, particle shape and particle size distribution;

viii.   Fiber breakage occurred during kneading and was evident on torque decrease of mixing curves. After extrusion, SEM images showed that fiber length has decreased from 30 mm to about 0.5 mm;

ix.   The fibers did not alter the debinding behavior of the warm-pressed samples;

Regarding powder thermoplastic extrusion:

    x.   Higher extrusion pressures, which leads to higher feedstock compaction, are achieved with low cylinder temperature, low die temperature and high piston speed;

    xi.   Cylinder temperature should be kept slightly above the backbone melting point. For the feedstock of the present work, the temperature of 120 °C is adequate. Above this temperature rough surface and banana shape defects happen, whereas below this temperature fish scale and stains appear in the extruded tube.

    xii.   Die temperature should be kept below the backbone melting point, otherwise the extruded tubes show rough surface and banana shape. In the present work 78 °C has shown to be an adequate temperature;

    xiii.   Extrusion speed should be kept as low as possible in order to avoid defects such as fish scale and banana shape. For the present work extrusion speeds equal or lower than 15.7 mm/min showed to be adequate, no matter the die geometry used;

    xiv.   Piston speed should be controlled in order to guarantee the same extrusion speed for different die geometries;

    xv.   Fiber alignment was successfully achieved with the use of powder thermoplastic extrusion for the production of short fibers reinforced composites;

Regarding tubes debinding:

    xvi.   Thermal debinding of tubes showed to be more critical than thermal debinding of warm-pressed discs, and tubes were more prone to undergo deformation;

    xvii.   Deformation during thermal debinding could be diminished for IN718 tubes and completely avoided for alumina tubes with the use of a solvent debinding step, before thermal debinding;

    xviii.   LDPE showed not to be the ideal binder for alumina and IN718 powders, since the onset of sintering temperature is considerably higher than the temperature of LDPE thermal removal (around 450 °C).

xix. Ethanol showed to be a good solvent for solvent debinding, being able to extract more than 90% of SA and PW from the compacts;

Regarding tubes sintering and tubes characterization:

xx. Sintering at 1300 °C for 60 min is enough for neck formation but not enough for neck growth of the used alumina and IN718 powders. Sintering temperature or time should be increased to develop mechanical strength of the tubes;

xxi. XRD analysis of alumina tubes has shown that no unexpected phase or crystallinity change has occurred after sintering of alumina powder together with alumina fibers;

xxii. XRD analysis of IN718 tubes has shown that the expected, but undesired, spinel phase was not formed on IN718 particles and alumina fiber interfaces. On the other hand, undesired carbides, nitrides and oxides have been formed, reducing the amount of this elements in the alloy and, consequently, causing a peak shift on the alloy XRD pattern. The formation of these compounds has showed that the thermal debinding and sintering conditions were not appropriate;

xxiii. Porosimetry analysis have shown that, despite the sintering conditions, temperature and time were not adequate, the level of porosity and pore size distribution was adequate for some filtering applications, such as hot-gas filtration. The increase in sintering level of would, however, decrease the porosity of the material, which could make the tubes inadequate for such applications.

As a final conclusion it can be stated that the powder thermoplastic extrusion has proved to be a promising processing route to produce short fibers reinforced porous MMCs and CMCs.

SUGGESTIONS FOR FUTURE WORK

   i.   Study of mixing, extrusion and sintering behavior of different powders (*e.g.* nickel superalloy IN625) and other oxide fibers;

   ii.   Investigation of the extrusion process with other binders systems, using for example polymers with higher viscosity, more adequate for the extrusion process; or polymers with higher evaporation/degradation temperature, allowing the onset of sintering to occur before the total removal of the backbone;

   iii.   Extrusion of other profile geometries, *e.g.* rods and prisms;

   iv.   Metrological analyses of the tubes after extrusion and after sintering;

   v.   Study of the influence of sintering conditions and parameters on the microstructure evolution, especially regarding the neck growth and porosity;

   vi.   Test of mechanical strength of sintered tubes and comparison between tubes with and without fibers, *e.g.* three point flexural strength;

   vii.   Study the fatigue resistance of the porous tubes and the influence of the fibers on this property;

   viii.   Investigation of filtration efficiency of the porous tubes;

   ix.   Investigation of creep, wear and corrosion resistance of the porous tubes and study the influence of the fibers on these properties;

   x.   Study other sintering techniques, such as hot isostatic pressing, which allows reach a full dense sintered compacts, for the use in other applications in which pores are undesirable.

REFERENCES

AKHTAR, Farid. 2009. Synthesis, microstructure and mechanical properties of Al2O3 reinforced Ni3Al matrix composite. *Materials Science and Engineering: A.* 15 de January de 2009, Vol. 499, 1-2, pp. 415-420.

ASM International. 2000. *ASM Specialty Handbook: Nickel, Cobalt, and Their Alloys.* [ed.] J. R. Davis. s.l. : ASM International, 2000. pp. 204-229. ISBN: 0-87170-685-7.

BANSAL, Narottam P. 2005. *Handbook of ceramic composites.* New York : Kluwer Academic Publishers, 2005. ISBN 1-4020-8133-2.

BOSE, A., et al. 1997. Powder injection molding of inconel 718 alloy. *Advances in Powder Metallurgy and Particulate Materials.* 1997, Vol. 3, pp. 18.99-18.112.

CALLISTER, Willian D. Jr. 2006. *Fundamentos da ciência e engenharia de materiais: uma abordagem integrada.* [trad.] Sérgio Murilo Stamile Soares. Segunda Edição. Rio de Janeiro : LTC, 2006. ISBN 85-216-1515-9.

CALOW, C. A. and MOORE, A. 1972. No hope for ceramic whiskers or fibres as reinforcement of metal matrices at high temperature. *Journal of Materials Science.* 1972, Vol. 7, 5, pp. 543-558.

—. 1971. Reinforcement of metals with ceramic whiskers and fibres. *Composites.* December 1971, Vol. 2, 4, pp. 231-236.

CHAWLA, K. K. 2003. *Ceramic matrix composites.* Second Edition. Dordrecht : Kluwer Academic Publishers, 2003. ISBN 1-40207262-7.

CHAWLA, N. and CHAWLA, K. K. 2006. *Metal matrix composites.* New York : Springer Science+Business Media, Inc., 2006. ISBN 10 0-387-23306-7.

CHENG, Baojia, et al. 2001. Evaluation of rheological parameters of polymer melts in torque rheometers. *Polymer Testing.* 2001, Vol. 20, 7, pp. 811-818.

CHEREMISINOFF, Nicholas P. 1987. *Polymer mixing and extrusion technology.* New York : Marcel Dekker, Inc., 1987. ISBN 0-8247-7793-X.

CHONG, J. S., CHRISTIANSEN, E. B. and BAER, A. D. 1971. Rheology of concentrated suspensions. *Journal of Applied Polymer Science.* 1971, Vol. 15, pp. 2007-2021.

CHOU, T. W., KELLY, A. and OKURA, A. 1985. Fibre-reinforced metal-matrix composites. *Composites.* July 1985, Vol. 16, 3, pp. 187-206.

CHUNG, Chan I. 2000. *Extrusion of polymers: theory and practice.* Cincinnati : Hanser Gardner Publications, Inc., 2000. ISBN 3-446-21376-7.

CINIBULK, Michael K., KELLER, Kristin A. and MAH, Tai-Il. 2004. Effect of ytrium aluminum garnet additions on alumina-fiber-reinforced porous-alumina-matrix composites. *Journal of the American Ceramic Society.* May 2004, Vol. 87, 5, pp. 881-887.

COOPER, Rene M. 1993. Results on powder injection molding of Ni3Al and Application to other intermetallic compositions. *Material Research Society Symposium Proceeding.* 1993, Vol. 288, pp. 903-908.

COOVATTANACHAI, Ornmanee, et al. 2010. Effect of heating rate on sintered series 300 stainless steel. *Songklanakarin Journal of Science and Technology.* 2010, Vol. 32, 2, pp. 163-167.

DEALY, John M. and SAUCIER, Peter C. 2000. *Rheology in plastics quality control.* Munich : Carl Hanser Verlag, 2000. ISBN 3-446-21069-5.

DEALY, John M. and WISSBRUN, Kurt F. 1999. *Melt rheology and its role in plastic processing: theory and applications.* Dordrecht : Kluwer Academic Publishers, 1999. ISBN 0-7923-5886-4.

DHINGRA, A. K. 1980. Alumina fiber FP. *Philosophical Transactions of the Royal Society of London Series A - Mathematical Physical and Engineering Sciences.* 1980, Vol. 294, 1411, pp. 411-417.

DUO, Wenli, et al. 1999. The role of the filter cake in hot gas cleaning with ceramic filters. *Industrial & Engineering Chemistry Research.* January 1999, Vol. 38, 260-269, pp. 260-269.

EILERS, H. 1941. Die Viskosität von Emulsionen hochviskoser Stoffe als Funktion der Konzentration. *Kolloids-Zeitschrift.* 1941, Vol. 97, 4, pp. 313-321.

—. 1949. The colloidal structure of asphalt. *Journal of Physical and Colloid Chemistry.* 1949, Vol. 53, 8, pp. 1195-1211.

FERNANDO, J. A. and CHUNG, D. L. L. 2002. Pore structure and permeability of an alumina fiber filter membrane for hot gas filtration. *Journal of porous materials 9.* 2002, pp. 211-219.

FERNANDO, J.A. and CHUNG, D.L.L. 2005. Thermomechanical properties of alumina fiber membrane. *Ceramics International.* 2005, 31, pp. 453–460.

FRANKEL, N. A. and ACRIVOS, Andreas. 1967. On the viscosity of a concentrated suspension of solid spheres. *Chemical Engineering Science.* 1967, Vol. 22, pp. 847-853.

GERMAN, R. M. and BOSE, A. 1989. Fabrication of intermetallic matrix composites. *Materials Science and Engineering: A.* January 1989, Vol. 107, pp. 107-116.

GERMAN, Randall M. 1990. *Powder injection molding.* Princeton : MPFI Metal Powder Industries Federation, 1990. ISBN 0-918404-95-9.

—. 2005. *Powder Metallurgy and Particulate Materials Processing.* Princeton : MPIF Metal Powder Industries Federation, 2005. ISBN: 0-9762057-1-8.

HACKEMANN, S., FLUCHT, F. and BRAUE, W. 2010. Creep investigations of alumina-based all-oxide ceramic matrix composites. *Composites Part A: Applied Science and Manufacturing.* 2010. In Press, Corrected Proof.

HAJMRLE, K. and ANGERS, R. 1980. Sintering of Inconel 718. *The International Journal of Powder Metallurgy & Powder Technology.* 1980, Vol. 16, 3, pp. 255-266.

HU, W., KARDUCK, P. and GOTTSTEIN, G. 1997. Diffusion of Ni into Al2O3-fibres during hot pressing of Al2O3/Ni3Al long fibre composites. *Acta Materialia.* November 1997, Vol. 45, 11, pp. 991-997.

HU, W., WUNDERLICH, W. and GOTTSTEIN, G. 1996. Interfacial chemical stability during diffusion bonding of Al2O3-fibres with Ni3Al- and NiAl-matrices. *Acta Materialia.* 6, June 1996, Vol. 44, pp. 2383-2396.

INNOCENTINI, M. D. M., et al. 2009. Permeability optimization and performance evaluation of hot aerosol filters made using foam incorporated alumina suspension. *Journal of Hazardous Materials.* February 15, 2009, Vol. 162, 1, pp. 212-221.

IPMD Inovar Communications Ltd. 2010. Powder Metallurgy - A Dynamic and Evolving Industry. *International Powder Metallurgy Directory.* [Online] Orangeleaf Systems Ltd, 2010. [Cited: September 3, 2010.] http://www.ipmd.net/pmindustry/whatispm.

ISHIZAKI, K., KOMARNENI, S. and NANKO, M. 1998. *Porous materials: process technology and applications.* Dordrecht : Kluwer Academic Publishers, 1998. ISBN 0-412-71110-9.

JOHNSON, J. L., et al. 2004. Mechanical properties and corrosion resistance of MIM Ni-based supperalloys. *Advances in Powder Metallurgy and Particulate Materials.* July 2004, Part 4, pp. 89-101.

KRIEGER, Irvin M. and DOUGHERTY, Thomas J. 1959. A mechanism for non-Newtonian flow in suspensions of rigid spheres. *Transactions of The Society of Rheology.* 1959, Vol. III, pp. 137-152.

LEE, P. Y., UCHIJIMA, T. and YANO, T. 2003. Processing and performance of alumina fiber reinforced alumina composites. *Journal of Materials Science and Technology.* 2003, Vol. 19, 4, pp. 337-340.

LEV, L. C. and ARGON, A. S. 1995. Oxide-fiber-oxide-matrix composites. *Materials Science and Engineering A.* June 1, 1995, Vol. 195, pp. 251-261.

LIN, Chung-Kwei, HONG, Shi-Shen and LEE, Pee-Yew. 2000. Formation of NiAl–Al2O3 intermetallic-matrix composite powders by mechanical alloying technique. *Intermetallics.* September 2000, Vol. 8, 9-11, pp. 1043-1048.

MAITY, A. K. and XAVIER, S. F. 1999. Rheological properties of ethylene–propylene block copolymer and EPDM rubber blends using a torque rheometer. *European Polymer Journal.* January 1999, Vol. 35, 1, pp. 173-181.

MARSHALL, D. B. and DAVIS, J. B. 2001. Ceramics for future power generation technology: fiber reinforced oxide composites. *Current Opinion in Solid State and Materials Science.* 2001, Vol. 5, 4, pp. 283-289.

MICHALSKI, A., et al. 2006. NiAl–Al2O3 composites produced by pulse plasma sintering with the participation of the SHS reaction. *Intermetallics.* June de 2006, Vol. 14, 6, pp. 603-606.

MILEIKO, S. T. 1997. *Metal and ceramic based composites.* [ed.] R. Byron Pipes. Amsterdam : Elsevier Science B.V., 1997. Vol. 12, Composite Materials Series. ISBN 0-444-82814-1.

—. 2002. Oxide-fibre/Ni-based matrix composites - III: a creep model and analysis of experimental data. *Composites Science and Technology.* February 2002, Vol. 62, 2, pp. 195-204.

MILEIKO, S. T., et al. 2004. Oxide fibres in a nickel-base matrix - do they degrade or become stronger? *Proceedings of the Institution of Mechanical Engineers Part L - Journal of Materials - Design and Applications.* August de 2004, Vol. 218, L3, pp. 193-199.

MILEIKO, S. T., et al. 2002b. Oxide-fibre/Ni-based matrix composites - II: mechanical behaviour. *Composites Science and Technology.* February 2002b, Vol. 62, 2, pp. 181-193.

MILEIKO, S. T., et al. 2002a. Oxide-fibre/nickel-based matrix composites - part I: fabrication and microstructure. *Composites Science and Technology.* February de 2002a, Vol. 62, 2, pp. 167-179.

MOONEY, M. 1951. The viscosity of a concetrated suspension of spherical particles. *Journal of Colloid Science.* 1951, Vol. 6, 2, pp. 162-170.

MURUT, Aldo E. and WHITE, Calvin L. 1997. Reinforcement/matrix interaction in Al2O3 and Al2O3-ZrO2 fiber-reinforced Ni3Al matrix composites. *Acta Materialia.* June 1997, Vol. 46, 6, pp. 2547-2563.

PADMAVARDHANI, D., GOMEZ, A. and ABBASCHIAN, R. 1998. Synthesis and microstructural characterization of NiAl-Al2O3 functionally gradient composites. *Intermetallics.* 1998, Vol. 6, 4, pp. 229-241.

Plastics Today. 2010. Sintering: A critical step. *Home of modern plastic and injection molding.* [Online] Canon Communications LLC, 2010. [Cited: October 11, 2010.] http://www.plasticstoday.com/articles/sintering-critical-step.

POVIRK, G. L., et al. 1988. Interfaces in nickel aluminide/alumina fibre composites. *Journal of Materials Science.* 1988, Vol. 23, pp. 3945-3950.

PRABHAKARAN, K., et al. 2005. A Novel Process for Low-Density Alumina Foams. *Journal of the American Ceramic Society.* September de 2005, Vol. 88, 9, pp. 2600-2603.

PRENTICE, P. 1995. *Rheology and its role in plastics processing.* [ed.] Rebecca Dolbey. Shawbury : Rapra Technology Ltd., 1995. Vol. 7, Number 12, Report 84. ISSN: 0889-3144.

QUEMADA, D. 1977. Rheology of concentrated disperse systems and minimum energy dissipation principles. 1. Viscosity-concentration relationship. *Rheologica Acta.* 1977, Vol. 16, 1, pp. 82-94.

—. **1978.** Rheology of concentrated disperse systems. 3. General features of proposed non-Newtonian model - Comparison with experimental Data. *Rheologica Acta.* 1978, Vol. 17, pp. 643-653.

RAUWENDAAL, Chris. 1986. *Polymer extrusion.* Munich; Vienna; New York : Hansers Publishers, 1986. ISBN 3-446-14196-0.

REED, James S. 1995. *Principles of Ceramics Processing.* Second Edition. New York : A Wiley-Interschience Publication, 1995. ISBN 0-471-59721-X.

ROUQUEROL, J., et al. 1994. Recommendations for the characterization of porous solids (Technical Report). *Pure and Applied Chemistry.* 1994, Vol. 66, 8, pp. 1739-1758.

SHENOY, Aroon V. 1999. *Rheology of filled polymer systems.* Dordrecht : Kluwer Academic Publishers, 1999. ISBN 0-412-83100-7.

Special Metals Corporation. 2008. Special Metals. *Special Metals.* [Online] Precision Castparts Corp. company, 2008. [Cited: Oktober 19, 2010.] http://www.specialmetals.com/.

STOLOFF, N. S. and ALMAN, D. E. 1991. Powder processing of intermetallic alloys and intermetallic matrix composites. *Materials Science and Engineering: A.* October 1991, Vol. 144, 1-2, pp. 51-62.

STUDART, André R., et al. 2006. Processing Routes to Macroporous Ceramics: A Review. *Journal of the American Ceramic Society.* June 2006, Vol. 89, 6, pp. 1771–1789.

SURESH, S., MORTENSEN, A. and NEEDLEMAN, A. 1993. *Fundamentals of metal matrix composites.* Stoneham : Butterworth-Heinemann, 1993. ISBN 0-7506-9321-5.

TROPEA, Cameron, YARIN, Alexander and FOSS, John F. 2007. *Springer handbook of experimental fluid mechanics.* Berlin, Heidelberg : Springer-Verlag, 2007. ISBN 978-3-540-25141-5.

VALENCIA, J. J., et al. 1994. Microstructure and mechanical properties of INCONEL 625 and 718 alloys processed by powder

injection molding. [ed.] E. A. Loria. *Superalloys 718, 625, 706 and Various Derivatives.* 1994.

VALENCIA, J. J., SPIRKO, J. and SCHMEES, R. 1997. Sintering effect on the microstructure and mechanical properties of alloy 718 processed by powder injection molding. [ed.] E. A. Loria. *Superalloys 718, 623, 706 and Various Derivatives.* 1997.

WEGMANN, M. R., MISIOLEK, W. Z. and GERMAN, R. M. 1991. Injection Molding and Reactive Sintering of Ni3Al. *Advances in Powder Metallurgy.* 1991, Vol. 2, pp. 75-180.

WOOD, S. and HARRIS, A. T. 2008. Porous burners for lean-burn applications. *Progress in Energy and Combustion Science.* October 2008, Vol. 34, 5, pp. 667-684.

YE, Hezhou, LIU, Xing Yang and HONG, Hanping. 2008. Fabrication of metal matrix composites by metal injection molding - A review. *Journal of Materials Processing Technology.* 2008, Vol. 200, 1-3, pp. 12-24.

ZHU, H. X. and ABBASCHIAN, R. 2000. In-situ processing of NiAl–alumina composites by thermite reaction. *Materials Science and Engineering A.* April 30, 2000, Vol. 282, 1-2, pp. 1-7.

ANEXO A – Resumo estendido em português

Introdução e objetivos

Materiais com poros interconectados são utilizados em diversas aplicações, em particular na filtragem. Exemplos de processos de filtragem são: purificação de água, filtração de óleo, filtração de aerossóis, filtração de gases quentes.

Nestes processos, os materiais porosos devem apresentar as seguintes propriedades:

     i.   Rede interconectada de poros;
    ii.   Distribuição de tamanho de poros adequada;
   iii.   Resistência mecânica;
   iv.   Resistência térmica;
    v.   Resistência a corrosão e a oxidação.

Contudo, se por um lado estes materiais devem apresentar uma alta porosidade, por outro lado eles devem ter resistência mecânica suficiente para suportar os esforços impostos a estes componentes.

A introdução de fibras curtas é uma maneira inteligente de aumentar a resistência mecânica destes componentes sem prejudicar a indispensável permeabilidade.

O principal objetivo deste trabalho é a obtenção de compósitos tubulares porosos de matrizes metálica e cerâmica, reforçados por fibras curtas, através da extrusão termoplástica de pós.

A extrusão termoplástica de pós é um processo capaz de produzir tubos de paredes finas, com alta razão de aspecto, isto é, tubos longos com diâmetro e espessura de parede muito inferiores ao comprimento. Além disso, a extrusão é um processo contínuo, com capacidade produtiva relativamente alta. No caso da extrusão termoplástica, uma das vantagens é a manutenção do tamanho de fibras, pois este processo impõe esforços cisalhantes muito inferiores se comparados com a extrusão convencional. Outra característica do processo em questão é o alinhamento das fibras na direção da extrusão.

Além do objetivo principal, são também objetivos deste trabalho:

     i.   Desenvolver um *feedstock* adequado aos processos de remoção de ligantes e extrusão;

  ii. Investigar a influência das fibras durante os processos de mistura e remoção dos ligantes;

  iii. Investigar a influência dos parâmetros de extrusão, notadamente, temperatura do cilindro, temperatura da matriz de extrusão e velocidade do pistão;

  iv. Caracterizar os tubos sinterizados em termos de microestrutura, porosidade e fases cristalinas.

Breve descrição experimental

Para compor a matriz dos compósitos de matriz metálica foi escolhido pó de superliga de níquel IN718, com tamanho médio de partícula de 6,5 μm em formato esférico. No caso dos compósitos de matriz cerâmica foi escolhido pó de α-alumina, com tamanho médio de partícula de 2,5 μm em formato poligonal.

Como reforço foram selecionadas fibras comerciais de alumina Nextel™ 610, fornecidas pela 3M Company. As fibras foram fornecidas picadas no comprimento de 30 mm, com diâmetro entre 10 e 12 μm.

Como ligantes foram utilizados dois polietilenos de baixa densidade, um com índice de fluidez de 2,0 g/10min (LDPE02) e outro com índice de fluidez de 70,0 g/10min (LDPE70), parafina (PW) e ácido esteárico (SA).

O desenvolvimento do *feedstock* foi dividido em duas etapas.

A primeira consistiu em definir o teor de sólidos. Para isto foi utilizado somente polietileno (LDPE02 e LDPE70) e alumina, por ser o pó que rendia *feedstocks* de maior viscosidade. O teor de sólidos variou entre 54 e 62 % em volume.

A segunda etapa consistiu em definir o teor de parafina no sistema ligante. Para isso foram utilizados como ligantes LDPE, PW e SA e, desta vez, *feedstocks* dos dois tipos de pós (alumina e IN718) foram produzidos. O teor de LDPE, bem como o de PW, variou entre 0 e 95 % em volume. O teor de SA foi fixado em 5 % em volume. Nesta etapa foi utilizado o teor de sólidos definido na etapa anterior.

O procedimento utilizado em ambas as etapas do desenvolvimento do *feedstock* consistiu em misturar os pós com os ligantes em um *kneader* (reômetro de torque) a 180 °C por 30 minutos e, em seguida a 152 °C por 40 minutos. Nesta etapa, o valor do torque necessário para a mistura foi importante na avaliação do teor de sólidos, bem como do teor de PW. Em seguida o *feedstock* produzido foi granulado em um reômetro capilar através de uma matriz de 1 mm de

diâmetro a 140 °C. Após isso, os grânulos foram prensados a morno (a temperaturas em torno da temperatura de fusão dos polietilenos) em forma de disco, através de uma prensa manual, sob força de 10 kN. A matriz utilizada apresentava 28 mm de diâmetro. A quantidade de grânulos prensada foi suficiente para produzir discos com espessura de 0.8 mm. Os discos prensados foram então levados ao forno para a remoção dos ligantes, que se deu à 600 °C por 60 minutos, com uma taxa de aquecimento de 0,5 °C/min, em atmosferas redutora (no caso dos compósitos de matrizes metálica e cerâmica) e oxidante (somente no caso de compósitos de matriz cerâmica). Em seguida, os discos foram avaliados no tocante à de presença de bolhas e deformação, para definição do teor de sólidos e teor de parafina.

Para a extrusão de tubos, as fibras de alumina foram incorporadas ao *feedstock* no teor de 30 % em volume. Tubos as seguintes geometrias foram extrudados:

     i.   10,0 mm de diâmetro e 1,0 mm de espessura;
    ii.   10,0 mm de diâmetro e 0.6 mm de espessura;
   iii.   4,5 mm de diâmetro e 1,0 mm de espessura.

Os parâmetros de extrusão, isto é, temperatura do cilindro, temperatura da matriz de extrusão e velocidade do pistão, foram controlados a fim de se obter extrudados visualmente sem defeitos.

Os ligantes foram removidos por meio de extração por solvente e extração térmica. A extração por solventes se deu a 60 °C em um banho de etanol 95 % durante 5 horas. A extração térmica se deu a 600 °C durante 60 minutos, com uma taxa de aquecimento de 0,5 °C/min, em atmosferas redutora e oxidante.

Finalmente os tubos foram sinterizados a 1300 °C durante 60 minutos, a uma taxa de aquecimento de 5,0 °C/min, também em atmosferas redutora e oxidante.

Os tubos foram então caracterizados por microscopia eletrônica de varredura, difração de raio-X e porosimetria.

Principais resultados

Durante os testes preliminares os discos de alumina apresentaram defeitos após a extração do LDPE70, realizadas em atmosfera redutora. Os defeitos encontrados foram bolhas, arredondamentos das arestas e deformação. Nenhum defeito foi encontrado nos discos de alumina após

a remoção dos ligantes em atmosfera oxidante. No caso dos discos de IN718, os mesmos defeitos surgiram após a remoção dos ligantes em atmosfera redutora. Não foram realizados testes de extração em atmosfera oxidante para este pó, devido a potencial oxidação da matriz metálica.

Não foram obtidos resultados melhores com LDPE02, e este polietileno não foi posteriormente utilizado, pois a viscosidade dos *feedstocks* com este ligante era muito elevada.

Através da análise do torque durante a mistura dos *feedstocks* de alumina, com diferentes teores de sólidos, foi possível calcular o teor máximo de sólidos admissível para este sistema, no valor de 71,4 % em volume. Com base nos resultados de extração térmica dos mesmos *feedstocks*, o teor de sólidos ficou definido em 62 % em volume.

Os valores de torque medidos durante esta etapa foram comparados a diversos modelos de viscosidade, sendo que o modelo de Frankel e Acrivos foi o que melhor descreveu o comportamento do *feedstock* em questão.

A quantidade de bolhas nas amostras, após a extração dos ligantes, foi o parâmetro utilizado como critério para a definição do teor de parafina. Sendo assim o teor de parafina mínimo necessário para evitar a formação deste defeito foi de 30 % em volume.

Por fim, o *feedstock* final para a extrusão foi definido, sendo constituído da seguinte forma:

     i.   62 % em volume de sólidos, dos quais:
          a.   70 % em volume composto de pós;
          b.   30 % em volume composto de fibras;
    ii.   38 % em volume de ligantes, dos quais:
          a.   5 % em volume de SA;
          b.   30 % em volume de PW;
          c.   65 % em volume de LDPE70.

Durante a extrusão, a pressão interna do cilindro variou com a temperatura do cilindro seguindo a relação da equação de Arrhenius. Tubos extrudados com cilindro acima da temperatura de fusão do LDPE70 apresentaram empenamento e superfície rugosa. Os tubos extrudados abaixo da temperatura de fusão ficaram retos, contudo outros dois defeitos superficiais ficaram evidentes, como escama de peixe e manchamento.

A temperatura da matriz de extrusão foi controlada através do contato com fluido refrigerante. Os fluidos refrigerantes utilizados foram etanol e água. Os melhores resultados foram obtidos através do resfriamento da matriz com etanol e alguns tubos sem defeitos foram obtidos desta forma.

Finalmente, o último parâmetro de extrusão controlado foi a velocidade do pistão. Foi observado que a velocidade do pistão não era o fator mais relevante, e sim, a velocidade de extrusão, à qual está diretamente relacionada a velocidade do pistão. Diversos testes foram feitos a diferentes velocidades e, finalmente, a velocidade de extrusão ótima foi definida como sendo 15,7 mm/min.

Enfim os parâmetros de extrusão foram definidos da seguinte forma:

    i.   Temperatura do cilindro: 120 °C;
    ii.   Temperatura da matriz de extrusão: 120 °C na entrada e 78 °C na saída;
    iii.   Velocidade de extrusão: 15,7 mm/min.

Sob as condições acima descritas, os tubos produzidos não apresentavam qualquer tipo de defeito visual. Diversos tubos com comprimento de aproximadamente 15 cm foram extrudados nas três diferentes geometrias.

Em seguida, foi realizada a extração dos ligantes dos tubos. A tentativa inicial de remover os ligantes através de extração térmica foi ineficaz e os tubos colapsaram, perdendo, em alguns casos, totalmente a forma cilíndrica. Com base neste resultado decidiu-se por utilizar, previamente à extração térmica, a extração por solvente.

A análise das amostras através de microscopia eletrônica, antes e depois da extração por solvente, mostrou que uma rede de poros surgiu nas amostras após a extração por solvente. A obtenção desta rede de poros tem por finalidade facilitar a permeação dos gases produzidos durante a posterior remoção térmica dos ligantes.

Os resultados após a extração por solvente seguida por extração térmica foram satisfatórios e a maioria dos tubos não apresentou deformação.

Finalmente, os tubos foram sinterizados a 1300 °C durante 60 minutos.

As imagens obtidas por microscopia eletrônica de varredura mostraram uma estrutura bastante porosa, na qual as partículas

praticamente não sinterizaram e o crescimento dos pescoços de sinterização não foi observado.

A formação dos pescoços pode ser somente observada entre as partículas de IN718. As fibras, por sua vez, aparentemente não aderiram a nenhuma das partículas, tanto nos compósitos de matriz de IN718 quanto nos de matriz de alumina.

Os resultados de difração de raios-X mostraram que nenhuma fase diferente de α-alumina formou-se nos compósitos de matriz cerâmica. Já nos compósitos de matriz metálica, picos de nitretos, carbonetos e óxidos foram identificados. Com base nestes resultados, pode-se dizer que a atmosfera redutora, rica em nitrogênio, interagiu com as amostras formando nitretos. O carbono, oriundo dos ligantes, que não foi totalmente extraído na forma de gases, também interagiu com as partículas metálicas, formando os carbonetos. A oxidação das amostras, por sua vez, mostrou que a vedação do forno não foi satisfatória, e uma quantidade significativa de oxigênio estava presente na atmosfera durante o tratamento térmico.

Outro aspecto interessante observado na difratometria dos compósitos de matriz metálica foi o deslocamento dos picos característicos da liga de níquel. Este deslocamento se deve, provavelmente, a distorções na rede cristalina causada pelo empobrecimento da liga em relação aos elementos formadores de carbonetos, nitretos e óxidos.

Finalmente, a análise porosimétrica das amostras mostrou que os tubos em matriz cerâmica apresentaram uma porosidade de 40,57 %, com um tamanho médio de poros de 0,62 μm. Os tubos em matriz metálica apresentaram uma porosidade de 36,27, com um tamanho médio de poros de 1,98 μm. A partir desses resultados pode-se dizer que os compósitos tubulares porosos de matriz metálica e cerâmica, reforçados por fibras curtas, obtidos através da extrusão termoplástica de pós, são adequados à aplicação de filtragem de gases quentes, a qual requer uma porosidade em torno de 40 %, com uma distribuição de tamanho de poros entre 0,1 e 50 μm.

Conclusões mais relevantes

Em relação ao desenvolvimento dos *feedstocks*:

i. Deformação e arredondamento de arestas, após remoção dos ligantes dos discos prensados, puderam ser eliminados com o aumento do teor de sólidos;

ii. A eliminação de bolhas pode ser alcançada somente com a introdução de, no mínimo, 30 % em volume de PW;

iii. A quebra das fibras foi satisfatoriamente alcançada durante a preparação da mistura.

Em relação à extrusão termoplástica de pós:

iv. Altas pressões de extrusão, que trazem como consequência uma mais efetiva compactação do *feedstock*, são obtidas através de uma baixa temperatura do cilindro, baixa temperatura da matriz de extrusão e alta velocidade de extrusão;

v. A temperatura do cilindro deve ser mantida ligeiramente acima da temperatura de fusão do *backbone*. Para o *feedstock* deste trabalho, 120 °C é uma temperatura adequada. Acima desta temperatura, superfície rugosa e empenamento dos tubos tornam-se evidentes, ao passo que, abaixo desta temperatura, escamas de peixes e manchas surgem na superfície dos tubos;

vi. A temperatura da matriz de extrusão deve ser mantida abaixo da temperatura de fusão do *backbone*, caso contrário, surgem defeitos como empenamento e rugosidade na superfície dos tubos. Para o presente trabalho, 78 °C foi a temperatura adequada para a matriz de extrusão;

vii. A velocidade de extrusão deve ser mantida a mais baixa possível, para evitar defeitos como escama de peixe e empenamento. Para o *feedstock* desenvolvido, a velocidade máxima que permitia a produção de extrudados livres de defeitos foi de 15,7 mm/min;

viii. A extrusão termoplástica promoveu o alinhamento das fibras.

Em relação à remoção de ligantes dos tubos:

ix.   A deformação dos tubos foi evitada com a utilização de remoção de ligantes por solventes;

x.   Etanol é um bom solvente para extração de PW e SA;

Em relação à sinterização e caracterização dos tubos sinterizados:

xi.   Sinterização a 1300 °C durante 60 minutos não é suficiente para promover o crescimento dos pescoços de sinterização entre as partículas e entre as fibras e partículas;

xii.   A análise difratométrica mostrou que nenhuma fase, além de α-alumina, formou-se durante a sinterização dos compósitos de matriz cerâmica;

xiii.   Nitretos, carbonetos e óxidos foram encontrados nos compósitos de matriz metálica, indicando que a atmosfera utilizada não foi a mais adequada para a sinterização destes compósitos;

xiv.   Porosimetria mostrou que os tubos produzidos apresentam porosidade e distribuição de tamanho de poros adequada para a filtração de gases quentes.

Finalmente, a extrusão termoplástica de pós provou ser um processo promissor para a obtenção de compósitos tubulares porosos em matriz cerâmica e metálica reforçados por fibras curtas.